Deposition of Ultrafine Lines using Pattern Transfer Printing for Metallization of Silicon Solar Cells

zur Erlangung des akademischen Grades eines
DOKTORS DER INGENIEURWISSENSCHAFTEN (Dr.-Ing.)

von der KIT-Fakultät für Chemieingenieurwesen und Verfahrenstechnik des
Karlsruher Instituts für Technologie (KIT)
genehmigte

DISSERTATION

von
Adrian, M.Sc.
aus Bandung, Indonesien

Tag der mündlichen Prüfung: 18.05.2022
Erster Gutachter: Prof. Dr. Norbert Willenbacher
Zweiter Gutachter: Prof. Dr. Stefan W. Glunz

Acknowledgements

I would like to express my deepest gratitude to Prof. Dr. Norbert Willenbacher for providing me with the opportunity to complete my doctoral thesis at the Institute of Mechanical Process Engineering and Mechanics (MVM) – Applied Mechanics Group (AME), for his continuous support and encouragement, and for dispelling my doubts. I am also thankful for our fruitful discussions that resulted in new ideas and for his guidance in helping me become a better researcher.

Sincere appreciation and thanks to Prof. Dr. Stefan Glunz for being the second supervisor of my thesis and for his valuable feedback to help me improve this work even further.

Words cannot express my thanks to Jan Lossen for guiding and supervising me during my time at the International Solar Energy Research Center (ISC) Konstanz, as well as for his dedicated support, providing constructive advice throughout my work and freedom in experimental design.

I would also want to express my gratitude to everyone who supported me during my time as a Ph.D. student at the KIT and the ISC Konstanz. Additionally, I am extremely grateful to:

- Radovan Kopecek, Petra Hoffmann, Rudolf Harney, Kristian Peter and Eckard Wefringhaus for giving me the chance to pursue my Ph.D. at the ISC Konstanz and for their full support.
- The Federal Ministry of Economics and Energy (BMWi) for financial support in the RefinedPV project. Special thanks also to Hanwha Q Cells GmbH for the preparation of the precursors, Heraeus Precious Metals for supplying tailored silver paste, and Utilight Ltd. for providing polymer films and extensive technical discussions on PTP.
- Dominik Rudolph, Christoph Peter, Valentin Mihailetchi and Jan Hoß for technical and scientific discussions on the experiments, laser process, metallization and characterization steps.
- Zih-Wei Peng, Lejo Koduvelikulathu, Haifeng Chu, Elina Schmid, Sabine Deck, Razvan Roescu and Aditya Chaudhary, for your moral support, friendship and advice.
- Kosuke Tsuji from Toyo Aluminium K.K. for recording the SEM images.
- Daniel Tune for proofreading my thesis.
- All my colleagues at the ISC Konstanz, especially Pedro Diaz-Perez, Rafael Marczak, Lejlja Hildebrand, Annette Helfricht, Mertcan Comak, Tanju Eren and Stephan Eisert, for your assistance with cell processing.
- All colleagues at the AME, especially Ceren Yüce and Karim Abdel Aal, for your technical support and discussions about rheology and organizational questions.

Lastly, I would be remiss in not mentioning my family, especially my parents and my brother for their unwavering support, guidance and encouragement over the years, as well as my dearest wife for your love, patience, and endless support during this period. Regardless of the distance, you are always there for me.

Abstract

This thesis deals with the fabrication of silver electrodes for the front metallization of crystalline silicon solar cells. It explores metallization methods to reduce silver consumption while preserving the electrical characteristics necessary for an efficient solar cell. One of the alternatives to standard screen-printing technology is Pattern Transfer Printing (PTP). PTP technology utilizes laser irradiance to transfer silver paste from trenches on the surface of polymer films onto a target substrate (e.g. silicon wafer), producing ultrafine silver finger electrodes with a high aspect ratio. The use of narrower silver finger electrodes could decrease the production cost enormously due to less silver consumption. At the same time, this could also improve the cell efficiency by increasing the short-circuit current density due to less shading at the cell front side. A challenge is to limit the fill factor loss caused by a potentially higher series resistance.

The first part of this thesis focuses on the PTP process in order to gain an understanding of the governing principles of the laser-based printing process and to optimize it towards the fabrication of narrower silver finger electrodes with a high aspect ratio. The printing sequence of PTP is divided into two steps: filling and transfer. For the filling step, two squeegee blades are required to fill silver paste into trenches and at the same time remove the residue of silver paste from the polymer film. In this work, a higher angle for the second squeegee blade toward the film surface is demonstrated to minimize the paste scooping inside the trenches, producing better electrode lines with more homogeneous height. The laser power is the key parameter for the transfer process of PTP technology. A strong dependence of line aspect ratio and amount of debris on the laser power is observed. Higher laser power is found to accelerate the shape deformations towards broader lines with a lower aspect ratio and to increase the amount of debris around silver lines. Therefore, an accurate optimization of laser power before the laser transfer process is essential for fabricating narrower electrodes with a high aspect ratio and low debris. Three possible scenarios related to the laser power during the laser transfer process of PTP are described: no transfer, optimum transfer and explosive transfer.

Two key aspects that control the PTP laser transfer process from a material point of view are investigated, namely the physico-chemical properties of silver pastes and film materials. An increase in paste yield stress minimizes the line spreading during the contactless laser transfer process, resulting in narrower line width and higher aspect ratio. The line spreading of PTP is caused by a decrease in yield stress after the laser transfer process as a result of local paste heating and by the pressure created from the vaporization of volatile paste components. A low laser power threshold can be achieved using silver pastes with a lower boiling temperature of volatile components and poor wetting between silver paste and polymer film. The thinnest film material has the lowest light transmission. However, this film material requires the lowest laser power threshold due to a weaker adhesion of silver paste to film material and a better alignment with the laser focal plane.

The second section of this thesis evaluates PTP technology for the front metallization of solar cells compared with state-of-the-art screen-printing technology. The print quality of PTP technology utilizing four different trench geometries on the polymer surface is analyzed, including line shapes, silver consumption and amount of debris. Furthermore, the electrical properties of PTP-metallized solar cells are compared to the screen-printing references. Each trench geometry requires a specific laser power, which is proportional to the ratio between the circumference and the horizontal interface of the trenches. Finger electrodes printed with PTP technology are narrower than the fingers fabricated with the screen-printing references, varying between 18 μm and 22 μm depending on the trench geometry used. These smaller silver finger lines result in a significant improvement in J_{sc} and a smaller gain in V_{oc} for all PTP groups than the screen-printing references. However, narrower electrode lines of PTP contribute also to a moderate FF loss due to higher series resistance. Since this loss in FF is smaller than the gains in J_{sc} and V_{oc}, an efficiency gain using PTP technology is possible.

It is demonstrated in this thesis that, using PTP technology, the average silver consumption is reduced by 54% and at the same time the cell efficiency is improved by $0.12\%_{abs}$ for the champion cell of PTP-printed cells (average electrode width of 22 μm and cross-sectional area as small as 220 μm^2) compared with the screen-printing references. The smallest finger obtained by PTP technology has an electrode width of 18 μm with an aspect ratio of 0.51, enabling silver reduction by 74%. However, a further paste modification and front grid optimization would be needed to reduce the significant FF loss that still presents for the PTP group with 18 μm finger.

An investigation of emitter sheet resistance for crystalline silicon solar cells highlights the importance of narrower silver lines for the high sheet emitter resistance to minimize the current transport losses without additional shading caused by higher finger count. However, silver paste adjustment is mandatory for both technologies, ensuring a good contact formation to avoid additional losses with reduced finger width. Due to the fact that the number of busbars is increasing in modern PV technology, the reduction of FF by the narrower PTP fingers will be reduced more and more.

This thesis provides guidelines for paste and film material design aiming at narrower silver electrode lines using PTP technology. The assessment of PTP technology for photovoltaic application in this thesis shows that the ultrafine silver electrode fingers deposited by PTP are suitable for the front metallization of silicon solar cells, which reduces silver consumption substantially while simultaneously increasing cell efficiency in comparison to industrial state-of-the-art screen-printing technology.

Zusammenfassung

In dieser Arbeit werden Kontaktstrukturen aus Silberpaste als vorderseitige Elektrode von kristallinen Silizium-Solarzellen hergestellt und untersucht. Ziel ist dabei eine deutliche Reduzierung des Silberverbrauchs unter Erhaltung guter elektrischer Eigenschaften der Solarzelle. Eine vielversprechende Alternative zum Standard-Siebdruckverfahren ist die Pattern Transfer Printing (PTP) Technologie. Die PTP-Technologie verwendet eine Polymer-Folie mit eingeprägten Gräben und Laserbestrahlung, um ultrafeine Linien aus Silberpaste auf eine Substratoberfläche zu deponieren. Schmaler gedruckte Linien können die Produktionskosten aufgrund eines reduzierten Silberverbrauches deutlich senken. Gleichzeitig können sie den Zellwirkungsgrad erhöhen, indem sie durch eine verringerte Abschattung der Zellvorderseite eine höhere Kurzschlussstromdichte ermöglichen. Eine Herausforderung besteht darin, einen durch höheren Serienwiderstand verursachten Füllfaktorverlust zu vermeiden.

Im ersten Teil dieser Arbeit wird der PTP-Druckprozess untersucht, mit dem Ziel ein Verständnis für die steuernden Prinzipien des Laserdruckverfahrens zu erlangen und den Prozess im Hinblick auf die Herstellung von schmalen Silberelektroden mit einem hohen Aspektverhältnis zu optimieren. Der Druckvorgang beim PTP-Verfahren lässt sich in zwei Prozesse unterteilen: die Füllung der Gräben und die anschließende Übertragung der Silberpaste auf das Substrat. Es sind zwei Rakeln erforderlich, um die Silberpaste in die Gräben zu füllen und Reste der Silberpaste von der Oberfläche der Folie zu entfernen. Ein größerer Winkel zwischen dem zweiten Rakel und der Folienoberfläche vermeidet, dass die Paste in Teilen wieder aus den Gräben entfernt wird und führt somit zu Elektroden mit einer gleichmäßigeren Höhe.

Die Laserleistung ist der bestimmende Parameter zur Regulierung des PTP-Übertragungsprozesses. Es wird eine starke Abhängigkeit des Aspektverhältnisses von Elektroden und der Menge ungewünschter Silber-Ablagerungen außerhalb der Linie von der Laserleistung festgestellt. Höhere Laserleistungen verändern die Linienform hin zu breiten Linien mit einem geringeren Aspektverhältnis und führen zu vermehrten Ablagerungen von Pastenspritzern um die Silberlinien herum. Daher ist eine genaue Optimierung der Laserleistung erforderlich, sodass schmale Elektroden mit hohem Aspektverhältnis und geringen Silber-Ablagerungen hergestellt werden. Es werden drei mögliche Szenarien hinsichtlich der Laserleistung betrachtet: keine Übertragung, optimale Übertragung und explosive Übertragung bei zu hoher Leistung.

Des Weiteren werden Materialeigenschaften untersucht, die für den PTP Lasertransferprozess eine große Rolle spielen, nämlich die physikalisch-chemischen Eigenschaften der Silberpasten und der Folienmaterialien. Eine Erhöhung der Fließgrenze der Silberpaste minimiert die Linienverbreitung während des Übertragungsprozesses, was zu einer geringeren Linienbreite und einem höheren Aspektverhältnis führt. Die Verbreitung der Linien wird verursacht durch eine Verringerung der Fließgrenze aufgrund einer lokalen Erwärmung der Silberpaste und durch den Druck, der beim Verdampfen flüchtiger Pastenbestandteile entsteht. Eine geringere Laserleistung kann

bei Silberpasten verwendet werden, die Lösungsmittel mit einer niedrigeren Siedetemperatur enthalten, und bei Pasten, welche die Polymerfolie schlecht benetzen. Für ein anderes, dünneres Folienmaterial wurde eine geringere Lichtdurchlässigkeit festgestellt. Trotzdem erfordert dieses Folienmaterial eine niedrigere Laserleistung, was auf eine geringere Benetzung des Folienmaterials durch die Silberpaste und eine bessere Ausrichtung hinsichtlich der Fokusebene der Laser zurückzuführen ist.

Der zweite Teil dieser Arbeit befasst sich mit der Evaluierung der PTP-Technologie für die Metallisierung der Vorderseiten von Solarzellen im Vergleich zur etablierten Siebdrucktechnologie als Referenz. Die Auswirkung von verschiedenen Grabengeometrien auf Linienform, Silberverbrauch und Menge der Ablagerung wird analysiert. Dafür werden auch die elektrischen Parameter entsprechender Solarzellen mit Referenzen verglichen, die mit Siebdruck hergestellt werden. Jede Grabengeometrie erfordert eine unterschiedliche Laserleistung. Es wird gezeigt, dass die erforderliche Laserleistung mit dem Verhältnis aus dem Umfang und der horizontalen Breite des Grabens korreliert. Mit der PTP-Technologie können schmalere Fingerlinien hergestellt werden, als mit dem Siebdruck als Referenz-Technologie. Die erzielten Fingerbreiten variieren zwischen 18 und 22 µm, abhängig von der verwendeten Grabengeometrie. Dies führt bei allen PTP-Gruppen zu einem deutlichen Gewinn des Kurzschlussstromes J_{sc} und zu einer geringen Steigerung der offenen Klemmenspannung V_{oc}. Allerdings führen die schmaleren Silberfinger des PTP-Druckers wegen eines höheren Serienwiderstands zu einem moderaten Füllfaktor (*FF)*-Verlust.

In dieser Arbeit wird gezeigt, dass mit der PTP-Technologie eine Reduzierung der Silbermenge von 54 % im Vergleich zur mit Siebdruck hergestellten Referenz erreicht werden kann (bei einer durchschnittlichen Elektrodenbreite von 22 µm und einer durchschnittlichen Querschnittsfläche von nur 220 µm^2). Zudem konnte für die besten mittels PTP gedruckten Zellen der Energiewandlungswirkungsgrad um 0,12 $\%_{abs}$ gegenüber der Referenz verbessert werden. Die schmalsten mit der PTP-Technologie hergestellten Finger haben eine Linienbreite von 18 µm bei einem Aspektverhältnis von 0,51, was sogar eine Reduzierung des Silbereinsatzes um 74 % ermöglicht. Allerdings sind bei dieser PTP-Gruppe eine weitere Pastenmodifikation und eine Optimierung des Layouts zur Verbesserung des Serienwiderstands erforderlich, um den erheblichen *FF*-Verlust zu verringern.

Eine Untersuchung des Schichtwiderstands des Emitters für kristalline Silizium-Solarzellen zeigt, dass schmalere Silberlinien helfen können, Widerstandverluste durch verringerte Querleitung im Emitter ohne zusätzlicher Abschattung aufgrund der höheren Fingeranzahl zu reduzieren. Eine Anpassung der Silberpastenformulierung ist für beide Technologien jedoch erforderlich, um zusätzliche Kontaktwiderstandsverluste bei verringerter Fingerbreite zu vermeiden.

Diese Arbeit liefert Richtlinien für das Design von Pasten- und Filmmaterialien, die auf schmalere Silber-Elektroden mittels PTP-Technologie abzielen. Die Bewertung der PTP-Technologie für photovoltaische Anwendungen in dieser Arbeit zeigt, dass die mittels PTP gedruckten ultrafeinen Silber-Elektroden für die Vorderseitenmetallisierung von Silizium-Solarzellen geeignet sind, was den Silberverbrauch erheblich reduziert und gleichzeitig den Zellwirkungsgrad im Vergleich zur industriellen Siebdrucktechnologie erhöht.

Table of Contents

Acknowledgements .... **i**

Abstract .... **iii**

Zusammenfassung .... **v**

Table of Contents .... **vii**

Abbreviations and Symbols .... **xi**

1 Introduction **1**

- 1.1 Background and motivation 1
- 1.2 Aim of the thesis 2
- 1.3 Structure of the thesis 3

2 Basic Principles and State of the Art **5**

- 2.1 Working principle of c-Si solar cells 5
  - 2.1.1 Structure and process flow of PERC solar cells 5
  - 2.1.2 Electrical and optical losses of solar cells 7
- 2.2 Various deposition methods for the front finger metallization of c-Si solar cells 8
  - 2.2.1 Flatbed screen-printing 8
  - 2.2.2 Rotary screen-printing 11
  - 2.2.3 Dispensing 11
  - 2.2.4 Plating 12
  - 2.2.5 Laser printing technologies 12
- 2.3 Pattern Transfer Printing Technology 13
- 2.4 Rheological properties of thick-film-Ag paste 15
  - 2.4.1 Thick film Ag paste for the front metallization of c-Si solar cells 15
  - 2.4.2 Typical rheological properties of thick-film Ag paste 16
- 2.5 Front contact formation 18
- 2.6 Characterization methods 19
  - 2.6.1 Solar cell 19
  - 2.6.2 Paste rheological properties 24

3 Development of Pattern Transfer Printing Technology **27**

- 3.1 Impact of squeegee configuration for the filling process 27
  - 3.1.1 Experimental details 28
  - 3.1.2 Results and discussions 28
- 3.2 Influence of laser power on the print quality of PTP 29
  - 3.2.1 Experimental details 30
  - 3.2.2 Results and discussions 30
- 3.3 Investigation of laser-induced damage 34
  - 3.3.1 Experimental details 34

3.3.2 Results and discussions ... 34
3.4 Chapter summary ... 37

4 Film Material and Rheological Paste Properties for PTP Application ... 39

4.1 Introduction ... 39
4.2 Materials ... 40
4.2.1 Silver pastes ... 40
4.2.2 Transparent polymer films ... 40
4.3 Experimental details ... 41
4.4 Results and discussions ... 42
4.4.1 Influence of paste yield stress on finger geometry ... 42
4.4.2 Influence of trench design on laser power threshold and printed finger geometries ... 44
4.4.3 Influence of organic vehicle on silver paste regarding its relationship to laser threshold ... 47
4.4.4 Investigation of film materials and thickness regarding how it relates to laser threshold ... 48
4.5 Chapter summary ... 50

5 PTP Application for Front Surface Metallization of c-Si Solar Cells ... 53

5.1 Screen-printing reference ... 53
5.1.1 Experimental details ... 53
5.1.2 Results and discussions ... 54
5.2 Benefits of PTP technology for front metallization ... 57
5.2.1 Experimental details ... 57
5.2.2 Results and discussions ... 58
5.3 Optimization of metal grid design for PTP ... 62
5.4 Current status of screen-printing technology ... 65
5.4.1 Experimental details ... 67
5.4.2 Results and discussions ... 68
5.5 Implementation and Challenge of PTP into PV metallization line ... 75
5.6 Chapter summary ... 77

6 Impact of Sheet Resistance and Paste Volume on Contact Resistance ... 81

6.1 Influence of sheet resistance on contact resistance ... 81
6.1.1 Experimental details ... 81
6.1.2 Results and discussions ... 82
6.2 Impact of paste volume and grid pattern on the contact resistance ... 86
6.2.1 Experimental details ... 86
6.2.2 Results and discussions ... 87
6.2.3 Chapter summary ... 90

7 Summary and Outlook ... 93

7.1 Summary ... 93
7.2 Outlook ... 97

Bibliography 99

Appendix 111

List of publications 113

Abbreviations and Symbols

Abbreviations

Ag	Silver
Al	Aluminum
Al-BSF	Aluminum back surface field
AlO_x	Aluminum oxide
ARC	Antireflection coating
B	Boron
CLSM	Confocal laser scanning microscopy
CO_2	Carbon dioxide
c-Si	Crystalline silicon
Cu	Copper
Cz	Czochralski method
DSC	Differential scanning calorimetry
ECV	electrochemical capacitance-voltage
EL	Electroluminescence
EQE	External quantum efficiency
EOM	Emulsion over mesh
I-V	Current-voltage
LCO	Laser contact openings
LIFT	Laser-induced forward transfer
LTP	Laser transfer printing
MPP	Maximum power point
Ni	Nickel
P	Phosphorus
PECVD	Plasma-enhanced chemical vapor deposition
PERC	Passivated emitter and rear cell

PL	Photoluminescence
PSG	Phosphosilicate glass
PTP	Pattern transfer printing
PV	Photovoltaic
REACH	Registration, Evaluation, Authorization and Restriction of Chemicals
SEM	Scanning electron microscopy
Si	Silicon
SiN_x	Silicon nitride
SiO_x	Silicon oxide
SP	Screen-printing
STC	Standard test conditions (1000 $W \cdot m^{-2}$, air mass 1.5 global spectrum and 25 °C)
SWCT	Smart Wire Interconnection Technology
TLM	Transfer length method
vs.	Versus

Symbols

A_{finger}	Finger cross-sectional area	[μm^2]
AR	Finger aspect ratio	[1]
c	Velocity of light	[$m \cdot s^{-1}$]
d	Distance between substrate and polymer film of PTP	[µm]
d_c	Contact distance between two Ag fingers	[mm]
E	spectral irradiance	[$W \cdot m^{-2}$]
FF	Fill factor	[%]
h	the Planck´s constant	[$W \cdot s^2$]
g	acceleration due to gravity	[$m \cdot s^{-2}$]
I	Current	[A]
J_0	Dark saturation current density	[$fA \cdot cm^{-2}$]
$J_{0,\text{met}}$	Dark saturation current density underneath the metal contacts	[$fA \cdot cm^{-2}$]

J_{MPP}	Current density at maximum power point	$[\mathrm{mA \cdot cm^{-2}}]$
J_{sc}	Short-circuit current density	$[\mathrm{mA \cdot cm^{-2}}]$
L	Width of contact finger for contact resistivity measurement	[µm]
L_{T}	Transfer length	[µm]
N_{f}	Number of fingers in a solar cell	[-]
p	Pressure	[Pa]
pFF	Pseudo fill factor	[%]
P_{Max}	Peak power of a solar cell (at maximum power point)	[W]
q	elementary charge	[A·s]
$r_{\mathrm{c/h}}$	Ratio between the trench circumference and the equivalent horizontal area	[1]
R_{Emitter}	Sheet resistance of emitter	[Ω/sq]
R_{C}	Contact resistance	[Ω]
R_{F}	Lateral finger resistance	[Ω/cm]
T	Temperature	[°C]
V	Voltage	[mV]
V_{oc}	Open-circuit voltage	[mV]
V_{T}	Thermal voltage	[mV]
w_{f}	Electrode finger width	[µm]
Z	Length of contact finger for contact resistivity measurement	[mm]
γ	Deformation	[-]
η	Conversion cell efficiency	[%]
λ	Wavelength	[nm]
ρ_{c}	Contact resistivity	$[\mathrm{m\Omega \cdot cm^{2}}]$
ρ_{paste}	Density of paste	$[\mathrm{kg \cdot m^{-3}}]$
σ	Standard deviation	
τ	Shear stress	[Pa]

1 Introduction

This chapter provides the background of and motivation for the thesis. It presents the current trend in the PV market and the reduction in the use of silver for the metallization of crystalline silicon solar cells. The main objectives of the thesis are also illustrated and described. Additionally, the outline of this thesis is introduced.

1.1 Background and motivation

As a result of global warming caused by human activity, climate change has become a major global issue that worsens the condition of the climate and causes catastrophic weather events around the world. In line with the Paris Agreement [1], many countries have been striving to limit the global temperature increase to within 2 °C before 2050 by decarbonizing the energy system. A transition from fossil power plants to renewable energy sources, such as wind energy, solar energy, hydropower, geothermal, and biomass, will generate electricity with zero CO_2 emissions, resulting in considerable reductions in global warming. However, decarbonizing the energy system requires a high level of capital expenditure and a massive transformation of the energy system from centralized to decentralized generation.

Many studies about the energy roadmap and outlook have suggested that solar photovoltaic (PV) technology will serve as one of the foundations for future renewable electricity supply systems in the most cost-efficient way [2]–[6]. The term "photovoltaic" describes a direct conversion of sunlight into electricity using a semiconductor technology known as a solar cell. In the last few years, the number of global PV installations has steadily increased. Even though the world economy in 2020 suffered due to a global pandemic, the number of solar PV installations worldwide broke the annual installation record with a total capacity of 126.7 GW, growing 22% from the previous year and reaching a total PV installed capacity of 707.5 GW worldwide [7], [8]. This increased the PV electricity share of gross electricity consumption to 2.7% of the total global electricity consumption in 2020 [8].

The global PV installation is expected to increase exponentially in the coming years as PV technology has already reached a high level of technical maturity for mass production. Furthermore, PV has been proven to be the cheapest source of electricity generation in history compared with other sources, such as coal, oil, gas, wind, and nuclear [5]. The International Renewable Energy Agency (IRENA) reported that 14,000 GW of solar photovoltaics need to be installed by 2050 to limit global warming to 1.5 °C, which requires a fourfold increase in annual solar PV installations [6]. A recent study by Bogdanov *et al.* with a more ambitious scenario concluded that a global 100% renewable energy system with zero CO_2 emissions can be reached with PV serving as the primary energy source providing 76% of the total energy supply by 2050, for which global PV installations of approximately 63,380 GW are required [9].

Over the last few decades, the global PV market has been dominated by crystalline silicon (c-Si) technology due to its abundant supply, non-toxicity, high stability, and cost competitiveness [10], [11]. Solar cells based on c-Si technology accounted for 95% of the global PV production in 2020 [8]. Silicon solar cells contain precious metals, such as silver and copper; silver plays a critical role in the metallization stage for collecting and transporting the generated electrons, and copper is used for the interconnection of solar cells in PV modules. The global silver demand for PV industries has increased significantly in the last seven years. In 2014, around 4.5% of global silver supply was destined for the solar PV industry, and it increased to 10.4% of the total global silver supply in 2020 due to a steady increase in the PV module production rate [12]. With the projected growth of PV, it is expected that the global demand for silver in the PV industry will rise significantly in the coming years. This may lead to an increase in the price of silver due to the cap on annual primary silver production and the supply chain problems of silver caused by its relative scarcity.

To reduce silver consumption and further lower PV production costs, it is necessary to fabricate smaller silver electrodes for the front metallization of c-Si solar cells. Smaller front electrodes cause not only less shading but also higher losses due to an increase in series resistance. Hence, it is possible to increase cell efficiency by optimizing the front metallization. The most common technology used to fabricate silver electrodes in mass production is screen-printing technology. Constant advancement in screen-printing technology together with a steady breakthrough in silver paste research have allowed a rapid reduction of the silver loading per cell from 300 mg in 2010 [13] to 90 mg in 2020 [14]. Despite this, silver is still the second most expensive material in c-Si solar cell production after silicon itself, accounting for about 60% of the non-Si cell price [14].

Nevertheless, it is forecast that PV industries will require ten years to reduce the width of the front silver electrodes from the current width of 36 µm to 20 µm for c-Si solar cells, which is equal to a silver reduction from 90 to 50 mg per cell, respectively [14]. A smaller screen aperture will limit silver consumption, and at the same time, reduce the open area inside the screen aperture region, resulting in inhomogeneous electrode lines caused by existing knots and wires. Silver paste development is also required to improve paste transfer and maintain a good contact formation with an even smaller silver amount. Therefore, alternatives to screen-printing technology for the front metallization of c-Si solar cells are undoubtedly an attractive way to limit the massive increase in silver demand resulting from a scarce global supply of silver in the future.

1.2 Aim of the thesis

This thesis deals with the fabrication of silver electrodes for front metallization of c-Si solar cells and explores methods to reduce silver consumption while preserving the electrical characteristics necessary for an efficient solar cell. One of the alternatives to standard screen-printing technology is Pattern Transfer Printing (PTP), which has been developed by Utilight Ltd. (currently called DR Utilight Corp Ltd.) in Yavne, Israel. PTP technology utilizes polymer films as paste carriers and fabricates silver electrodes using a contactless laser transfer process. In 2015, Lossen *et al.*

demonstrated that PTP technology could produce silver electrode lines with an average width of 27 µm for the front metallization of c-Si solar cells [15].

The first part of this thesis focuses on developing and optimizing PTP technology to further improve the laser transfer process, targeting silver electrodes with a width of 20 µm and an aspect ratio above 0.5. Various silver pastes with different rheological properties and several polymer film materials with different material properties are studied to better understand their influences on PTP application in achieving an even narrower electrode line. In the second part of the thesis, the performance of PTP technology for the front metallization of c-Si solar cells is assessed and compared with industrial screen-printing technology. Their finger shape, electrical properties of the solar cells, and the difference in silver paste consumption between both technologies are analyzed. Furthermore, the effect on contact formation of ultrafine fingers obtained with PTP technology is investigated. By maintaining a good contact formation for PTP finger lines, the full advantage of PTP fingers can therefore be taken, leading to not only a lower production cost resulting from lower silver consumption but also higher cell efficiency caused by less shading at the cell front side without a significant increase in series resistance.

1.3 Structure of the thesis

Chapter 1 offers a brief introduction regarding the market trend and the urgency of silver reduction in the PV industry, clarifying the background and motivation of this thesis. Furthermore, the aims of this work are described.

Chapter 2 provides background for understanding the front metallization process of crystalline silicon (c-Si) solar cells. The basic principle of c-Si solar cells is introduced, followed by a description of the typical structure of c-Si solar cells and its process flow in mass production. Additionally, the front metallization step is discussed and several front metallization technologies are outlined, such as flatbed screen-printing, rotary screen-printing, laser printing technologies, dispensing, and plating. The principle of Pattern Transfer Printing (PTP) technology is presented and explained in detail. Furthermore, the components of silver pastes are examined, and the general rheological properties of thick-film silver paste are discussed. The theory of contact formation for the front metallization of c-Si solar cells is also introduced. Afterward, the state-of-the-art characterization methods for solar cells and the rheological properties of silver paste are reviewed.

In **chapter 3**, the development and optimization of PTP technology are presented. Two steps of the PTP printing sequence, namely the printing process and transfer process, are separately optimized. The impact of squeegee blade angle on the quality of the filling process of thick-film silver paste is examined. The effect of laser power on the laser transfer process of PTP is investigated, showing the importance of laser power optimization for an excellent finger geometry of PTP-metallized cells. Furthermore, three possible cases during the laser transfer process are determined, and two terms, "optimum laser power" and "laser power threshold," are defined. Additionally, the front surface passivation quality of c-Si solar cells after the laser transfer process of PTP technology is investigated for any possible laser-induced damage during the paste transfer process.

Chapter 4 focuses on two key aspects that control the laser transfer process from a materials point of view, namely the physico-chemical properties of silver paste and film material, aiming for a better understanding of the laser deposition process for PTP application. Different silver pastes are investigated to identify the effect of rheological properties on printed finger geometry for PTP application. Various shapes of pre-embossed trenches on the polymer film surface are tested, and their impact on finger shape and laser transfer process are analyzed. Furthermore, different materials and thicknesses of polymer film are also investigated.

Chapter 5 presents the application of PTP technology for the front metallization of c-Si solar cells with passivated emitter and rear cell (PERC) structure, where technology assessment of PTP is conducted as an alternative to screen-printing technology. Finger profiles and electrical performance of the solar cells fabricated using PTP technology are evaluated and compared later with the state-of-the-art screen-printing technology as reference. The advantages and challenges of PTP application in mass production are discussed. Additionally, the current status of screen-printing technology on the research level is presented and discussed.

In **chapter 6**, the influence of emitter sheet resistance on cell efficiency and contact formation is discussed. Furthermore, the effect of silver paste volume on contact formation is also studied. Finally, two different metallization approaches are presented to examine their impact on the contact formation of PERC solar cells.

Chapter 7 concludes this work with a summary presenting the main results regarding the development of PTP processes and the evaluation PTP technology as an alternative to the industrial-standard screen-printing technology for the front metallization of c-Si solar cells. Furthermore, an outlook with potential ideas and possible experimental direction for future research is presented, serving as a valuable guideline for further PTP improvement and optimization aimed at even narrower silver fingers.

2 Basic Principles and State of the Art

This chapter provides basic principles to understand the requirements of the front metallization process of crystalline silicon solar cells. Firstly, the fundamental function of a standard c-Si solar cell is introduced and followed by the typical structure of c-Si solar cells and its process flow in mass production. Furthermore, the front metallization step of c-Si is discussed, and available technologies for the front metallization are presented, such as standard screen-printing technology, Pattern Transfer Printing (PTP) technology and others. The components of silver pastes are described, and the typical rheological properties of thick-film silver paste are discussed. Next, the theory of the contact formation for the front metallization of silicon solar cells is explained. Finally, the state-of-the-art characterization methods of solar cells and rheological properties of silver pastes are presented.

2.1 Working principle of c-Si solar cells

Solar cells based on crystalline silicon (c-Si) have been dominating the PV world market. After holding the highest market share over the last few decades, the standard aluminum back surface field (Al-BSF) solar cells were surpassed by the *p*-type passivated emitter and rear cell (PERC) solar cells in 2019 [16]. The rear passivation with dielectric layer stacks of PERC technology improves the cell efficiency significantly [17]. Furthermore, high compatibility with existing production lines of *p*-type Al-BSF solar cells has made PERC technology on *p*-type monocrystalline silicon the dominant cell technology in mass production [14]. In this thesis, all investigations are conducted on PERC solar cells, which are now the industrial standard cell technology in mass production.

2.1.1 Structure and process flow of PERC solar cells

Figure 2.1 shows the typical industrial *p*-type PERC solar cell structure and its process flows in mass production. First, a *p*-type c-Si wafer doped with boron or gallium is chemically etched to remove any surface damage caused by diamond-wire-sawing on (c-Si) wafers [18]–[20]. This is followed by texturing step in an alkaline etch solution to reduce reflection of the incident photons and increase the path length of the photon inside the Si layer. An *n*-type emitter is formed by diffusing phosphorus atoms into the *p*-type wafer, creating a diffused *p*-*n* junction. The rear surface pyramids are partly polished with a wet chemical etching process, which simultaneously removes the rear phosphorus-doped layer. After the chemical etching of phosphosilicate glass (PSG) layer on the front surface, the rear side is passivated with an aluminum oxide/silicon nitride (AlO_x/SiN_x) stack. The AlO_x layer has been proven to be an excellent passivation layer for *p*-type silicon surfaces due to its high negative fixed charge density [21]. The capping layer SiN_x enhances the optical properties of the rear surface by increasing the infrared light absorption due to better light trapping [22]. A silicon nitride (SiN_x) layer on the front surface serves as an antireflection coating (ARC) and a passivation layer. The rear dielectric layers are locally removed by laser ablation, creating laser contact openings (LCO). Silver solder pads and Al thick-film paste are screen-printed on the rear, while the metallization of silver (Ag) for front contacts and busbars is conducted on the front side. A sintering process at a peak temperature between 750 and 850 °C results in the Ag front contacts and the Al contacts with local Al-BSF, which hinders the recombination of charge carriers at the rear contacts caused by p/p^+ high-low junction [21].

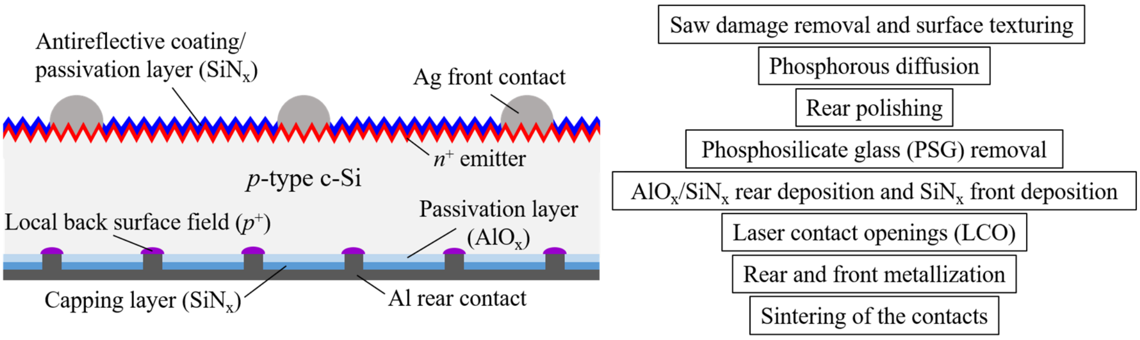
Antireflective coating/
passivation layer (SiN_x)
Ag front contact
n^+ emitter
p-type c-Si
Local back surface field (p^+)
Passivation layer (AlO_x)
Capping layer (SiN_x)
Al rear contact
Saw damage removal and surface texturing
Phosphorous diffusion
Rear polishing
Phosphosilicate glass (PSG) removal
AlO_x/SiN_x rear deposition and SiN_x front deposition
Laser contact openings (LCO)
Rear and front metallization
Sintering of the contacts

Figure 2.1: An industry-typical cell concept of a p-type passivated emitter and rear cell (PERC) structure with local back surface field (BSF) and AlO_x/SiN_x layer stack for rear passivation; left: schematic drawing of a PERC solar cell structure (not drawn to scale); right: typical production process flows of an industrial PERC solar cell.

When sunlight irradiates the solar cell, its photon energy is absorbed by the bulk of solar cells generating electron-hole pairs randomly across the emitter and base region of a solar cell. The electrical field at the p-n junction drifts the generated electron through the emitter to the front finger contacts, and the generated holes to the base and the rear contacts. The metal contacts on both surfaces collect the generated charge carriers and transport them to the current collector lane, called busbar. The electrons flow and the generated electrical energy can be used by connecting the solar cell with a load to the two poles of solar cells. More details regarding the physics of solar cells are described by Goetzberger *et al.* [23], Mertens [24] or Würfel and Würfel [25]. The open-circuit voltage, the short-circuit current, the fill factor and the conversion cell efficiency are the main parameters that represent the performance of solar cells. These parameters are determined from the I-V curve under illumination using a flash-type solar simulator.

Open-circuit voltage (V_{oc}) is the maximum voltage obtainable from a solar cell when the load resistance is infinitely high ($I = 0$) and no current flows between the two polarities of a solar cell. The recombination of carriers in the solar cell determines the V_{oc} value, and it can be improved by reducing the dark saturation current density of a solar cell caused by recombination.

Short-circuit current (I_{sc}) describes the maximum current that can be generated from a solar cell in the short-circuit condition ($V = 0$). For homogeneous solar cells, the short-circuit current is proportional to the area of the solar cell. To achieve a parameter that is independent of the solar cell area, the parameter short-circuit current density (J_{sc}) is generally used in many studies. J_{sc} is affected by optical losses of solar cells due to shading and reflection. Hence, J_{sc} can be improved by increasing the active cell area with narrow fingers and reducing the reflection with a good ARC layer and surface texture.

Peak power (P_{Max}) is the highest possible power output from a solar cell at the maximum power point (MPP) on the *I-V* curve of a solar cell.

Fill factor (*FF*) is defined as the ratio between the maximum power of a solar cell at the MPP and the product of V_{oc} and J_{sc}. *FF* can be improved by minimizing the power losses due to series and parallel resistances of a solar cell.

Conversion cell efficiency (η) describes the maximum possible energy conversion rate of a solar cell from the light energy as input energy to the generated electrical energy as output energy. Kerr *et al*. investigated the ultimate cell efficiency of silicon solar cells and showed that the highest cell efficiency achievable by a single *p-n* junction silicon solar cell is 29.43% due to the material limitation of silicon to absorb all solar spectrum, radiative recombination and the Auger recombination [26].

2.1.2 Electrical and optical losses of solar cells

The reduction of power as a result of an electrical loss is affected by the parasitic resistances of the solar cells, which are described as shunt and series resistance. The shunt resistance of solar cells influences the V_{oc}, and a small shunt resistance also leads to a decrease in *FF* and cell efficiency. A small shunt resistance might be caused by the low-ohmic defect at the *p-n* junction, current leakage at the cell edges, material, or manufacturing defects [27], [28]. On the other hand, the series resistance influences the J_{sc}, and must be maintained low. A high series resistance also decreases the *FF* and cell efficiency resulting in a significant power loss of solar cells.

In Figure 2.2, all contributors to the series resistance of silicon solar cells are presented. The light-generated current flows from the emitter and the base through the internal resistance of a solar cell. It is then collected by full Al layer on the rear and Ag fingers connected to busbars forming an H-grid pattern on the front. As the busbars on the front and the full Al layer on the rear are contacted directly with the pins during the *I-V* measurement, the resistance of the solder joint and the resistance of Ag/Al pads are neglected in this thesis. Therefore, the total series resistance of a solar cell can be described as the sum of the lateral resistance of busbar, lateral resistance of Ag finger, contact resistance of Ag finger to the emitter, resistance of emitter, resistance of base, contact resistance of Al to the base and lateral resistance of Al layer. A more detailed description of each contributor to the total series resistance can be found in Goetzberger *et al*. [23]. In this thesis, the pre-processed industrial PERC solar cells came from the same production batch, highlighting the critical parameters are series resistance, mainly contact resistance and finger lateral resistance.

Not all incident light is absorbed by c-Si solar cells due to the reflection, the silicon band gap of 1.12 eV, as well as the front shading of Ag fingers and busbars. Low absorption of incident light leads to a lower current generation of solar cells. Several procedures are optimized to minimize the optical losses of a solar cell: texture on the front and optimization of antireflection coating at the front and rear side to create a light trapping effect, and a further reduction of the total metal fraction on the front side. The narrower width of Ag fingers with a high aspect ratio (ultrafine finger lines) allows a minimal optical shading loss resulting in a J_{sc} gain and a minimal lateral finger resistance due to a high cross-sectional area to minimize the *FF* loss. Hence, a higher cell efficiency can be achieved.

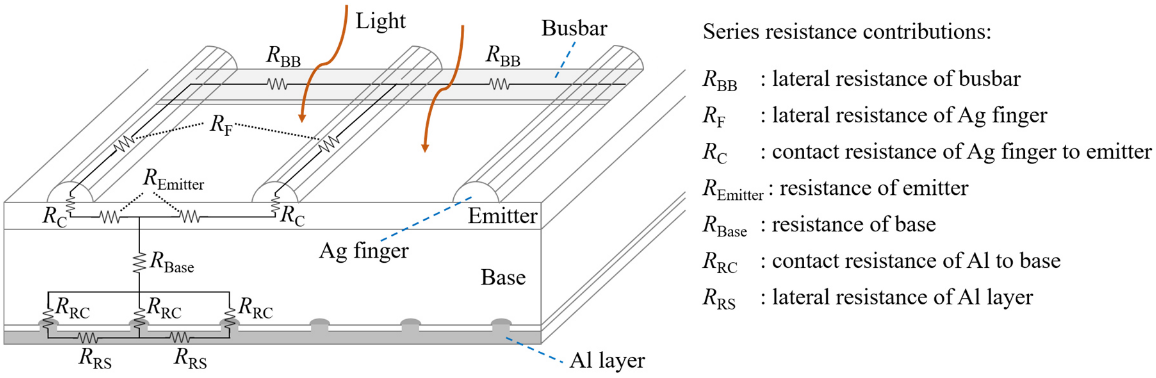
Light
Busbar
R_{BB}
R_{BB}
R_F
$R_{Emitter}$
R_C
R_C
Emitter
Ag finger
Base
R_{Base}
R_{RC}
R_{RC}
R_{RC}
R_{RS}
R_{RS}
Al layer
Series resistance contributions:
R_{BB} : lateral resistance of busbar
R_F : lateral resistance of Ag finger
R_C : contact resistance of Ag finger to emitter
$R_{Emitter}$: resistance of emitter
R_{Base} : resistance of base
R_{RC} : contact resistance of Al to base
R_{RS} : lateral resistance of Al layer

Figure 2.2: Illustration of various resistance contributions to a total series resistance in a PERC solar cell, excluding the resistance of solder joint on the front and resistance of rear Ag/Al pads on the rear. The total series resistance of a solar cell is the sum of the lateral resistance of busbar, lateral resistance of Ag finger, contact resistance of Ag finger to the emitter, resistance of emitter, resistance of base, contact resistance of Al to the base, and lateral resistance of Al layer. The optical losses are influenced by the metal fraction on the front blocking the incident light by Ag fingers and busbars.

2.2 Various deposition methods for the front finger metallization of c-Si solar cells

Metal contacts of solar cells are mandatory for the collection of the generated current and interconnection. The metallization process starts with the deposition of respective pastes on the rear and front surfaces, followed by a drying step. During the drying step, the thermal heat from infrared lamps heats the paste, and the solvents inside the paste are therefore evaporated, transforming the wet paste into a solid form. After each printing step, a drying step is essential to prevent the contamination of different metal paste in the several printing sequences from the rear to the front surface of the solar cells. Afterward, the sintering step in a fast-firing furnace initiates the reaction between the pastes and the cell surface, creating proper ohmic contacts for both sides. Finally, a working solar cell is produced. The front metallization is more challenging than the rear since narrower metal contacts with a good shape are vital to achieve a lower optical loss, as discussed in the previous section.

2.2.1 Flatbed screen-printing

Since the beginning of mass production of c-Si solar cells, flatbed screen-printing technology has been dominating the PV market due to its simplicity, robustness and cost-effectiveness. As shown in Figure 2.3, the flatbed screen-printing process divides into two steps: flooding and printing. First, a metal squeegee floods the mesh inside the screen opening with the paste due to the squeegee angle of 90° towards the screen. This flood squeegee is set to have a space with the screen (called down stop) so that the screen is not pushed toward the substrate underneath. The flooding step fills all open areas of the screen with paste homogeneously. The second squeegee made from rubber pushes down the paste through the mesh opening in the opposite direction of the flood squeegee. This squeegee with a defined pressure rolls the paste and pushes the screen down until the screen and paste contact the substrate in the cling zone. The tension of the screen is lessened after the squeegee pressure is withdrawn along the printing direction, allowing the screen to return to its snap-off height and leaving the substrate with the desired paste pattern. The snap-off height is the distance between the screen and the substrate, and it must be adjusted to achieve the best possible finger shape and avoid misprint, while it is kept as low as possible to reduce the deformation of the screen and the wearing of the screen.

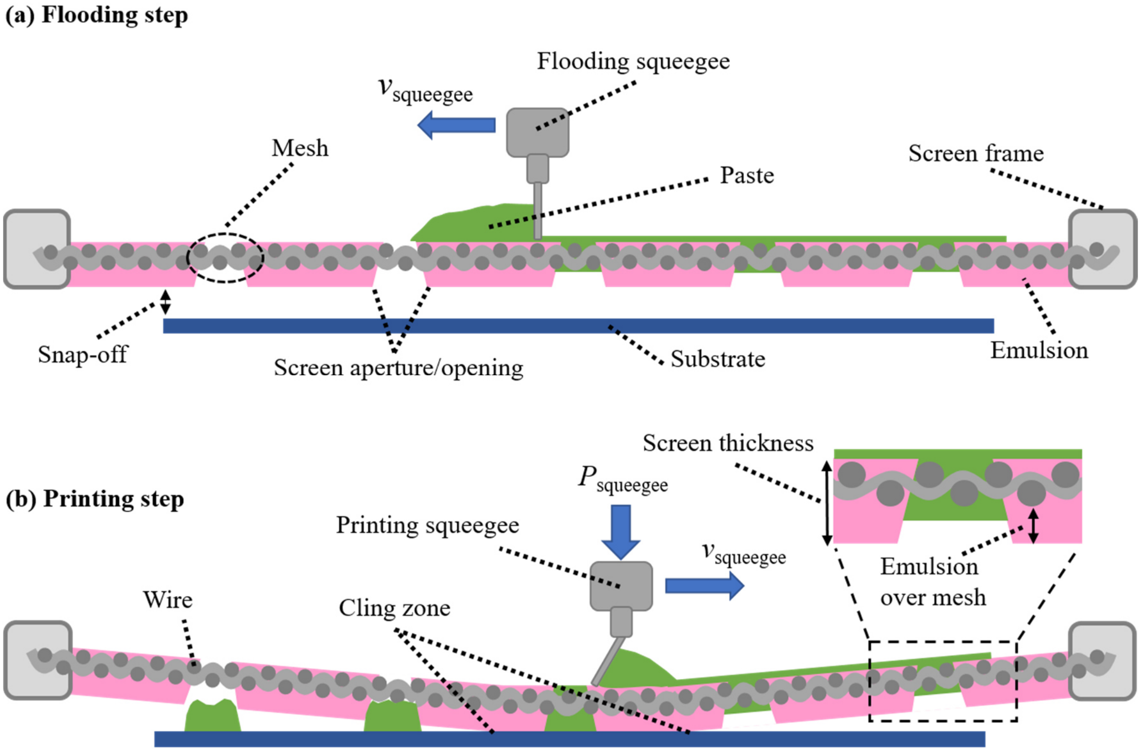
(a) Flooding step
Flooding squeegee
v_{squeegee}
Mesh
Paste
Screen frame
Snap-off
Screen aperture/opening
Substrate
Emulsion
(b) Printing step
Screen thickness
P_{squeegee}
Printing squeegee
v_{squeegee}
Emulsion over mesh
Wire
Cling zone

Figure 2.3: Illustration of two printing steps of flatbed screen-printing technology: (a) flooding step; (b) printing step.

Squeegees with hardness ranging from 65° to 90° Shore are generally used for screen-printing. The lower the squeegee hardness, the more paste is pushed through the screen opening as the deformation of the squeegee is stronger. Hence, the pressure per area is lower and it can adapt better to uneven surfaces. A more rigid squeegee has a lower deformation and is chosen if high pressure is necessary during the screen printing and a thinner print is desired. The angle of the printing squeegee is usually set between 45° and 60° to apply sufficient hydrodynamic pressure to the paste in front of the squeegee that allows the paste to pass through the screen meshes onto a substrate, as studied by Riemer [29]. The squeegee pressure affects the paste laydown, the shape and the uniformity of Ag fingers. An inadequate pressure could either fail to wipe the paste clear from the screen surface or push the screen into contact with the substrate in a particular area that reduces the finger uniformity. However, an excessive squeegee pressure will allow the squeegee to enter the screen aperture and scoop out the paste thus removing the paste and decreasing the overall paste amount and the aspect ratio. The printing speed also influences print quality since different printing speed results in various dynamic pressure to the paste, which affects the paste properties. A printing speed from 300 to 400 $mm \cdot s^{-1}$ is typically adopted for high throughput in industrial PV production lines.

A standard mesh screen consists of a mesh of fine wires, which is stretched with a pneumatic system until the optimal screen tension (typically around 20 to 23 $N \cdot cm^{-1}$), to ensure a sufficient paste release mechanism related to the mesh count, the wire diameter and the total mesh thickness. The mesh count describes the number of wires per unit length. Afterward, the mesh is coated with a screen emulsion, and the non-printable area is polymerized and solidified with UV light via photolithography method. The emulsion in the location of the screen opening is, however, still soft and soluble in water because it is protected by the printing motive from the UV light. Thus, the screen opening is cleared by washing the screen with water. The thickness of the emulsion, defined as emulsion over mesh (EOM), can be controlled by adjusting the light intensity, the exposure time and the emulsion specifications, such as spectral sensitivity and water content. Typically, a narrow screen opening has a lower EOM than a screen with a broader opening to mitigate the flow resistance of the paste affecting the shape and the aspect ratio of the finger [30].

Nevertheless, an adequate height of EOM is required to limit the mesh effect on the printed fingers and to achieve a decent finger aspect ratio [31]. The screen thickness is the sum of the mesh thickness and the EOM. The open area of the screen opening is related to the mesh count, wire diameter and mesh angle. An angle of 22.5° between the screen opening and the mesh is chosen for state-of-the-art screens, providing higher screen stability, better shape and less interference between the meshes inside the screen opening than other angle configurations [32]–[34]. To generate the best print quality on the surface of solar cells, a careful adjustment and optimization of printing parameters, i.e., snap-off height, squeegee angle, squeegee hardness, printing speed and printing pressure, as well as screen parameters, i.e., mesh count, wire diameter, mesh angle, screen tension, EOM, emulsion type and coating, are required since all parameters are interdependent.

Another type of screen, called stencil, can be used for the same screen-printing technology. The stencil is referred to the framed and tensioned metal foil with an opening at the printable area. The metal foil has a specific thickness and is generally electroformed or laser cut. Apart from mesh screens, the open area of stencils is 100% due to missing mesh/wire in the opening region. Thus, a higher paste transfer and finer fingers with a better uniformity can be achieved. Yet, a typical finger pattern for solar cells, composed of many long parallel openings, constitutes a challenge for stencil printing, as the mask gets mechanically unstable, if bigger sections of the mask are connected by only small bridges. Although several positive results of stencil printing for front metallization application of silicon solar cells were published [35]–[38], this technology is not applied in the industrial PV production line due to several drawbacks: the suitable electroformed stencils are relatively expensive and exhibits only limited lifetime, requiring excessive cleaning effort, and further slumping of the paste under the stencil and local finger broadening from possible dust particles between substrate and stencil leading to a lower production yield [39].

2.2.2 Rotary screen-printing

The rotary screen-printing method utilizes a cylindrical screen from a woven mesh of thin metal wires. To ensure screen stability, this cylindrical screen requires thicker wires than the standard flatbed screen [40], [41]. The printing step of rotary screen-printing is illustrated in Figure 2.4. The paste is placed inside the cylindrical screen. The screen is rotated at a certain speed, and the paste is transferred through the screen aperture onto the substrate using an immovable squeegee. The substrate is mounted on a moving belt in the same direction as the screen rotation. By using rotary screen-printing, the productivity output can be increased to 0.45 s per cell from one or two seconds per cell (standard throughput of industrial screen-printing technology) [42]. Thus, the throughput of 8000 cells per hour can be achieved. A handful of results related to the rotary screen-printing for the front metallization of silicon solar cells have been published [41]–[44], but the less uniform fingers due to thicker wires and a low finger height are quite challenging to compete with established flatbed screen-printing technology.

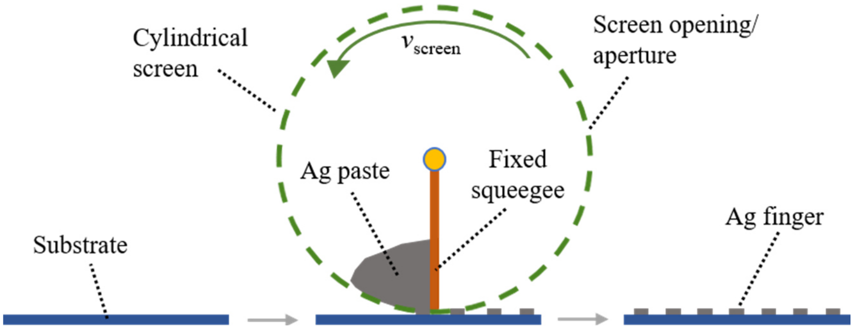

Figure 2.4: Illustration of a rotary screen-printing setup for the finger metallization of silicon solar cells. This figure is adapted and retrofitted from Lorenz *et al*. [41].

2.2.3 Dispensing

Dispensing technology utilizes pressure generated from jetting valves or pump to force a paste out through nozzles with narrow openings. To fabricate 100 continuous finger lines in two strokes, a printing head with 50 nozzles was used and moved up and down towards a substrate at a moving speed of 650 $\text{mm}\cdot\text{s}^{-1}$ fabricating homogeneous fingers with an average width of 35 µm [45]. The nozzle diameter determines the width of the fingers. The smaller the nozzle diameter, the narrower the Ag fingers and the higher the pressure required to push the paste through, ensuring the same mass flow rate as the larger nozzle diameter [45]. Pospischil *et al*. presented an average finger width of 17 µm fabricated with dispensing technology using nozzles with a diameter of 20 µm on PERC solar cells [46]. The rheology of Ag paste affects the dispensing parameter and the finger geometries; a higher paste yield stress resulted in a better finger aspect ratio, but a higher dispensing pressure was required to extrude the paste out the nozzles completely without any interruptions [47]. Starting and stopping the dispensing process in mass production is generally a challenge. However, a recent study showed that an intermittent dispensing process with precise positioning of endpoints was possible at a printing speed up to 300 $mm \cdot s^{-1}$ for an entire cell area of 156 mm × 156 mm with a total printing time of 1.1 s per cell [48].

2.2.4 Plating

Plating technology is presented as an alternative for screen printing technology mostly under the motivation of reducing the production cost. Using the plating method, copper can be chosen as the primary conducting material instead of silver. Copper (Cu) has the second-highest electrical conductivity of all elements after Ag, but Cu is far cheaper than Ag [49]. A process sequence of Cu plating that might be possible for the front metallization of c-Si solar cells was described by Horzel *et al.* [50]: the rear metallization is conducted firstly using screen-printing technology then followed with sintering process. Laser irradiation is utilized to locally ablate the front SiN_x dielectric layer forming a contact pattern. Afterward, the sample is cleaned to reduce the laser damage, and nickel (Ni) is plated on the ablated pattern. Then, the plating process is followed with Cu. Ni serves as a barrier layer between Cu and Si to prevent Cu diffusion into Si that can significantly reduce the minority carrier lifetime. The third plating process coats Cu with a thin layer of Ag to avoid oxidation of Cu under normal air conditions. Finally, the Ni-Cu-Ag metal stack is annealed at moderate temperature, forming nickel silicide to improve the mechanical contact adhesion and the contact resistance of front contact fingers. An industrial process of one-sided light-induced plating of Ni-Cu-Ag was introduced by Rena Technologies GmbH [51], [52] or Kuttler plating bath [53]. It might have a throughput up to 5000 wafers per hour. Until now, plating could not gain a significant market share due to several challenges [54], i.e., higher cost of ownership, adhesion strength of contact fingers, process complexity, etc.

2.2.5 Laser printing technologies

Apart from destructive processes, such as scribing [55]–[58] and ablation [59]–[62], lasers can also be applied for the metallization process in PV industries. Until now, three different laser printing methods have been published for the front metallization of silicon solar cells: laser-induced forward transfer (LIFT) [63]–[66], laser transfer printing (LTP) [67]–[69], and pattern transfer printing (PTP) [15], [70]–[72]. The principle behind these three technologies is similar. First, a transparent carrier is coated with a metallic donor material, which can be in a solid form, pastes (high viscosity liquid), or inks (low viscosity liquid). Then, a laser irradiates the donor material to be transferred through the transparent carrier. Through the heat absorption by the donor material, a pressure is generated at the interface between carrier and donor, which locally separates the donor material from the carrier and surrounding donor material. Hence, the desired donor material is transferred and released onto a target substrate, enabling a contact-free metallization process. As generated pressure does not operate directionally towards the substrate, the laser pattern is generally broader than the released donor material, exhibiting debris due to the splashing effect. Debris is donor particles that are not connected to the main body and are scattered around the printed donor material on the substrate. The debris could contribute to the total shading of a solar cell since it covers the active cell area.

Morales *et al.* presented a finger width between 90 and 150 µm and height of 50 µm with the LIFT method, which coated a commercial Ag paste on transparent glass using a squeegee and deposited it with a laser, resulting in variation of aspect ratio from 0.36 to 0.61 for front grids on a c-Si cell with a size of 10 × 10 cm [63]. Compared with the LIFT method, LTP technology uses a four-axis guided roll system to coat the transparent belt continuously with Ag paste [68], [69]. A substrate is placed underneath with some distance, and a laser pulse is used to transfer the Ag paste fabricating a finger width below 100 µm with a decent aspect ratio [67]. PTP technology utilizes pre-embossed grooves (trenches) as a mold on transparent polymer film to construct a particular shape of Ag paste. By inserting the Ag paste into the trenches, the shape of the metalized fingers can be improved resulting in a higher aspect ratio, and the splashing effect can also be minimized leading to a lower amount of debris than LIFT and LTP methods. As PTP is the main topic in this thesis, a more detailed explanation of PTP technology is described separately (see section 2.3). The recent results of PTP technology are also presented in chapter 5.

2.3 Pattern Transfer Printing Technology

Pattern Transfer Printing (PTP) technology was patented in 2015 [73] and has been developed since 2015 by the company Utilight Ltd. (currently called DR Utilight Corp Ltd.) in Yavne, Israel. PTP technology is a contactless metallization process using a laser, which could help to reduce wafer breakage during the printing process. The PTP printing sequence involves two processes: filling and transfer (see Figure 2.5). A transparent polymer carrier film with pre-embossed grooves or trenches[1] is rolled to the filling position, where two metal squeegee blades fill the paste into the trenches. These are narrow, long openings (like channels) in the transparent carrier film, which act as a mold for Ag paste. After the trenches on the film are completely filled with the paste, the film is rotated 180° and moved to the printing position. At the same time, the two squeegees and the next empty segment of trenches are pulled to the original filling position, preparing for the following transfer process for the next substrate.

A cell precursor as a substrate is held in place on a vacuum chuck, then positioned underneath the film at a short distance. An infrared laser irradiates the trenches one after the others. The laser irradiance is transmitted through the transparent polymer film, and its energy is absorbed first by the paste surface in the interface region between the paste and film material. The resulting heat energy vaporizes the solvent of the paste in the interface region and forms a high-pressure vapor layer at this paste-film interface. When sufficient pressure is built up at the paste-film interface, the paste is released onto the substrate surface. One segment consists of 1008 trenches and can be used to metalize nine cells with 112 fingers or eight cells with 126 fingers.

---

[1] For consistency with previous publications, instead of grooves the term “trenches” will be used in this thesis to describe the narrow, long opening in the polymer film for PTP technology.

Figure 2.6 shows four different trench geometries available for PTP technology. Various trench geometries determine the shape of deposited fingers, the paste laydown and the finger cross-sectional area. To fabricate this microstructure on the surface of polymer films, a rigid metal model is constructed with the desired trench design. This model is used for embossing the pattern into a polymer film. For this, the polymer film is heated to become deformable and the metal model is stamped with high pressure into the film.

The PTP machine uses a quasi-continuous wave ytterbium fiber YLM-QCW (IPG Laser GmbH, Burbach, Germany) to generate an infrared laser at a wavelength of 1070 nm with a repetition rate of 10 kHz and it has a laser scanning velocity of 250 $m \cdot s^{-1}$. It allows the paste deposition of 112 finger lines of 155 mm length for a cell area of 244.32 cm^2 at virtually the same time (in a few milliseconds). Including additional handling and transport time, the total printing time required for PTP process using a pilot machine 1800i at the International Solar Energy Research Center (ISC) Konstanz is 1.2 s per cell. However, the total printing time in the mass production might be even lower. The applied laser power of a PTP machine is adjustable between 250 and 700 W. Similar to the screen-printing technology, printing parameters of PTP, such as squeegee speed, squeegee pressure, laser power and distance between film and substrate, are optimized before the printing of cell precursors to achieve an optimal finger shape with the best aspect ratio. In a study conducted in 2015 by Lossen *et al*., it was shown that PTP technology had an advantage over the screen-printing technology and was able to produce homogeneous fingers with an average width of 27 µm and maintain a good aspect ratio [15].

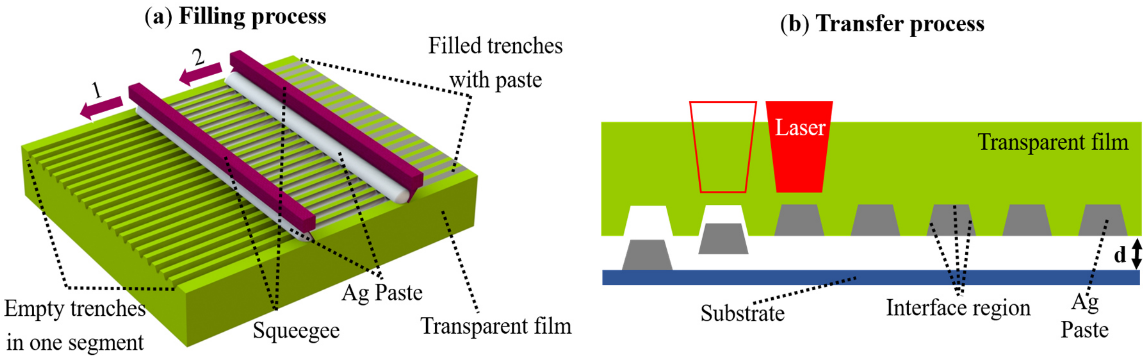
(a) Filling process
Filled trenches with paste
2
1
Empty trenches in one segment
Squeegee
Ag Paste
Transparent film
(b) Transfer process
Laser
Transparent film
d
Substrate
Interface region
Ag Paste

Figure 2.5: Illustration of PTP printing sequence for front finger metallization of c-Si solar cells [74]: (a) the filling process and (b) the transfer process.

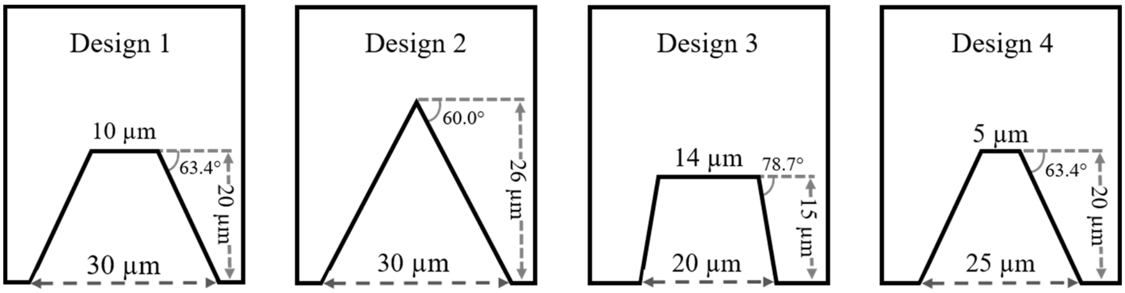
Design 1
10 µm
63.4°
20 µm
30 µm
Design 2
60.0°
26 µm
30 µm
Design 3
14 µm
78.7°
15 µm
20 µm
Design 4
5 µm
63.4°
20 µm
25 µm

Figure 2.6: Cross-sectional view of four various trench designs with different geometries available for PTP technology [72].

2.4 Rheological properties of thick-film-Ag paste

In this section, the main components of thick-film Ag paste are listed and described. Furthermore, the typical rheological properties of Ag paste for the front metallization using screen-printing as well as PTP technology are discussed. The rheological properties significantly influence the paste transfer for both technologies and the printability of fine Ag fingers of the desired shape. Printability is assessed by the finger homogeneity and its shape, interruption of Ag fingers, as well as paste splashing or spreading after the printing process.

2.4.1 Thick film Ag paste for the front metallization of c-Si solar cells

To extract the light-generated current from solar cells, metal contacts on the front and rear are required. Ag is chosen as the main component to extract the current on the front side because Ag is stable against corrosion in open-air conditions, has the highest electrical conductivity among all metals, and exhibits a low contact resistivity [49]. This advantage of Ag material properties allows for the deposition of narrow fingers for low optical losses and simultaneously limits the electrical losses. An industrial standard Ag paste contains a combination of Ag powder and inorganic glass frit suspended in a solvent-based organic vehicle [75], [76]. The organic vehicle is a mixture of polymers in organic solvent and other additives might be added as necessary.

Ag powder is typically spherical or flaky in shape, with a size ranging from one to five µm. The physical properties of Ag electrodes/fingers can be affected by the amount, particle size, surface area and shape of Ag powder. Data from several studies suggest that the particle size and surface area [77], as well as the ratio of Ag in the paste [75], actually impact the electrical conductivity of Ag fingers.

Glass frits act as an etching agent to remove the SiNx layer during the sintering steps and to moderate the formation of ohmic contacts between Ag and emitter. The amount, shape, size and composition of glass frits influence the etching step and affect the quality of the contact formation. The existing industrial Ag pastes use the PbO-based glass frits in the mixture, typically lead-borosilicate glass. However, another type of glass frits, namely bismuth-borosilicate glass, serves as an alternative to fabricate lead-free solar cells. Environmental regulations, such as the European Union REACH directive, request that electronic and electrical products become lead-free, in order to reduce the environmental impact and health risks of the products. However, solar modules are so far still exempted from REACH.

Organic solvent is required to dissolve the additives and reconstitute the Ag powder and glass frits from solid into the paste form. The organic solvent and organic additives combine to form the organic vehicle, which determines the rheological properties of Ag paste in order to improve the printability of Ag fingers. In the next section, several rheological properties of Ag paste are described.

Polymer binder, usually comprised of cellulose derivatives, is a crucial component that adds cohesion force between Ag paste and the wafer surface as a substrate, ensuring a successful paste deposition. It also influences the rheological properties of the Ag paste, and defines the green strength of the paste after drying.

Additives are added to adjust the rheological properties of Ag paste to warrant a good printability and improve the paste stability during printing. Thickener, stabilizer, thixotropic agents, or surfactants are various additives that may be found in the standard industrial screen-printing Ag pastes. Thickener is used to increase the viscosity of the paste and alleviate the squeegee step for the paste passing through the screen aperture. Stabilizer is added to improve the stability of paste against sedimentation of solid particles. Thixotropic agents are required to reduce viscosity during printing while maintaining a high viscosity after shearing, allowing the fingers to form a three-dimensional (3-D) structure and retain their shape after printing [78], [79]. Surfactants support dispersion of solid particles in the paste and improve the paste stability of the suspension through time [80]. It is essential to mention that the Ag pastes optimized for screen-printing and for PTP technology might have different additive compositions resulting from the paste adjustment for a successful paste transfer for each technology.

2.4.2 Typical rheological properties of thick-film Ag paste

The rheological properties of Ag pastes depend on the components in Ag pastes, mainly controlled by the composition of organic vehicles. Here, the various rheological properties of Ag paste that may affect the paste transfer for screen-printing and PTP technology are presented and discussed, such as yield stress, thixotropic behavior, viscosity and wetting properties of Ag paste.

Yield stress is defined as the minimum shear stress that must be applied to induce the transition from elastic solid-like behavior to viscous liquid-like behavior [81]. A certain amount of shear stress is generated during the squeegee stroke for both technologies and transferred to the thick-film Ag paste in front of the squeegee blade. The amount of stress applied to the Ag paste is controlled by adjusting the printing parameters, such as squeegee angle, printing speed and squeegee pressure. For shear stress above the yield stress, the Ag paste transitions from the solid-like to the liquid-like structure enabling a good paste flow into the structures of polymer film. However, a certain threshold of yield stress is required to achieve a high finger aspect ratio [30], [82]–[85] and to delay the sedimentation of solid particles in Ag paste, extending the paste shelf lifetime further [82]. However, too high yield stress of Ag paste might be detrimental for the paste transfer of screen-printing application resulting in inhomogeneity and line interruption as well as a reduction of screen lifetime due to the application of high shear stress. The effect of paste yield stress on the laser transfer process of PTP is presented and discussed in chapter 4.

Viscosity is the physical parameter that represents the flow resistance of a fluid related to the internal frictional forces during shearing [86]. A fluid with a constant viscosity independent of shear rate and a direct relaxation of the shear stress for a condition without shearing is called Newtonian fluid, for example, water, glycerin, etc. [87]. Apart from Newtonian fluids, the viscosity of other fluids may decrease or increase with increasing shear rate. The viscosity of Ag pastes sinks with increasing shear rate, indicating non-Newtonian fluid characteristics with shear thinning behavior, also called thixotropy. Viscosity plays a decisive role for a proper paste transfer of screen-printing technology, enabling the paste to easily flow through the screen mesh and aperture [84], [88]–[90]. Ag paste with low viscosity offers an easy printing process for a small screen aperture but results in a poor finger aspect ratio. Utilizing a high-speed camera underneath a transparent glass substrate to analyze the paste transfer of a flatbed screen-printing technology, Xu *et al*. [82] and Abdel Aal *et al*. [91] observed that the paste spreading is more distinct at high shear rates for Ag paste with a lower viscosity. The influence of paste viscosity on the PTP processes is investigated in chapter 4.

Thixotropic behavior is a time-dependent flow behavior of a fluid becoming thinner due to a decrease in the fluid viscosity while shearing (shear thinning behavior), and after a relaxation period with no shearing, the fluid gradually recovers and regains the initial state in short periods of time [92], [93]. The thixotropic behavior of Ag paste is critical for a successful printing process in both technologies. The shear stress applied in the paste during the squeegee stroke changes the paste structure into liquid-like and reduces the paste viscosity, which facilitates the paste to flow into the trench during the filling process of PTP or through the screen aperture and mesh onto the substrate during the squeegee process of screen-printing application. The thixotropy property of Ag paste facilitates the paste to regain its initial structure (more viscous and solid-like) after the squeegee process during the screen-printing process, and the structural recovery process takes place within milliseconds according to the experimental observations carried out by Xu *et al*. [82] and Abdel Aal *et al*. [91]. Hence, the thixotropic behavior determines if spreading occurs or the thick-film Ag paste can maintain its form until drying, resulting in a bad or a good finger aspect ratio, respectively. Several studies about the influence of thixotropy behavior of Ag paste for screen-printing application showed that the narrower fingers could be achieved if the Ag paste has a higher storage modulus (elastic properties) [90] and the recovery time for the paste to regain its initial structure is lower [88].

Wettability defines an ability of a liquid to preserve its contact with a solid surface related to the physicochemical properties of both liquid and solid [94]. For the front metallization, suitable wetting properties of thick-film Ag paste on a substrate must be reached by adjusting its organic vehicle to achieve adhesion between Ag paste and a solar cell surface and thus the printability. A good adhesion ensures that Ag pastes stick to the substrate during and after the squeegee stroke and that the paste is released from the screen during the snap-off step. Liang *et al*. observed that the surface energy of the solid influences the wettability of paste significantly and therefore affects the line resolution in the screen-printing application [95]. A less wettable screen emulsion through coating enhances the paste transfer during the snap-off step of the screen-printing application, as observed by Tepner *et al*. [96]. They showed that the coated screen surface with lower wetting properties resulted in more homogeneous fingers with a smaller width due to a better wall slip, enabling the paste to flow through the screen aperture easily [96]. The solid-liquid interaction related to the wetting behavior between Ag pastes and the surface of polymer film for PTP application is investigated in chapter 4.

2.5 Front contact formation

To complete the metallization step of c-Si solar cells, the sintering process is required after the paste deposition on both surfaces, creating an Ag contact formation on the front and Al contact formation on the rear, for the case of PERC technology. This section focuses on the contact formation of Ag on the front side of PERC solar cells. The following features should be achieved with screen-printed front contacts: high aspect ratio, firing through SiN_x, low contact resistance, high conductivity, no junction shunting, good adhesion to silicon and good solderability for cell interconnection [97]. Figure 2.7 illustrates a typical firing profile of a fast-firing furnace used in mass production and three characteristic phases during the Ag front contact formation are marked. The first phase is the burn-out phase, where the organic vehicles inside Ag paste are removed, leaving only Ag and glass frit. Yüce *et al*. found out that the organic vehicles are not removed entirely after sintering steps but that residuals can be found in the Ag fingers, resulting in a higher lateral finger resistance due to impurities [71].

A further increase in temperature of Ag paste initiates a melting process of the glass frit and a redox reaction between glass frit and Si. The liquid glass etches SiN_x and also dissolves Ag and Si. Inverted pyramid pits are created on the Si wafer surface resulting from the redox reaction and filled with Ag. The amount of glass frit inside Ag paste must be controlled to prevent too deep etching of silicon, leading to Ag-spikes reaching into the *p-n* junction and producing junction shunting and space charge region recombination. Furthermore, a thin glass layer forms between the conducting Ag thick-film and the emitter affecting the contact resistance of the screen-printed Ag front contact. In the cooling phase (III), the temperature is reduced significantly and Ag recrystallizes in the inverted pyramidal pits forming the Ag crystallites at the Si-glass-Ag interface. The Ag crystallites act as ohmic contacts to the Si, and the current transport on the front surface is conducted through these Ag crystallites, colloidal Ag precipitates and the ultra-thin interfacial glass layer [97]. Detailed models of Ag front contact formation are studied and reviewed by Schubert *et al*. [98] and Hong *et al*. [99].

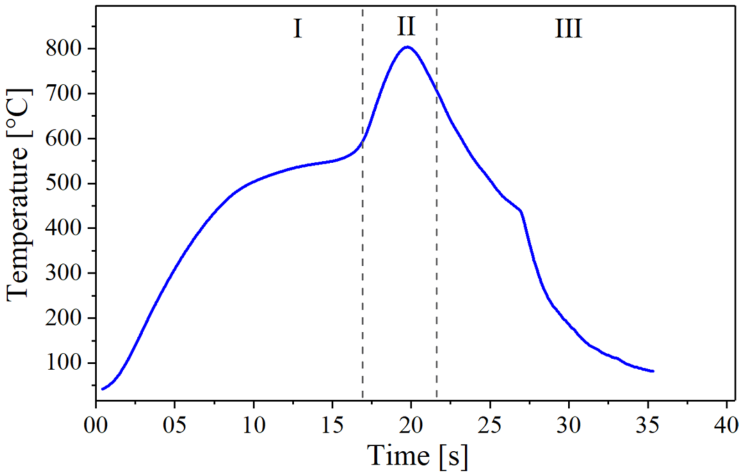

Figure 2.7: Illustration of a typical firing profile used for sintering step in a fast-firing furnace consisting of three phases of contact formation: phase I is the burn-out phase, phase II represents the SiN_x etching phase and contact formation, and phase III is the cooling phase.

2.6 Characterization methods

This section focuses on the state-of-the-art methods to characterize the parameters of solar cells and the rheological properties of Ag pastes that were used in this thesis.

2.6.1 Solar cell

Here, the state-of-the-art characterization methods for solar cells are discussed, such as, *I-V* measurement, surface metrology, external quantum efficiency measurement, contact resistivity measurement, line resistance measurement, luminescence imaging analysis, and the electrochemical capacitance-voltage method.

2.6.1.1 *I-V* measurement

An *I-V* curve contains all important information about the operation characteristics of a solar cell. Normally, it is determined in the lab using a flash-type solar simulator, which illuminates the solar cell surface homogenously using an artificial light source with a similar spectrum as sunlight and a tunable power source or a cascade of resistance. From the *I-V* curve (see Figure 2.8), several electrical parameters of a solar cell can be determined, such as open-circuit voltage (V_{oc}), short-circuit current (I_{sc}) or short-circuit current density (J_{sc}), fill factor (*FF*), cell efficiency (η). The *I-V* curve depends on three external conditions: the light intensity, the spectrum of the incident light and the cell temperature. Therefore, the *I-V* measurement is conducted worldwide under normalized conditions, namely standard test conditions (STC), to deduce and limit these dependencies, enabling an accurate comparison of *I-V* results by different laboratories or industries.

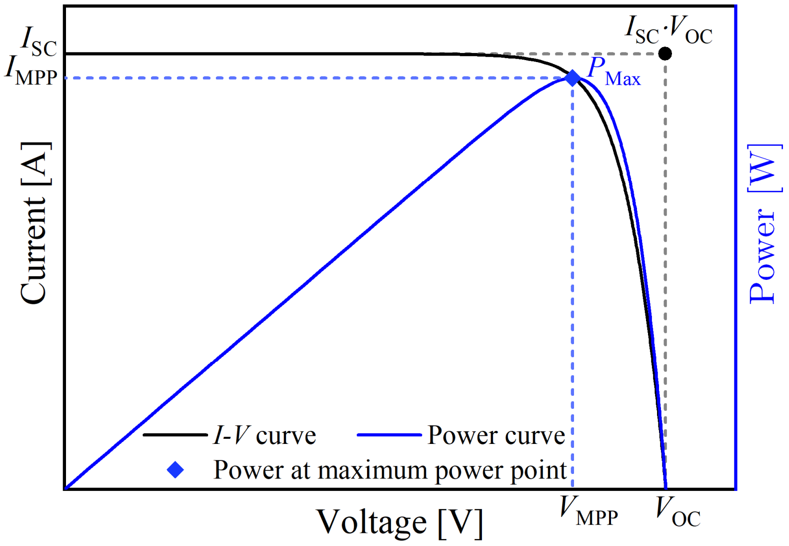

Figure 2.8: Illustration of a current-voltage *(I-V)* curve of a solar cell.

A flash-type solar simulator is required to generate homogeneous light of 1000 W·m^{-2} over the cell area and a similar spectrum as sunlight at AM1.5(g). Furthermore, the cell temperature during the measurement needs to be controlled at close to 25 °C. These three conditions are defined as the standard test conditions (STC). The effect of temperature deviance must be compensated in the measurement results using a correction factor, called temperature coefficient. The *I-V* measurement in this thesis were measured under STC using xenon flash-type solar simulator cetisPV by h.a.l.m electronik GmbH, Frankfurt am Main, Germany, which spectrum is rated to be in high agreement with sunlight, class AAA. Further specification of this cetisPV sun simulator is listed in Table A1.

2.6.1.2 Surface metrology

The characterization of print geometry is essential to analyze expected shading and expected line conductivity of Ag fingers obtained by PTP technology, and compare it with the screen-printing reference. Two different characterization methods for the Ag fingers on the front surface are conducted in this thesis, namely confocal laser scanning microscopy and scanning electron microscopy.

Confocal laser scanning microscopy (CLSM) is frequently used to characterize the Ag printed geometries in this work. CLSM creates defined optical sections of the Ag finger using laser light in a confocal beam path. Ag finger on the front surface of solar cells is partitioned into several optical sections between the surface and the objective of the microscope (*z*-axis). A small opening, called pinhole, is positioned to block information outside the focus area and only information within the focus plane is processed. Laser scanning moves in the *x*- and *y*- direction, and the information inside the focus area is converted to a greyscale image of each optical section. All images between the surface and objective are combined, resulting in a 3-D image stack of Ag finger. The height of Ag finger is determined by assessing the intensity distribution of a single pixel across the entire image stack. Furthermore, a height map of Ag finger can be generated by integrating the height information from the entire image field. A detailed explanation of CLSM is presented by Paddock [100] and Claxton *et al.* [101]. A confocal laser scanning microscope LEXT OLS4000 LSM (Olympus K.K., Tokyo, Japan) was used to analyze the printed Ag contacts in this thesis. Finger width, finger height and finger cross-sectional area can be extracted from the 3-D images using an image analysis software Mountains Technology Surface Texture Analysis Premium [102].

Scanning electron microscopy (SEM) can also be used to analyze the Ag finger contact. One of its advantages is the capability of SEM to produce a high-quality cross-section image of Ag finger than CLSM. Hence, all cross-sectional images of Ag contacts in this thesis were taken using a scanning electron microscope JSM-6510 (JEOL Ltd., Tokyo, Japan) with the assistance of K. Tsuji from Toyo Aluminium K.K., Japan. The basic principle of SEM is discussed in detail by Reimer [103]. A high electron beam with energy up to 30 keV generated from a field-emission cathode scans the solar cell surface in a raster pattern within a vacuum-sealed chamber. Several electromagnetic and electrostatic lenses are used to regulate the trajectory and shape of the electron beam. After the electron beam makes contact with atoms at various depths within the substrate, backscattered and secondary electrons are generated, providing information about the morphology of Ag finger, and absorbed by electron detectors. All information is delivered through a cathode-ray tube, forming a 3-D image of Ag finger. SEM provides a characterization method with a wide range of magnification simply by adjusting the scan-coil current [103].

2.6.1.3 External quantum efficiency measurement

External quantum efficiency (EQE) describes the ratio of the electrons generated by the solar cell to the number of incident photons on the solar cell. EQE values in this thesis were measured over a range of wavelengths inside the active bandgap of the solar cell using IQE-SCAN (pv-tools GmbH, Waldburg, Germany) [104]. The solar cell is mounted on a temperature-controlled vacuum chuck of 25 °C. A combination of chopped monochromatic light from 280 to 1200 nm from a grating monochromator and white bias light of one sun illuminates the solar cell homogeneously over an area of 20 mm × 20 mm. A lock-in amplifier is set to detect the low-level modulated current from the solar cell, and about 200 lock-in readouts are recorded per wavelength and averaged to provide a single value per wavelength [104]. The specification of IQE-SCAN is listed in Table A2. The J_{sc} value from the *I-V* measurement of the respective solar cell is used to validate the EQE measurement result based on the following equation [105]:

$$J_{\mathrm{sc}} = \frac{q}{c \cdot h} \int EQE(\lambda) \cdot \lambda \cdot E(\lambda)\, d\lambda \tag{2.1}$$

where q is the elementary charge of $1.6022 \cdot 10^{-19}$ A·s, c is the light speed of $2.9979 \cdot 10^{8}$ m·s^{-1}, h is the Planck´s constant of $6.6261 \cdot 10^{-34}$ W·s^{2}, λ is the wavelength, and E is the spectral irradiance.

2.6.1.4 Contact resistivity measurement using transfer length method

Contact resistivity of Ag finger to emitter is a vital parameter to characterize the quality of the front metallization of solar cells. For comparison with another contact with various sizes, contact resistivity has to be chosen since it is independent of contact area compared to contact resistance. It contributes to a power loss due to series resistance and may result in a lower *FF*, leading to higher power loss in case of bad ohmic contact. The standard method to determine the specific contact resistance between Ag finger and Si is the transfer length method (TLM) [106], which is suitable for measuring contact resistivity values to a minimum of $1 \cdot 10^{-6}$ Ω·cm^{2} [107].

Figure 2.9(a) illustrates the schematic of the test structure using TLM to measure contact resistivity of the front metallization of silicon solar cells, where the solar cell samples are cut into small stripes with a width of 10 mm, forming a ladder structure for TLM. Each Ag finger is contacted with two pins for measuring the resistance from one Ag finger to another. The first pin is used for injecting/extracting a current and the second pin for measuring the voltage drop between the fingers. Every voltage drop due to a total resistance between each pair of adjacent Ag contacts R_{total} is measured. The total resistances between possible all pairs of six Ag fingers are plotted as a function of Ag contact distance d_{c}, creating a TLM graph as shown in Figure 2.9(b). The parameters, such as sheet resistance under the finger R_{Emitter}, contact resistance R_{C}, transfer length L_{T} and contact resistivity ρ_{C}, can be calculated from the graph, using the following equations under the assumption that the emitter sheet resistance under the Ag contact and between Ag contacts is identical [106]:

$$R_{\text{total,between two Ag contacts}} = \frac{R_{\mathrm{Emitter}}}{Z} \cdot d_{\mathrm{c}} + 2 \cdot R_{\mathrm{C}} \approx \frac{R_{\mathrm{Emitter}}}{Z} \cdot (d_{\mathrm{c}} + 2 \cdot L_{\mathrm{T}}) \tag{2.2}$$

$$R_{\mathrm{C}} = \sqrt{\frac{\rho_{\mathrm{C}} \cdot R_{\mathrm{Emitter}}}{Z}} \cdot \coth\left(\sqrt{\frac{R_{\mathrm{Emitter}}}{\rho_{\mathrm{C}}}} \cdot L\right) \tag{2.3}$$

$$L_T = \sqrt{\frac{\rho_C}{R_{\mathrm{Emitter}}}} \tag{2.4}$$

where, Z is the length of the contact finger and L is the width of contact finger. The slope is equivalent to the emitter sheet resistance R_{Emitter}, and the contact resistance R_C can be measured using the extrapolation of the measurement data at the y-axis intercept ($d = 0$) that corresponds to the value $2 \cdot R_C$. Contact resistivity ρ_C is determined using Newton´s method in 20 iteration steps using equation 2.3. The transfer length L_T is the length where the voltage drops exponentially to $1/e$ of its value and is also described as the distance that current flows in the semiconductor through the finger contact area. A study regarding the influence of contact distance, width of strips, the shunting effect and the difference between emitter sheet resistance under the Ag contact and between Ag contacts on the contact resistivity of front metallization contact of silicon solar cells is presented by Guo *et al.* [108]. In this thesis, the contact resistivity measurement was conducted using a GP 4-Test Pro (GP Solar, Konstanz, Germany).

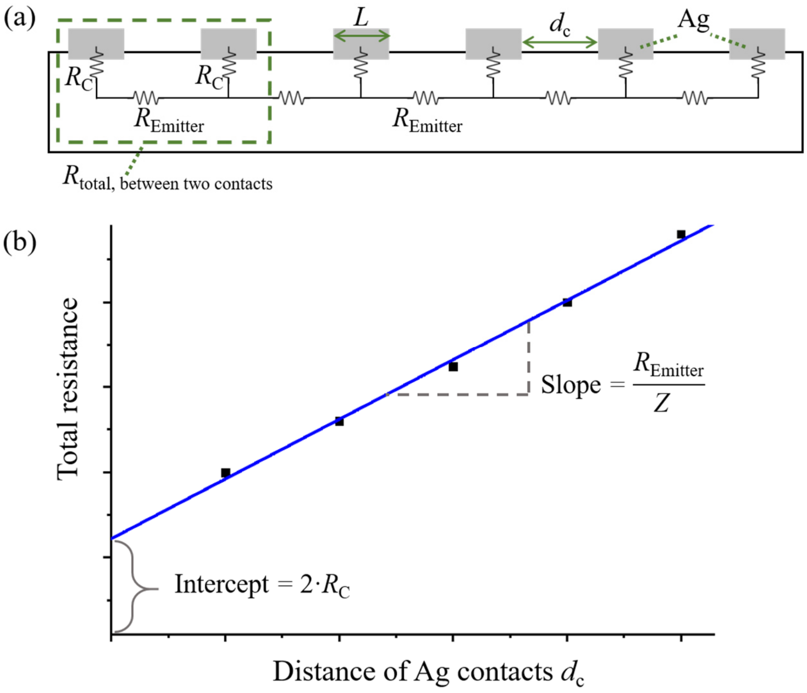
(a)
L
d_c
Ag
R_C
R_C
R_{Emitter}
R_{Emitter}
$R_{\mathrm{total, between\ two\ contacts}}$
(b)
Total resistance
Slope = $\frac{R_{\mathrm{Emitter}}}{Z}$
Intercept = $2 \cdot R_C$
Distance of Ag contacts d_c

Figure 2.9: Transfer length method for characterization of ohmic contact between Ag contact and Si: (a) illustration of ladder structure for TLM measurement, (b) TLM plot of total resistance as a function of contact distance for determination of sheet resistance, contact resistance, transfer length and contact resistivity of Ag fingers.

2.6.1.5 Finger line resistance via four-point-contact measurement

The lateral finger line resistance can be determined using four-point-contact measurement method [109]. As it is called, this measurement method uses in total four pins, two each for current and voltage. Current is injected through the two outer pins, and two inside pins are used to measure the voltage drop due to lateral resistivity of Ag fingers utilizing a multimeter. The lateral finger resistance can be defined as a ratio between the voltage drop and the injected current [106]. A certain distance between these pairs of pins must be fixed to achieve a consistent measurement value for each measurement. The lateral finger resistance values in this thesis were measured using a customized four-point-contact measurement setup for Ag fingers with a distance of 22 mm.

2.6.1.6 Luminescence imaging

Luminescence imaging is a standard method to characterize solar cells. Semiconductors (e.g. solar cells), can be used as a light-emitting diode by injecting free charge carriers into a solar cell [110]. Radiative recombination converts the free charge carriers into photon energy, and an image of emitted photons is captured using a susceptible camera, delivering information about the properties of the solar cell.

Photoluminescence (PL) utilizes photon energy from a diode laser with an overlapping diffuse beam to inject free charge carriers into a solar cell [111]. The photon energy is absorbed and re-emitted at a longer wavelength as radiative energy by the solar cell. The photoluminescence radiation is detected by a near-infrared camera and is converted into a greyscale image. A different PL intensity across the solar cell shows the characteristics of solar cells or even non-metalized cells, such as minority carrier lifetime, surface recombination, inhomogeneity, and possible defect area [112]. PL images in this thesis were taken under open-circuit conditions using a customized PL measurement setup with a silicon charge-coupled device (Si-CCD) camera PIXIS 1024BR (Teledyne Princenton Instruments, USA).

Electroluminescence (EL) uses an electrical source to inject free charge carriers into solar cells by contacting the front busbars and rear side with metal contacts connected to a power supply. The electrical energy injected into the solar cell creates free charge carriers, which re-emitted photons via radiative recombination. This luminescence emission is detected using a shortwave infrared camera, and it is converted into a greyscale image delivering information about the quality of contact formation, finger interruption and micro-cracks in the solar cell [113]. In this thesis, EL images were taken under a forward bias condition using a LumiSolarCell (greateyes GmbH, Berlin, Germany), and its specification is listed in Table A3.

2.6.1.7 Electrochemical capacitance-voltage

The electrochemical capacitance-voltage (ECV) method is used to characterize doping profiles in a Si wafer [114]. In this thesis, the doping profiles of the diffused *n*-type layer were determined with the ECV method using a Wafer Profiler CVP21 (WEP, Furtwangen, Germany). The sample is placed in the measuring chamber, where a spot size with a diameter around four millimeters is sealed with a sealing ring enabling direct contact between Si and an electrolyte solution. This contact creates a Schottky-barrier at the interface between Si and electrolyte, allowing electron current to pass through. A silver chloride electrode is placed near the Si wafer to determine the electron current and the potential difference during the measurement. The doping profile of carrier concentration versus depth profile is determined through a depth-dependent capacitance-voltage measurement by creating a depletion region at the Si-electrolyte interface and controlled etching of the Si wafer. The capacitance of the space-charge region of the *n*-layer is quantified at a fixed bias voltage. A specific amount of Si is removed in the nanometer range by varying the current applied to an electrolyte solution of ammonium bifluoride with a concentration of 100 mol·m^{-3}. A full description regarding the ECV measurement method is discussed in [115], [116].

2.6.2 Paste rheological properties

Typical rheological parameters of Ag paste are described before in section 2.4. Here, the state-of-the-art characterization method for each parameter is explained and discussed.

2.6.2.1 Yield stress measurement

In this thesis, yield stress of various Ag pastes was measured using a rotational rheometer Rheostress 150 (Thermo Fisher Scientific, Karlsruhe, Germany) equipped with a vane geometry. The yield stress measurement is based on a protocol established by Yüce and Willenbacher [117]. Ten milliliters Ag paste is filled into a cylindrical measuring cup. The holder of the measuring cup is temperature-controlled, enabling the measurement at various temperatures. The vane geometry is inserted into the measuring cup and set at the height for the measuring position. After a five-minute stabilization period, controlled shear stress is applied and stepwise increased from 1 – 3000 Pa. The so-called apparent yield stress for each Ag paste was determined from the kink in the logarithmic plot of deformation γ versus shear stress using the tangent intersection method [117], as illustratively shown in Figure 2.10.

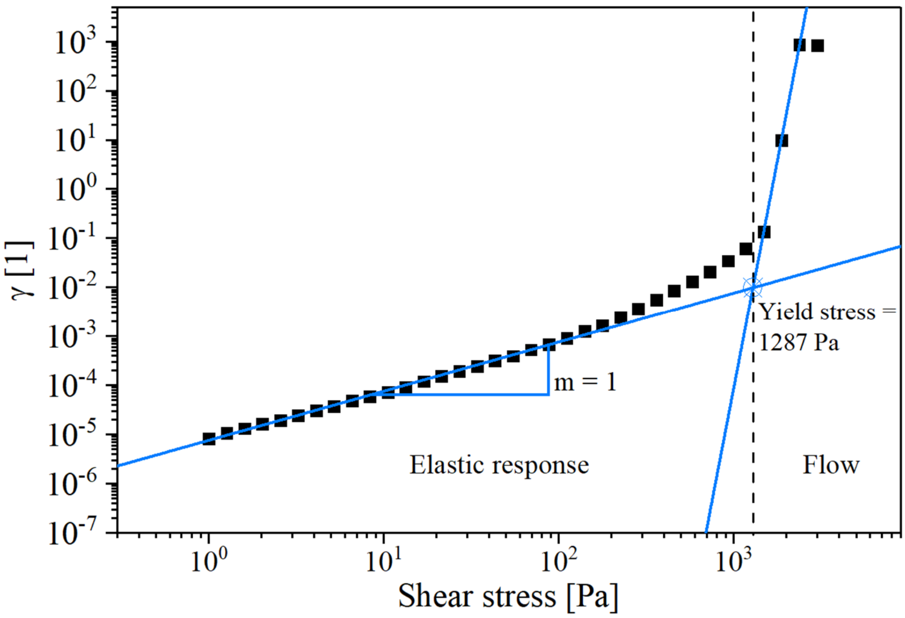

Figure 2.10: Illustration of yield stress determination using the tangent intersection method from the logarithmic plot of deformation γ versus shear stress.

2.6.2.2 Viscosity

The viscosity values presented in this thesis were measured by the paste supplier using a viscometer and a cone plate spindle CPE-51 (Brookfield Engineering Laboratories, Inc., Middleboro, MA, USA) at one rpm and 25°C for five minutes. As the printing process of screen-printing and

PTP technology uses a fast squeegee speed, the shear stress applied to the Ag paste in front of the squeegee is higher than the applied shear stress at one rpm using a parallel-plate rotational rheometer. As mentioned before in section 2.4, the viscosity of Ag paste decreases with increasing shear stress. Therefore, the actual viscosity of Ag paste is lower than the viscosity value provided by the paste supplier. The viscosity measurement at high shear stress using a parallel-plate rotational rheometer might detect wall slip phenomena that cause a false determination of Ag paste viscosity value [117]. The particle layer near the wall of the plate is more diluted than in the bulk flow and has a significantly lower viscosity, causing slippage of bulk liquid along the wall.

A capillary rheometer can also be used to characterize the viscosity of Ag paste at a higher shear rate, which represents the real pressure applied to the paste during the printing process. A rheological characterization for Ag paste at high shear rates with a capillary rheometer is presented by Yüce and Willenbacher [117]. A nozzle with a diameter of 0.5 mm and a length of 40 mm is selected and installed into the capillary rheometer together with a 500 bar pressure transducer. A homogeneously mixed Ag paste is filled into the feed reservoir and pressed with the piston through the nozzle. The measurement is conducted in stepwise controlled shear rate by applying various piston velocities between 0.001 and 20 $\mathrm{mm \cdot s^{-1}}$. Minimum five pressure data points are required for each piston velocity. The apparent shear rate is determined from the volumetric flow rate using the piston velocity and diameter of the feed reservoir and corrected for non-Newtonian liquid with the Weissenberg-Rabinowitsch equation to gain the true shear rate [118]. The wall shear stress is calculated from the pressure gradient, which is the pressure drop per unit length of the nozzle. Finally, the apparent viscosity is determined as the ratio between the wall shear stress and the shear rate.

2.6.2.3 Tensiometry

The organic vehicle of Ag pastes determines the wetting properties of the polymer film for PTP application. A standard method to characterize the wetting properties of a liquid on a solid material is tensiometry [119]. To characterize the wetting properties of Ag paste on the polymer film, the three-phase contact angle of the organic vehicle on the polymer film was determined using a customized sessile drop tensiometer. First, a centrifugation step at 9000 rpm for 30 min is conducted to separate the liquid and solid phase in Ag paste. Polymer films were cut each to a size of 3 cm × 7 cm and glued to a microscope slide. The extracted organic vehicle was squeezed from a needle with a diameter of 0.8 mm onto the polymer film. The droplet shape was recorded using a camera Stingray F-033 (Allied Vision Technologies GmbH, Stadtroda, Germany), and the contact angle value was obtained via the image analysis program ImageJ [120].

2.6.2.4 Differential scanning calorimetry

Laser irradiation of PTP technology evaporates the organic vehicle of Ag paste at the paste-film interface. Differential scanning calorimetry (DSC) is a standard method for characterizing the thermal properties of materials [121] and was used in this thesis to determine the boiling point of the organic vehicle of Ag paste. The main principle of DSC is that the heat from a furnace flows symmetrically to the samples through a disk of medium thermal conductivity integrated with temperature sensors, where the differential temperature signal ΔT between the reference crucible and the crucible with samples are measured [122]. This ΔT is converted into the heat flow rate as a measurement output calculated internally with the software. In this thesis, a DSC 214 Polyma (Netzsch-Gerätebau GmbH, Selb, Germany) is used to study the thermal behavior of various Ag pastes by analyzing heat flow as a function of temperature.

3 Development of Pattern Transfer Printing Technology

PTP technology emerged in 2015 as a new alternative technology for the front surface metallization of c-Si solar cells [15]. *As a recently emerging technology, PTP requires steady development and optimization to obtain its full potential. Similar to screen-printing technology, the printing sequence of Pattern Transfer Printing (PTP) technology consists of two steps: the filling process and the transfer process. In this chapter*[1]*, the development and optimization of each printing step of PTP technology are described. The printing parameters of PTP technology are investigated to improve the print quality of the front metallization of c-Si solar cells. The effect of the squeegee blade angle on the filling process of thick-film silver paste is evaluated. The influence of laser power on the transfer process of PTP technology is investigated, and its impact on the finger profile is also analyzed. The effect of laser power on preventing line interruption is also examined since line interruption is a critical aspect in the PV industry. In addition, the term "laser power threshold" for the PTP laser transfer process is defined to describe the laser power required to ensure a successful paste transfer. Finally, the quality of solar cells after the laser process of PTP is investigated to look into possible laser-induced damage.*

3.1 Impact of squeegee configuration for the filling process

PTP technology utilizes transparent polymer film with pre-embossed trenches on its surface. There are two main objectives in the filling process of PTP. Not only thick-film Ag paste must be filled completely into the trenches using a squeegee blade, but also the surface of the trench surface must clean from any paste residue. A pre-experimental result showed that one squeegee blade was insufficient to achieve these two objectives. A typical squeegee angle of 60° toward the film surface is chosen to apply sufficient hydro-dynamic pressure to thick-film Ag paste in front of the squeegee, as shown by Riemer [29], which helps to inject the paste into the trenches. However, a part of the paste is scooped away, creating a concave paste surface in the trenches and leaving the trenches half-filled with paste. Therefore, another squeegee blade is required to fill the paste into the trenches sufficiently and level the paste with the film surface. Hence, in this section two different configuration of squeegee blades are introduced, and the quality of the filling process of both configurations are investigated.

---

[1] This chapter 3 is partly adapted from the author´s publications:

A. Adrian, D. Rudolph, J. Lossen, and N. Willenbacher, "Investigation of Thick-Film-Paste Rheology and Film Material for Pattern Transfer Printing (PTP) Technology," Coatings, vol. 11, no. 1, p. 108, Jan. 2021, DOI: 10.3390/coatings11010108.

A. Adrian, D. Rudolph, N. Willenbacher and J. Lossen, "Finger Metallization Using Pattern Transfer Printing Technology for c-Si Solar Cell," IEEE Journal of Photovoltaics, vol. 10, no. 5, pp. 1290-1298, Sept. 2020, DOI: 10.1109/JPHOTOV.2020.3007001. © 2020 IEEE.

3.1.1 Experimental details

Two different squeegee configurations were investigated to improve the filling quality of PTP technology. Parts (a) and (b) of Figure 3.1 show two schematic angle configurations of the squeegee blades for the PTP filling process. The first configuration is called the fill and fill (F&F) configuration, where the second metal squeegee blade has the same blade angle as the first squeegee (60° toward the film surface). The second configuration is called the fill and clean (F&C) configuration, where a higher angle for the second squeegee than the first squeegee is chosen, and has a blade angle of 130° toward the film surface. The same thick-film paste was filled inside the trenches using these two angle configurations. To analyze the filling quality of these configurations, the surface of transparent polymer films directly after the filling process of PTP was observed using confocal laser scanning microscopy (CLSM).

3.1.2 Results and discussions

Figure 3.1(c) and (d) show 3-D images of the trench formed on the surface of a transparent film after the filling step of PTP using two different angle configurations. The F&F configuration was able to fill the trenches to a certain degree. However, the scooping effect was still observed, and it created inhomogeneous cavities in the trenches with depths between 3 and 9 µm. Such cavities in the trenches lead to an irregularity in the buried Ag shape and later an inhomogeneous cross-section of printed fingers, which causes an increase in finger resistance. With a blade angle of 130° for the second squeegee, the F&C configuration filled more paste into the trenches and more uniform along with the trench opening. However, unfilled trenches with depths between one and two µm were observed due to the scooping effect during the filling process. The scooping effect is caused by deflection of the squeegee blade within the trenches and excessive pressure from the squeegee blade on the buried paste in the trenches. Increasing the angle of the second squeegee reduces the pressure on the paste, and therefore, the scooping effect can be minimized by using F&C configuration in the filling process of PTP.

The printing parameters, such as squeegee pressure and speed, can be adjusted to reduce the pressure on the paste inside the trenches. Nevertheless, sufficient pressure is also necessary to ensure the cleanliness of the film after the filling process. Figure 3.2 shows the CLSM images of the film surface after the filling process using the F&C configuration with two different squeegee pressures. It was observed that inadequate pressure resulted in a bad swiping, leaving some paste residue on the surface of the transparent film. Increasing squeegee pressure to 3.5 bar is sufficient to wipe the film surface clean of any residual paste. The diameter spot of the top-hat laser beam of PTP is approximately around 100 µm. It is wide enough to illuminate the paste in the trenches and the residual paste on the film surface near the trenches, increasing the amount of debris on the substrate underneath unnecessarily. Therefore, paste residual on the surface needs to be eliminated because it will increase the amount of debris and reduce the cell efficiency due to higher shading. As the F&C configuration provides a uniform paste filling over the whole trenches and removes the unwanted paste residual from the film surface, the F&C configuration is chosen to be the standard configuration of the PTP filling process.

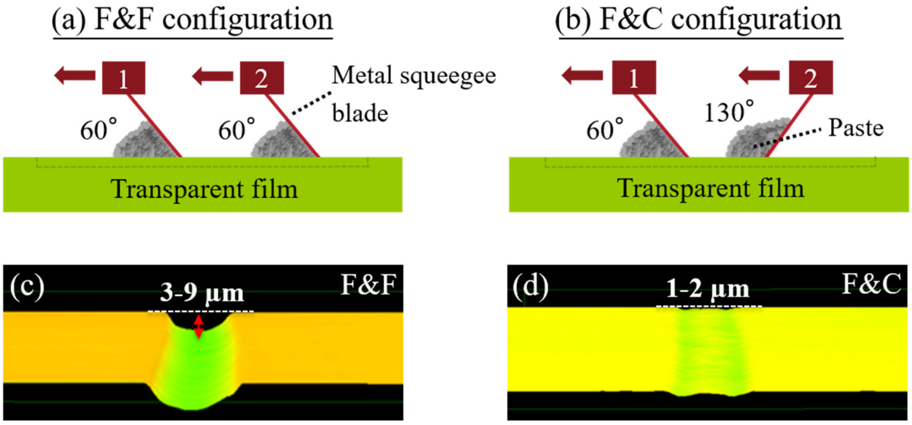
(a) F&F configuration
1
2
60°
60°
Metal squeegee blade
Transparent film
(b) F&C configuration
1
2
60°
130°
Paste
Transparent film
(c)
3-9 µm
F&F
(d)
1-2 µm
F&C

Figure 3.1: Two blade configurations for the filling process of PTP technology: (a) Fill and fill (F&F) configuration with a blade angle of 60° for both squeegees; (b) Fill and clean (F&C) configuration with an angle of 60° for the first squeegee and 130° for the second squeegee; sectional CLSM images of the surface of transparent film after the filling process of the F&F (c) and the F&C configuration (d).

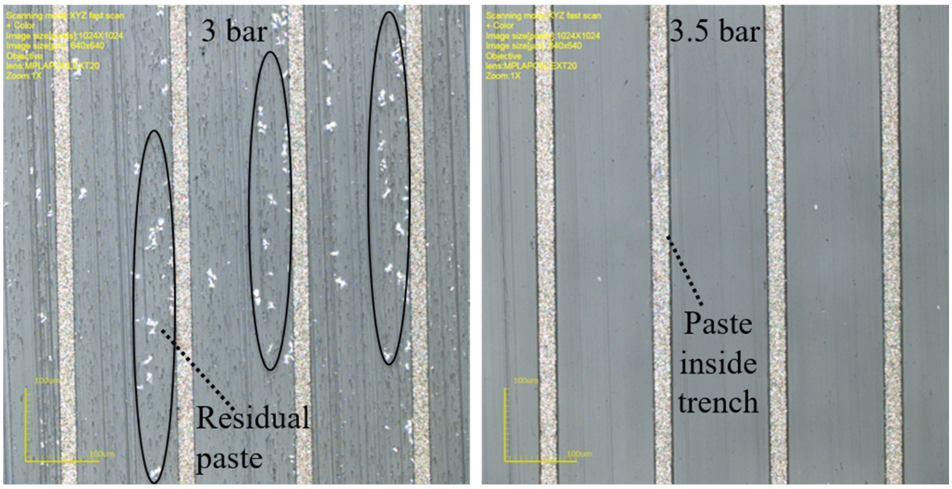
3 bar
Residual paste
3.5 bar
Paste inside trench

Figure 3.2: Comparison of the transparent film surface with different second squeegee pressures: applying a squeegee pressure of 3 bar is insufficient to clean the surface of the polymer film (left) and a squeegee pressure of 3.5 bar is required to remove the residual paste on the film surface completely (right). CLSM images were obtained at 20× magnification.

3.2 Influence of laser power on the print quality of PTP

An infrared laser is utilized to transfer thick-film Ag paste onto a substrate. The laser irradiance is absorbed by the paste surface and it causes a temperature increase in the paste surface at the paste-film interface sufficiently to evaporate the organic component of the paste, which leads to evaporation of organic components of Ag paste. The evaporation creates a high-pressure layer in the interface region, resulting in a successful paste transfer onto the substrate underneath. In this section, the influence of laser power for the laser transfer process on the print quality of PTP technology is investigated.

3.2.1 Experimental details

Ag fingers were deposited with different laser powers on textured monocrystalline silicon wafers coated with silicon nitride (SiN_x) as substrates. In this experiment, trapezoidal trench geometry with 25 µm trench width (trench design 4, see Figure 2.6) was used, and the same thick-film Ag paste was filled inside the trenches using F&C configuration. The operating laser power was increased in steps of 100 W from 250 to 650 W. After metallization steps using PTP, all samples were dried at 200 °C for 15 min duration using a Baccini paternoster drying oven and sintered using a fast-firing furnace c.FIRE at a peak temperature of 905 °C and a belt speed of 7 $m \cdot min^{-1}$. The finger morphology was imaged at 50× magnification using a CLSM Olympus LEXT OLS4000, and the images were analyzed using the surface analysis software Mountains Technology Surface Texture Analysis Premium [102] to determine the height and the width of printed fingers.

3.2.2 Results and discussions

Figure 3.3 shows CLSM images of the surface of the substrate printed using five different laser power from 250 to 650 W. The operating laser power at 250 W created insufficient high-pressure vapor to overcome the adhesive forces between the Ag paste and film material, resulting in no paste transfer. With increasing laser power, the paste transfer was started, and it occurred for laser powers from 350 to 650 W. The increase in laser power improved the straightness of the fingers, but simultaneously more substantial splashing effect was observed, creating more debris around the printed fingers. This stronger splashing can be understood by considering that the high-pressure vapor layer at the paste-film interface expands with the increasing laser power. The generated pressure was apparently enough to surpass the adhesive forces to release the paste and overcome the cohesive strength within the Ag paste.

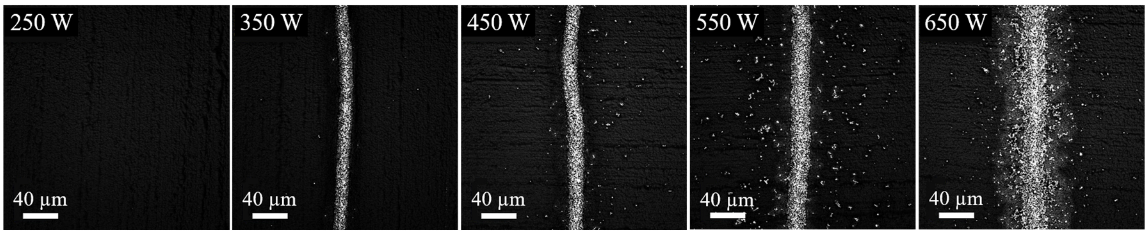

Figure 3.3: Top-view images of PTP-printed fingers with different laser power from 250 to 650 W. CLSM images were obtained at 50× magnification. © [2020] IEEE. Reprinted, with permission, from ref [72].

Figure 3.4 presents the finger width, finger height and the calculated finger aspect ratio for each laser power. Finger width increases and finger height decreases with increasing laser power. Therefore, the highest aspect ratio of 0.7 was achieved using a laser power of 350 W. Figure 3.3 and Figure 3.4 show that the laser power of 350 W offers the optimum laser transfer for the trench design 4, because the amount of debris or splashing were mitigated and the printed finger had the highest aspect ratio. Judging from the analysis of finger shape, lower shading and highest cell efficiency would be expected for the laser power of 350 W. Another criteria for a successful laser transfer of PTP technology is the completeness of the paste release over a substrate area, defined as the capability of laser power irradiation to release the paste from the whole trenches onto the substrate without any interruptions. Top-view images of PTP-printed fingers on the substrate surface using a laser power of 350 and 450 W, respectively, are depicted in Figure 3.5.

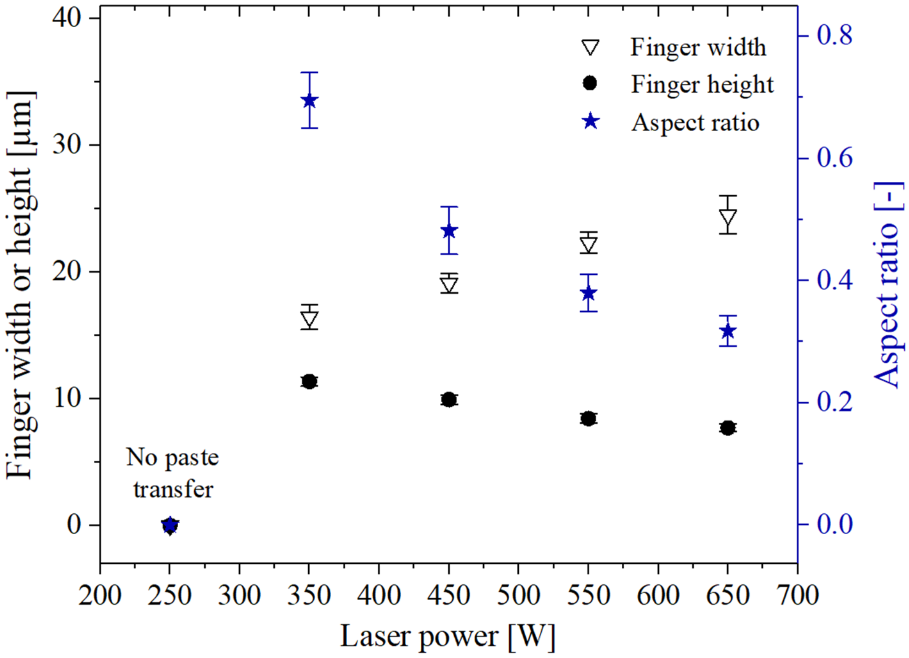

Figure 3.4: Influence of laser power on the printed finger geometry using trench design 4 [72]: finger height (circle); finger width (triangle); calculated finger aspect ratio (star).

Although the applied laser power of 350 W fabricated the highest finger aspect ratio and the minimum amount of debris, the finger interruptions due to a failure of the transfer process using this laser power setting were observed on the substrate. Interestingly, the finger interruptions occurred mainly in the middle-right part of the cell. A possible explanation for this might be that the geometry of the laser deflection system is responsible for the local inhomogeneity in laser power. This inhomogeneity decreases the laser power in a particular part of the carrier film. Hence, the generated pressure at the interface could not overcome the adhesive force between the carrier film and the Ag paste resulting in a local line interruption. No finger interruptions on the substrates were traced for the operating laser power of 450 W and above. Therefore, the operating laser power for trench design 4 (trapezoidal trench shape with 25 µm trench width), which ensures the paste deposition for whole lines without interruption onto the substrate, was determined to be

450 W. The printed finger using this laser power has an average finger width of 20 µm and an average aspect ratio of 0.48.

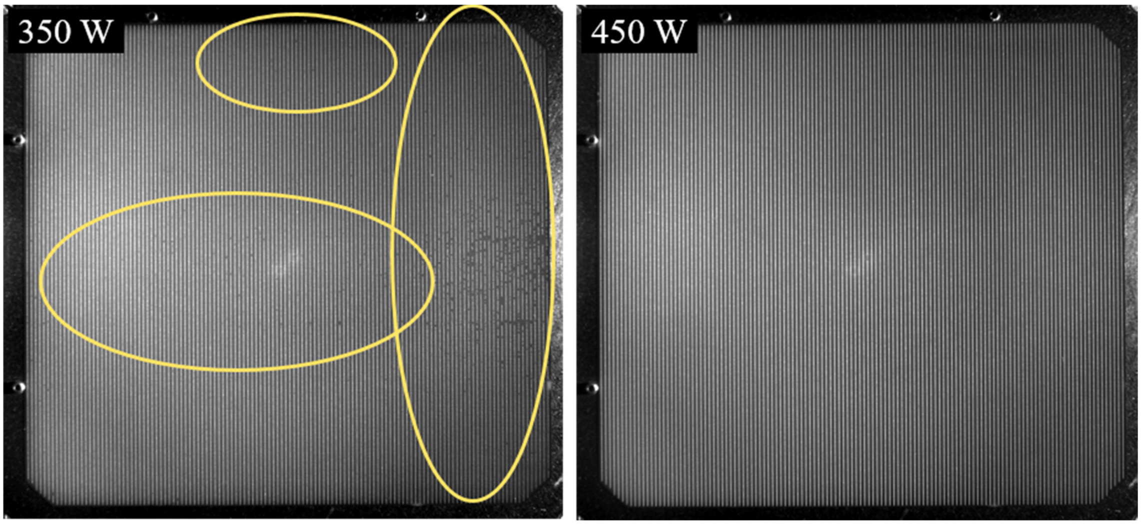

Figure 3.5: Comparison of top-view images of the PTP-printed substrates using trench design 4: (left) laser power of 350 W results in uncomplete paste transfer over the substrate area causing many line interruptions; (right) an increase operating laser power to 450 W allows a complete paste transfer over the whole substrate area. © [2020] IEEE. Reprinted, with permission, from ref [72].

PV industries have a strict requirement for the number of allowed line interruptions [123], [124]. Although it might not be the technical optimum to achieve a better cell efficiency, electrodes without any interruptions are prioritized over a slightly better line geometry. A slightly higher laser power than the laser power of optimum transfer is principally needed to avoid reliably interruptions that are caused by laser inhomogeneity. Therefore, the term laser power threshold is introduced. The laser power threshold describes the required laser power to completely transfer the paste from the entire trenches with a lower mean number of interruptions than specific criteria, e.g., three or five acceptable interruptions over the whole area of a solar cell. However, the laser power threshold will create a certain amount of debris around the Ag fingers and sacrifice the best aspect ratio of printed lines.

Three possible scenarios of the laser transfer process of PTP related to different laser powers are shown schematically in Figure 3.6. The first scenario is called no transfer, where the operating laser power is insufficient to generate enough pressure at the paste-film interface to overcome the adhesive strength between the polymer film and paste. The paste cannot be transferred and stays inside the trenches. The second scenario is called optimum transfer. This is when the operating power of the laser is adequate to generate requisite pressure in the interface region to overcome the adhesion between paste and polymer film. Thus, the paste is released and deposits onto the substrate underneath and the printed lines have an optimum geometry with only a slight trace of splashing. The last scenario is called explosive transfer. The operating laser power is notably higher than in the previous cases, exceeding the adhesive strength by far and therefore releasing the paste completely. The excess pressure not only overcomes the paste cohesion strength to remove a considerable amount of Ag particles from the main body creating debris but also accelerates the ejected paste onto the surface and deforms it towards a broader line width. The laser power decides the success of the transfer process of PTP technology and affects the print quality, including finger width, finger aspect ratio, and amount of debris. Therefore, an accurate optimization of laser power before every laser transfer process is necessary to achieve optimum print quality.

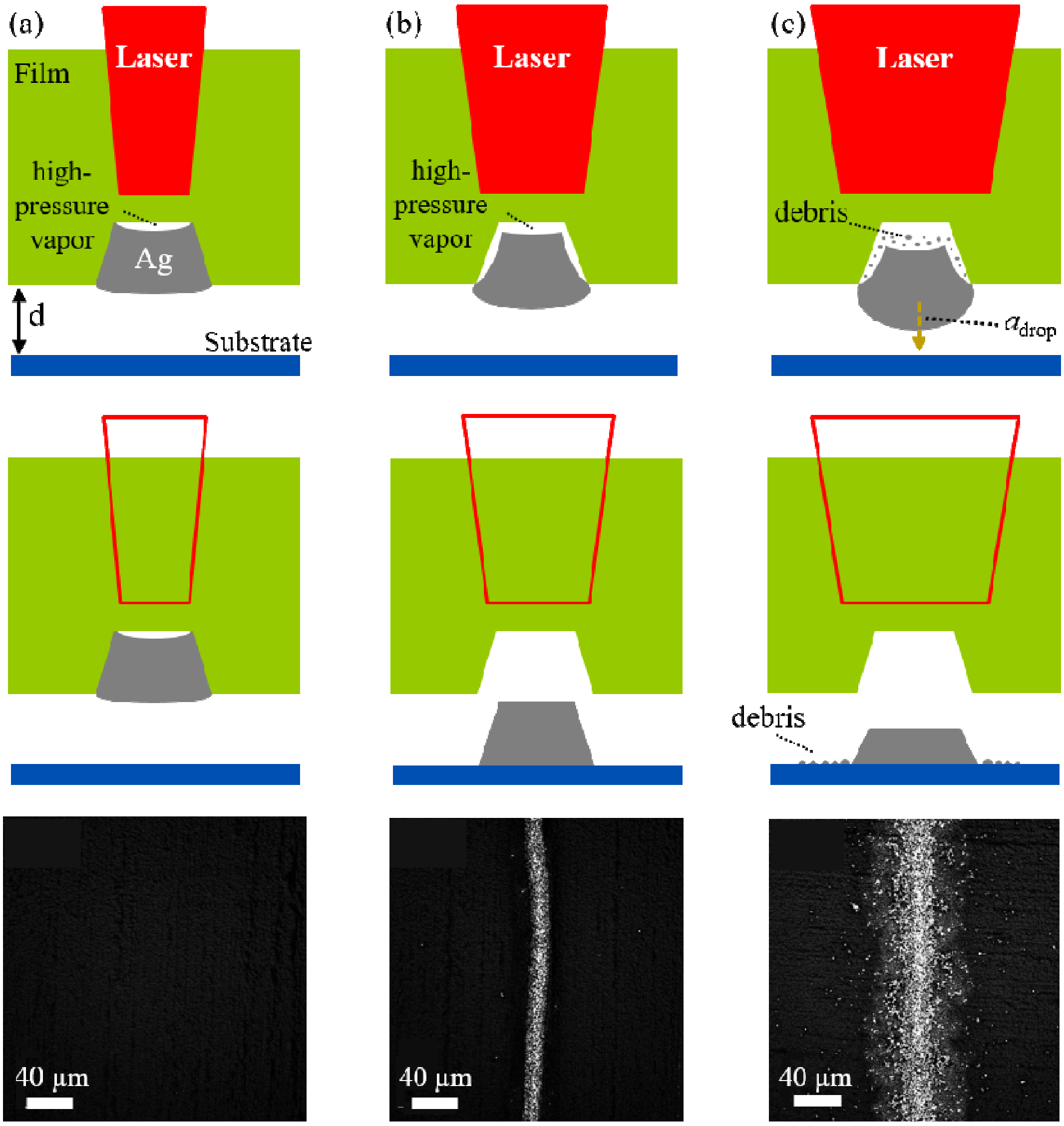

Figure 3.6: Schematic paste transfer during the PTP laser transfer process for different laser power [74]: (a) no transfer, when the operating laser is below the laser power threshold; (b) optimum transfer, for laser power slightly above the sufficient laser power fabricating the best possible finger aspect ratio; (c) explosive transfer, when the operating laser power is significantly above the laser power used for the optimum transfer generating a significant amount of high-pressure vapor layer, which is high enough to overcome the adhesion force to release the paste, to surpass the cohesion strength to create a considerable amount of debris and to accelerate the paste drops and deform Ag fingers towards a broader line width.

3.3 Investigation of laser-induced damage

A laser beam has a higher power density and may be absorbed by the material, transferring its energy to the material. Thus, the material can be heated, melted or vaporized depending on the absorbed energy into the material. PTP technology uses an infrared laser with a wavelength of 1070 nm for the laser transfer process. A laser spot of 100 µm will not only be absorbed by the paste inside the trenches with a width of 20 to 30 µm but also transmit through the film from left and right sides of the trenches to the substrate. In this section, the effect of laser irradiance on cell quality is investigated. This experiment might explain whether the laser irradiation during the PTP laser transfer process induces any laser damage to the cell surface, which may have a detrimental effect on the electrical performance of silicon solar cells.

3.3.1 Experimental details

For this experiment, the already printed and fired multi-crystalline PERC-solar cells were used to analyze the effect of the laser transfer process of PTP on the electrical performance of solar cells. The filling process was excluded and the laser irradiance illuminates through the transparent polymer film to the solar cell surface. These metalized solar cells were separated into different groups with various laser powers and laser lines on the wafer surface (see Table 3.1). Apart from laser power variation and number of laser lines, two control groups were also included in this experiment. Four cells from control group A were not laser-treated and these cells were put aside (no laser treatment & no handling), while the rest of the groups were placed into the PTP machine. Five cells from control group B were inserted into the PTP machine without turning the laser on (only handling, no laser treatment). Other groups of 12 cells were inserted in the PTP machine and irradiated with different laser powers (300, 500 and 700 W) and various laser lines (126, 252, and 336 laser lines).

Before and after treatment, the I-V parameters of all groups were measured using a HALM-flasher under standard test conditions of 25 °C and irradiance of $1000\,\mathrm{W \cdot m^{-2}}$ with an AM1.5(g) spectrum. This laser damage investigation was conducted on the same day to mitigate the measurement uncertainty from the I-V measurement. However, a linear effect of I-V parameters on cell temperature was observed, and therefore, the I-V parameters were from this temperature effect corrected with a coefficient. The photoluminescence (PL) measurements were also performed before and after laser treatment to observe if the laser induces some line damage on the surface of solar cells.

3.3.2 Results and discussions

The I-V results before and after laser treatment were compared. The delta value for each parameter was determined using the following equation:

$$\triangle = \textit{the measured value after treatment} - \textit{the measured value before treatment} \tag{3.1}$$

Table 3.1: List of groups for the laser damage investigation of PTP laser transfer process.

Group	Laser treatment	Laser power [W]	Number of laser lines
Control group A	no	0	0
Control group B	no (pass through PTP)	0	0
G1	yes	300	126
G2	yes	300	252
G3	yes	300	336
G4	yes	500	126
G5	yes	500	252
G6	yes	500	336
G7	yes	700	126
G8	yes	700	252
G9	yes	700	336

Figure 3.7 presents the delta values of *I-V* parameters from the laser-induced damage investigation. The control groups A and B served as references with the delta values from both groups were expected to be zero, when the measurement uncertainty is also zero (ideal case) and no handling damage can be assumed during the chuck transport inside the PTP machine. Even though the delta value of control group B is not zero, this insignificant difference was caused by the measurement uncertainty of the flasher and not by the damage due to the chuck transport inside the PTP machine. A dashed line depicts an ideal case, in which there is no difference between the parameter after and before laser treatment (no laser-induced damage).

The J_{sc} values for all groups after laser treatment were higher than before laser treatment, which resulted in positive ΔJ_{sc} values as shown in Figure 3.7(a). The difference between the control groups and the sample groups is minuscule and still within the measurement uncertainty range. On the other hand, the V_{oc} values for all groups after laser treatment were lower than before laser treatment, resulting in negative ΔV_{oc} values for both control groups A and B as well as other groups with laser treatment. V_{oc} loss with an average of –0.25 mV was calculated for both control groups, and the V_{oc} loss for groups with laser treatment was varied between –0.43 and –0.66 mV without any linear dependence with the increase in laser power and laser lines. The disparity of V_{oc} loss between control groups and groups with laser treatment was insignificant and still within the measurement uncertainty range, indicating no V_{oc} loss after the laser process.

For all laser powers, no notable difference in ΔFF was observed with an increase of laser lines. A similar trend was observed for $\Delta\eta$ values that the $\Delta\eta$ value of control group A is 0% and for the control group B is –0.01%. $\Delta\eta$ values for groups with laser treatment varied between –0.01% and –0.015% without any relation with laser power and the number of laser lines. In summary, no significant difference of all *I-V* parameters was observed for different laser powers from 300 to 700 W and various laser lines of 126, 252 and 336, which showed that the laser did not affect cell performance during the PTP laser transfer process.

Apart from *I-V* measurements, photoluminescence (PL) images before and after the experiment were taken and compared. Figure 3.8 compares the PL images from the control group A, and groups of 336 laser lines with the operating laser powers from 300 to 700 W. The PL images before and after the laser experiment for all groups are identical, even though the maximum laser power of 700 W and the maximum laser lines were ablated directly on the cell. Neither laser lines nor other features attributed to laser-induced damage, such as melting, recrystallization, nor stress, were detected on the cell surfaces. Hence, it is concluded that the laser induces no damage to the cell quality and performance during the laser transfer process of PTP technology.

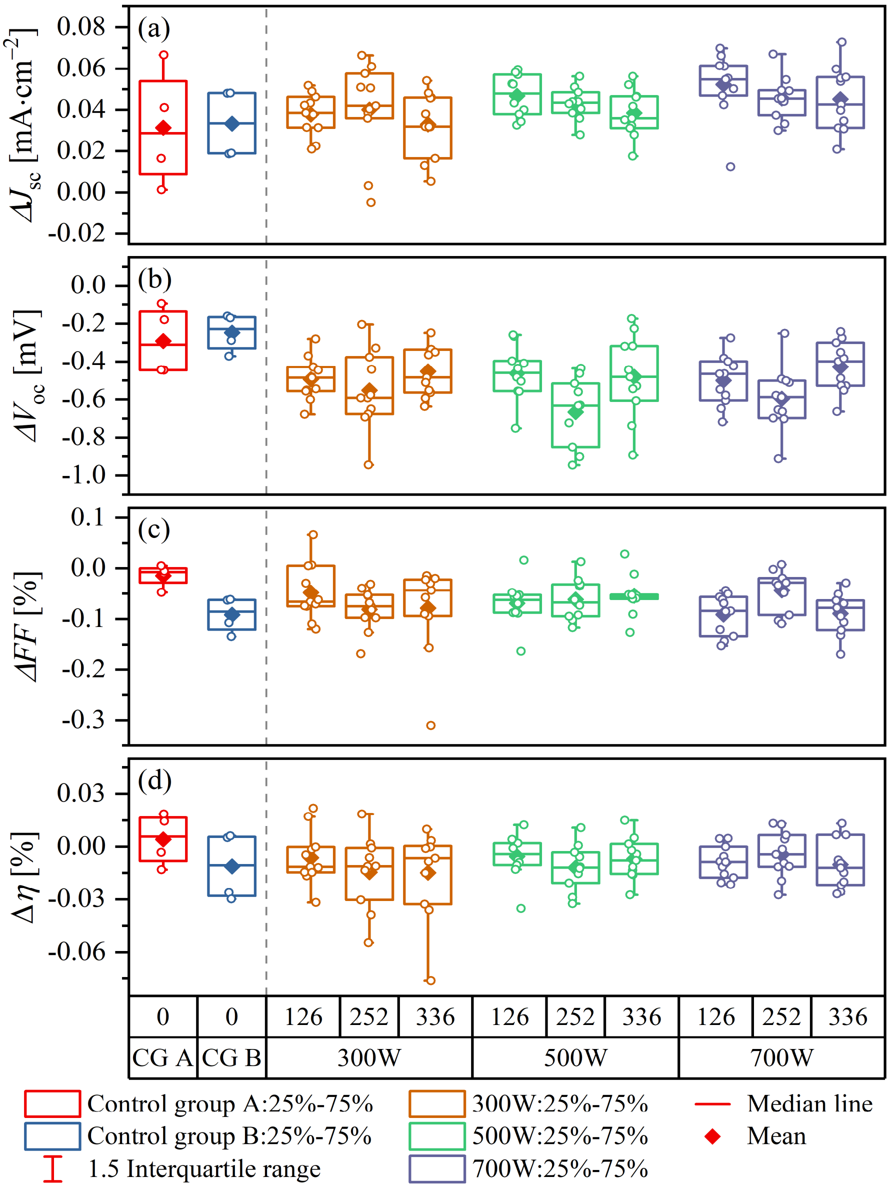

Figure 3.7: Delta values of *I-V* parameters measured according to STC: (a) ΔJ_{sc}; (b) ΔV_{oc}; (c) ΔFF; and (d) $\Delta\eta$. Delta values of each parameter were measured by subtracting the *I-V* values measured after treatment with the values measured before laser treatment.

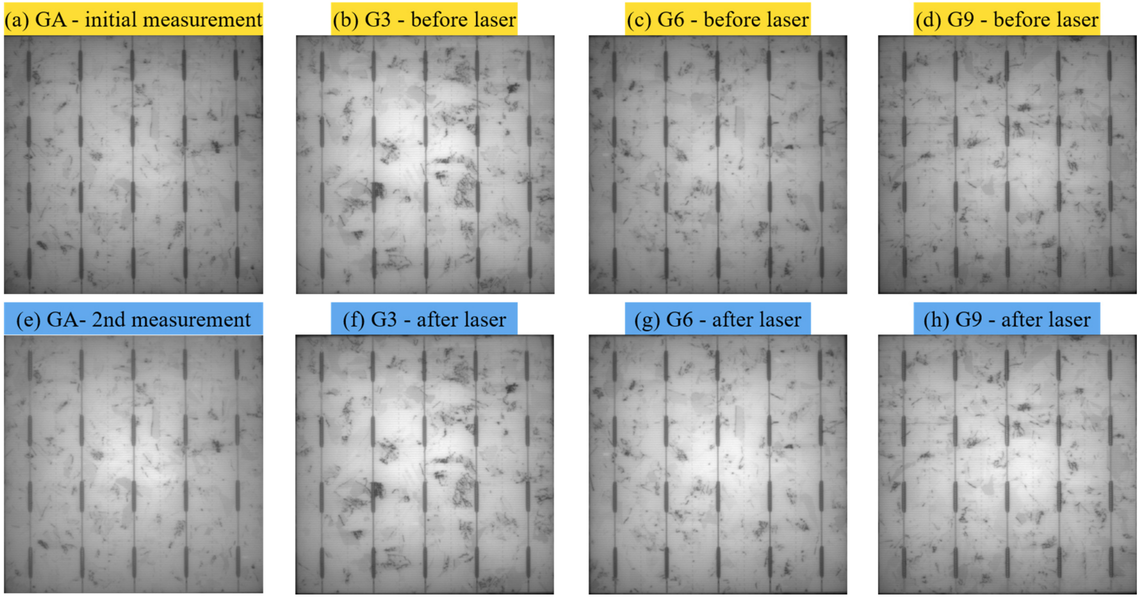

Figure 3.8: Comparison of PL images of multi-crystalline PERC-solar cells before and after laser-induced damage experiment: (a) initial measurement and (e) second PL measurement for control group A without laser treatment and cell handling; group 3 with 336 laser lines and operating laser power at 300 W before (b) and after (f) laser treatment; group 6 with 336 laser lines at 500 W before (c) and after (g) laser treatment; group 9 with 336 laser lines at 700 W before (d) and after (h) laser treatment.

3.4 Chapter summary

In this chapter, the development of PTP technology for each process is described. The F&C configuration is chosen as the standard filling process for a further experiment because it filled thick-film Ag paste sufficiently and uniformly into the trenches. By using a higher blade angle for the second squeegee, the F&C configuration is able to minimize the scooping effect leaving only a tiny area of the trenches unfilled, which are around 1 to 2 µm deep. Nevertheless, optimizing the PTP printing parameters is also essential to improve the filling quality and to ensure the cleanliness of the film surface after the filling process. A film surface with some paste residue after the filling process will increase the amount of debris on the substrate unnecessarily.

The laser power decides the success of the transfer process of PTP technology and affects the print quality, such as finger width, finger aspect ratio, and amount of debris. Therefore, an accurate optimization of laser power before every laser transfer process is necessary to achieve good print quality. Ag paste absorbs the energy from the laser during the transfer process. It leads to a temperature increase of the paste enough to vaporize the organic components of the paste in the interface region. When the high-pressure vapor at the interface is higher than the adhesive strength between the polymer film and paste, the paste is released or transferred to the substrate underneath. The increase in laser power elevates the pressure in the interface region, which is enough to overcome the adhesive strength and the cohesive force creating a splashing around the fingers.

The narrowest fingers with the highest aspect ratio are fabricated by operating the laser power at the optimum transfer. Unfortunately, the laser power needs to be slightly increased to avoid local line interruptions due to laser inhomogeneity in certain areas. Thus, the term “laser power threshold” describes the operating laser power required to remove the paste from the trenches over the whole substrate area. However, the laser power threshold will create a certain amount of debris around Ag fingers and sacrifice the best aspect ratio of printed lines. Three possible scenarios of the PTP laser transfer process related to different laser power are presented; no transfer, the optimum transfer and the explosive transfer.

The laser damage on the substrate after the laser transfer process of PTP technology is investigated. Even though the maximum operating laser power of 700 W and the maximum possible laser lines of 336 are selected, no significant differences are observed on the *I-V* parameters and PL images before and after the laser process. The results of the laser-induced damage investigation suggest that the laser irradiation during the transfer process of PTP technology is harmless and non-destructive for the substrate surface and the passivation quality of c-Si solar cells.

4 Film Material and Rheological Paste Properties for PTP Application

The laser transfer process of PTP technology for the front metallization of crystalline silicon solar cells involves three aspects: laser irradiance, transparent film with embossed trenches and Ag paste. As learned from the previous chapter, the optimization of laser power is mandatory to ensure the success of the paste transfer process, to achieve good finger geometries and to minimize the amount of debris on the substrate. This chapter[1] *aims to gain understanding related to the governing principles of the laser transfer process of PTP technology. Different film materials, film thicknesses and trench geometries formed in the surface of the transparent film are compared and their effect on the laser power are analyzed. Pastes with different rheological properties are evaluated to distinguish their influence on the laser power threshold and also the geometry of the printed fingers.*

4.1 Introduction

The PTP machine utilizes continuous-wave laser irradiation with a wavelength of 1070 nm and several lenses to generate a top-hat laser irradiance on the surface of transparent film. The absorbance of optical irradiation of Ag pastes has a wide wavelength range [125]. Therefore, the energy transmitted from the laser irradiation of PTP at a wavelength of 1070 nm can be directly absorbed by Ag pastes. It is shown in the previous chapter that an accurate laser power optimization is required not only to secure a successful paste transfer over the whole substrate area but also to attain the highest achievable finger aspect ratio and to minimize the amount of debris. This chapter focuses on two key aspects that control the PTP laser transfer process from a material point of view: the physico-chemical properties of the used Ag paste and the film material. The influences of the film and paste properties on the applied laser power are also investigated. Three different film materials with varying thicknesses are compared and their effects on the applied laser power are investigated. The impact of paste rheology on the paste spreading after the laser transfer process is studied and hence the geometry of the PTP-printed finger lines. The influence of the paste boiling point and the adhesion between paste and film material is studied. Finally, four different trench designs formed on the surface of transparent films are investigated to examine the dependence of the applied laser power on the trench geometry. By understanding the relationship between the materials and the laser power threshold, an optimum combination of film material, thickness, trench design and paste rheology can be designed to achieve a lower laser threshold in PTP-based solar cell metallization.

---

[1] This chapter 4 is partly adapted from the author´s publications:

A. Adrian, D. Rudolph, J. Lossen, and N. Willenbacher, “Investigation of Thick-Film-Paste Rheology and Film Material for Pattern Transfer Printing (PTP) Technology,” Coatings, vol. 11, no. 1, p. 108, Jan. 2021, DOI: 10.3390/coatings11010108.

A. Adrian, D. Rudolph, N. Willenbacher and J. Lossen, "Finger Metallization Using Pattern Transfer Printing Technology for c-Si Solar Cell," IEEE Journal of Photovoltaics, vol. 10, no. 5, pp. 1290-1298, Sept. 2020, DOI: 10.1109/JPHOTOV.2020.3007001. © 2020 IEEE.

4.2 Materials

4.2.1 Silver pastes

Finger lines were fabricated using six different Ag pastes rheologically designed for PTP technology based from the commercial ultrafine line screen-printing Ag paste SOL9641B from the paste manufacturer Heraeus Precious Metals, West Conshohocken, PA, USA. Both the organic and inorganic paste components from these six Ag pastes were either modified or entirely replaced to support the laser transfer process of PTP technology and to provide a good contact formation with an even ultrafine finger line. The solid content of silver and glass particles, the organic vehicle content, and the viscosity of each paste as analyzed by the supplier are given in Table 4.1. The viscosity values were measured using a viscometer and a cone plate spindle CPE-51 (Brookfield Engineering Laboratories, Inc., Middleboro, MA, USA) at one rpm and 25 °C for five minutes. The organic vehicle in a silver paste might be a mixture of solvent, thixotropic agent, surfactant, plasticizer, and other additives. The actual constituents for each paste and their proportion of organic vehicles are held confidentially by the paste manufacturer.

Table 4.1: Components and specifications of six different silver pastes modified for PTP application [74].

Paste	Solids [wt.%]	Organic vehicle [wt.%]	Viscosity [Pa·s]
A	90.74	9.26	55.9
B	91.21	8.79	247
C	89.00	11.00	186
D	90.95	9.05	186
E	90.66	9.34	150
F	91.14	8.86	143

4.2.2 Transparent polymer films

Three transparent polymer films were supplied by Utilight Ltd. (now called DR Utilight Corp Ltd., Yavne, Israel) and used to investigate the influence of film material on laser power during the laser transfer process (see Table 4.2). The transparent film made of materials M1 and M2 was embossed with two different trench geometries using a rigid pattern metal (see Figure 2.6). The transparent film of material M3 was embossed with four trench designs. The variation of the film material also accommodates a different film thickness. The standard film of M3 has a thickness of 200 μm. The film thickness of the newly made polymer materials M1 and M2 are decreased to

80 µm and 150 µm, respectively. A lower film thickness might require a lower laser power for the paste transfer, and at the same time, reduce the material cost of PTP technology.

Table 4.2: Three different films with various materials and thicknesses available for PTP technology [74].

Film material	Film thickness [µm]	Material	Trench design (see Figure 2.6)
M1	80	Polyethylene (PE)	2 and 4
M2	150	Polyvinyl chloride (PVC)	2 and 4
M3	200	Amorphous polyethylene terephthalate (APET)	1, 2, 3 and 4

4.3 Experimental details

The yield stress measurements were performed using a rotational rheometer Rheostress 150 (Thermo Fischer Scientific, Karlsruhe, Germany) equipped with a vane geometry. The shear stress was increased in steps from 1 to 3500 Pa. The yield stress values for six different Ag pastes were determined from logarithmic plots of deformation versus shear stress data obtained in the creep experiment using the tangent intersection point method (see section 2.6.2). Differential scanning calorimetry has been utilized to measure the boiling point of the liquid phase of Ag pastes using a DSC 214 Polyma, as described in section 2.6.2. An alumina crucible was filled with around 100 mg Ag paste and sealed with a pierced alumina lid. The crucible with the sample was placed side by side with a reference crucible inside a DSC. Both crucibles were heated with 20 $K \cdot min^{-1}$ at a dynamic N_2 atmosphere of 40 $mL \cdot min^{-1}$. The thermal behavior of various Ag pastes can be studied by analyzing heat flow as a function of temperature. Each measurement was performed in triplicate, always using a fresh Ag sample.

The organic vehicle of Ag pastes determines the wetting of the transparent film material. Therefore, the organic vehicle of pastes E and F was separated by centrifugation at a speed of 9000 rpm for 30 min. The three-phase contact angle of the organic component of Ag paste on the film material was measured using a customized sessile drop tensiometer. The organic liquid was squeezed from a needle with a diameter of 0.8 mm onto the polymer film. The droplet shape was recorded using a Stingray F-033 camera (Allied Vision Technologies GmbH, Stadtroda, Germany), and the contact angle was obtained via an image analysis program (ImageJ [120]). The transmission and reflection of film materials were determined using a spectrometer Lambda 950 (PerkinElmer Ltd., Llantrisant, UK) in the wavelength range between 1000 and 1250 nm. The sum of absorption, reflection and transmission of the irradiance is equal to the total irradiance. Hence, the absorption of the film materials was calculated as 100% − (transmission + reflection).

Finger electrodes from six different Ag pastes were fabricated using a pilot PTP machine with a maximum throughput of 3000 wafers per hour. The F&C configuration was adopted, and both squeegees were set at a pressure of 3.5 bar and a speed of 200 $mm \cdot s^{-1}$. Industrial pre-processed *p*-type c-Si precursors with PERC structure and M2-size of 244.32 cm^2 from a pilot line of Hanwha Q Cells (Thalheim, Germany) were used as substrates and placed underneath the film at a distance of 200 μm. To avoid electrode interruptions, a determination of the laser power threshold for each paste and film material was performed. The laser power was gradually increased from 300 W in 10 W steps until no interruption could be detected on microscopy images obtained at 5× magnification. This laser power was set as the laser power threshold for the respective paste and transparent film material.

After finger metallization, all precursors were dried at 200 °C for 15 minutes using a Baccini paternoster drying oven. Then, all substrates were sintered using a Centrotherm fast-firing furnace at a set peak temperature of 890 °C and a belt speed of 7 $\mathrm{m \cdot min^{-1}}$. Electrode morphology was imaged at 50× magnification using a confocal laser scanning microscope (CLSM) LEXT OLS4000. Three-dimensional (3D) images of printed electrodes were analyzed using the surface analysis software Mountains Technology Surface Texture Analysis Premium [102] to determine the height and the width of the printed electrodes. The finger aspect ratio was calculated by dividing finger height by finger width.

4.4 Results and discussions

This section focuses on the effect of the paste flow properties for the front metallization of solar cells using PTP technology. The influence of the organic vehicle of the Ag paste and the optical properties of the film material on the laser power threshold for the transfer process are presented and discussed separately in the subsequent sections.

4.4.1 Influence of paste yield stress on finger geometry

Finger lines were printed using four Ag pastes (pastes A, B, C and D) with film material M3 with trench design 1 (see Figure 2.6). The filling process of trenches worked smoothly with all these pastes, and no unfilled trenches could be seen after the filling process irrespective of the paste rheological properties. The measured yield stress values of the investigated paste are summarized in Table 4.3.

Table 4.3: Yield stress of four Ag pastes A–D modified for PTP technology [74].

Ag paste	Measured yield stress at 20 °C [Pa]
A	204 (σ = 13)
B	1025 (σ = 14)
C	1130 (σ = 110)
D	1623 (σ = 55)

Figure 4.1(a) and (b) show that the average finger height increases and the finger width decreases with increasing yield stress. Accordingly, the aspect ratio significantly improves with an increasing yield stress, as shown in Figure 4.1(c). Paste A with the lowest yield stress of 204 Pa resulted in the smallest aspect ratio of 0.27, and the highest aspect ratio of 0.43 was obtained with paste D with a yield stress of 1623 Pa. The theoretical aspect ratio value accessible using trench design

type 1 is 0.67. The lower aspect ratio achieved experimentally was caused by the paste spreading after deposition. To enable the spreading, the impact pressure during the paste deposition must be higher than the yield stress of each paste. The pressure imposed on the Ag line when dropped from the film trench to the wafer is given as:

$$\Delta p = \rho_{\text{paste}} \cdot g \cdot d \tag{4.1}$$

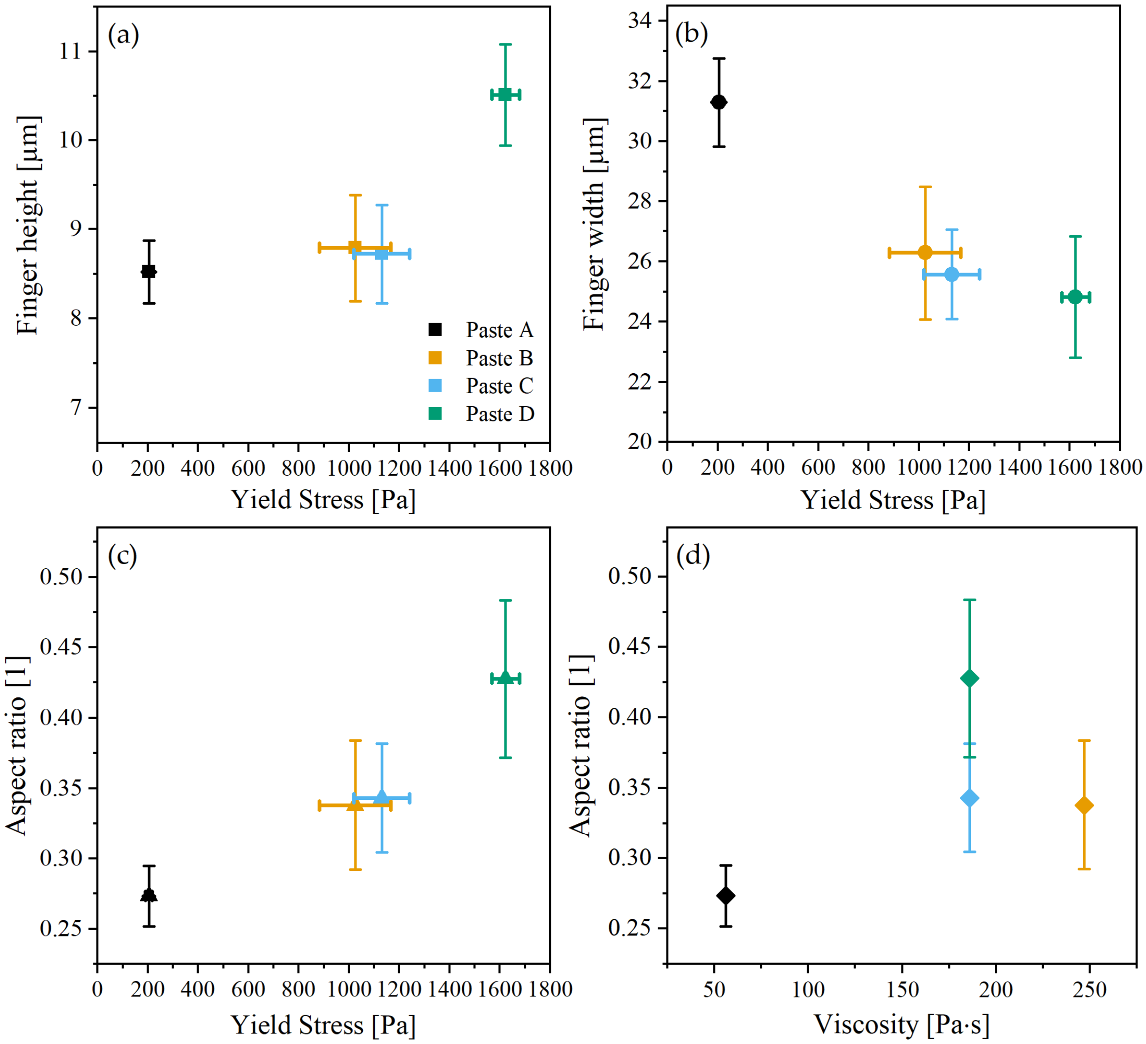

Figure 4.1: Finger geometries obtained with pastes A – D and film material M3 with trench design 1 [74]: (a) finger height; (b) finger width; (c) aspect ratio vs. yield stress; (d) aspect ratio vs. viscosity.

where $\rho_{\text{paste}} = 5700\ \text{kg}\cdot\text{m}^{-3}$ is the Ag paste density, $g = 9.81\ \text{m}\cdot\text{s}^{-2}$ is the acceleration due to gravity, and $d = 200\ \mu\text{m}$ is the distance between the film and the substrate. The value $\Delta p = 11$ Pa is well below the yield stress values of all Ag pastes obtained at 20 °C. However, two additional aspects have to be considered here. First, laser power dissipation results in vaporization of volatile paste ingredients, and the corresponding gas pressure at the paste-film interface exceeds the adhesion between paste and polymer film, providing an additional contribution to the force acting on the Ag paste during deposition. Second, the laser energy is absorbed with the Ag paste at the interface and increases the paste temperature. The Ag surface at the paste-film interface sustains the highest temperature increase. However, the paste temperature inside the trenches is also raised quite significantly due to the high thermal conductivity of Ag paste. Accordingly, the yield stress of the Ag paste decreases.

During the determination of laser power threshold, it was found out that each increase of input laser parameter by 100 W raised the surface temperature of the polymer film by 0.5 °C, observed using an infrared camera VarioCAM (InfraTec GmbH, Dresden, Germany), which was focused on the film surface from the laser side. Due to the small gap between the substrate and the polymer film, the infrared camera could not observe the increase of paste temperature during the paste transfer process directly, which is expected to be more pronounced. Figure 4.2 presents the dependence of yield stress of the Ag pastes A–F on paste temperature. Measuring the yield stress value of pastes E and F at a temperature range up to 40 °C, a linear decay was observed with a drop of the yield stress of about 25 Pa for a temperature rise of one degree Celsius. By assuming that the Ag pastes A–D also have a similar temperature behavior as pastes E and F, the required temperature for a yield stress drop below $\triangle p$ for pastes A–D is estimated. For paste A the yield stress drops below $\triangle p$ around 27 °C. For pastes B, C and D, this temperature limit is reached at 60 °C, 65 °C, and 84 °C, respectively, assuming the linear decrease to persist even at a higher temperature. Both phenomena are considered to contribute to the observed spreading of the deposited lines on solar cells. However, further experiments would be required to quantify which mechanism is more relevant for the line spreading.

Although the true pressure that acts on the deposited line and resistance of the paste against deformation could not be quantified, the results indicate that the accessible aspect ratio of Ag lines printed using PTP technology is related to the paste rheology, particularly to its yield stress. The paste viscosity, in contrast, seems not to correlate to the achieved aspect ratio, as can be seen in Figure 4.1(d). It should be mentioned that the viscosity was shown to be a decisive parameter for a proper paste transfer through the mesh screen in screen-printing technology [82], [84], [89], [90]. The findings in this experiment show that the theoretical aspect ratio of 0.67 for PTP-metallized cells with trench design 1 might be reached for Ag paste with higher yield stress or weaker dependence of yield stress on the temperature. The laser printing method of PTP technology allows a modification of Ag pastes with a wide range of yield stress even above the typical industrial Ag paste of screen-printing technology since several printing issues of screen-printing technology, such as paste clogs in the screen aperture and a reduction of screen lifetime, are for PTP technology not relevant anymore. However, an excessively high yield stress of Ag paste might deteriorate the trench filling of PTP, and further investigation is necessary to analyze this issue.

4.4.2 Influence of trench design on laser power threshold and printed finger geometries

For the PTP application, there are currently four different trench designs with different shapes and geometries available. The trench geometry is essential for PTP as it defines the finger shape, the finger cross-sectional area and the paste laydown. During the optimization of the laser power threshold, it was discovered that the trench shape has an effect on the laser power threshold as well. Figure 4.3 presents the laser power thresholds required for a successful paste transfer and the SEM images of the fingers printed using PTP technology with four available trench designs. The forms of each PTP finger are identical to the shape of their respective trench designs, which means that the shape of the fingers of trench design 1, trench design 3 and trench design 4 is trapezoidal, and for the trench design 2 the finger shape is triangular. It is observed that the trench design defines the shape and cross-sectional area of the printed fingers. The smallest finger was obtained by using trench design 3, as the trench design 3 has the smallest cross-sectional area of the trench opening compared with the other trench designs. The printed finger geometries are significantly smaller than the trench shape. This difference can be understood considering the incomplete filling process and shrinkage during the drying and the firing step. As mentioned in section 3.1, trenches are not entirely filled with Ag paste, but a certain concave meniscus with a depth of around one to two µm is built during the filling process of PTP using F&C configuration. In addition, there are three other factors that could cause the finger shrinkage: the evaporation of the solvent during the drying process, the removal of the organic binder during the burn-out phase and the sintering of the Ag paste particles at the firing process.

To investigate the effect of the trench shape and geometry on the laser power threshold, the equivalent horizontal area and the ratio between the circumference and the equivalent horizontal area $r_{\mathrm{c/h}}$ are calculated using the following equations:

$$Equivalent\ horizontal\ area = \frac{trench\ opening\ area}{trench\ height} \tag{4.2}$$

$$r_{\mathrm{c/h}} = \frac{length\ of\ the\ interface\ region\ (circumference)}{equivalent\ horizontal\ area} \tag{4.3}$$

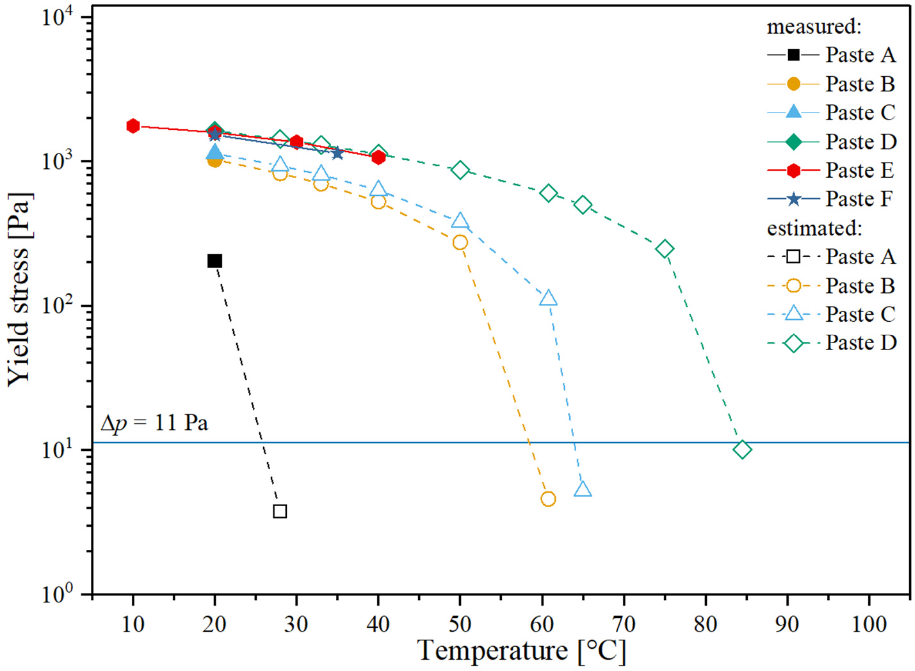

Figure 4.2: Yield stress versus temperature for Ag pastes A–F [74]. The closed symbols represent the measured yield stress values. The open symbols represent the extrapolated yield stress value of pastes A–D, assuming a linear decay of 25 Pa·K^{-1} (with dashed lines as a guide to the eye). The horizontal line at 11 Pa is the gravitational pressure imposed on Ag paste during the PTP laser transfer process onto a substrate with a distance of 200 µm.

Figure 4.4 shows the dependence of the laser power threshold on the ratio $r_{c/h}$. A higher laser power threshold is required for a trench design with a higher $r_{c/h}$ value. Trench design 1 and trench design 4 have the same trench angle and height. However, a higher laser power threshold was needed for trench design 4 due to its smaller horizontal interface area and a higher value of $r_{c/h}$ than trench design 1. The laser power required for trench design 2 was even higher because of its triangular trench shape, which has a minuscule horizontal interface area than trench design 1 and design 4, and hence the highest value of $r_{c/h}$. Trench design 3 with the lowest $r_{c/h}$-value required a slightly higher laser power threshold than trench design 1 to compensate for the laser power absorption due to the longer optical path through the transparent film corresponding to the lower trench height of trench design 3 compared with other trench designs.

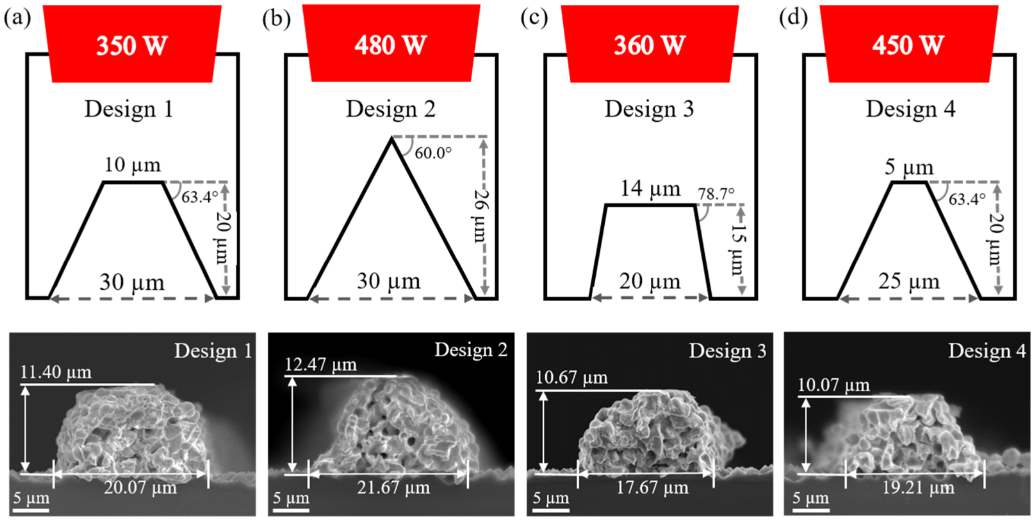
(a)
350 W
Design 1
10 µm
63.4°
20 µm
30 µm
(b)
480 W
Design 2
60.0°
26 µm
30 µm
(c)
360 W
Design 3
14 µm
78.7°
15 µm
20 µm
(d)
450 W
Design 4
5 µm
63.4°
20 µm
25 µm
Design 1
11.40 µm
20.07 µm
5 µm
Design 2
12.47 µm
21.67 µm
5 µm
Design 3
10.67 µm
17.67 µm
5 µm
Design 4
10.07 µm
19.21 µm
5 µm

Figure 4.3: Laser power threshold and cross-sectional scanning electron microscopy (SEM) images of printed finger geometries for four different trench designs: (a) trench design 1; (b) trench design 2; (c) trench design 3; (d) trench design 4. The cross-sectional view of printed fingers was observed using a spot size of 40 µm at 10 kV with a magnification of 3000×.

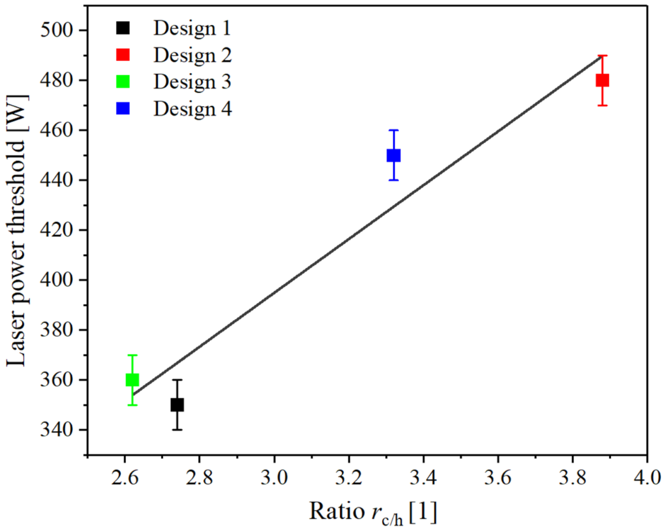

Figure 4.4: Influence of the ratio $r_{c/h}$ on the laser power threshold of paste E over a whole substrate area. The black line serves as a guide to the eye.

4.4.3 Influence of organic vehicle on silver paste regarding its relationship to laser threshold

Figure 4.5 compares the laser power threshold required to release the pastes E and F from three different film materials with embossed trench designs 2 and 4. Trench design 2 demanded a higher laser power threshold than trench design 4 for both pastes E and F. It is attributed to the higher surface to volume ratio of trench design 2 than trench design 4 (see section 4.4.2). Paste E required a higher laser power to release the paste entirely out of the trenches than paste F, irrespective of the film material. This could be related to the difference in boiling temperature as well as the different wetting of the film material of these two pastes. As described in section 3.2, a certain amount of pressure at the paste-film interface is necessary to overcome the adhesion between paste and film material. The adhesive strength is correlated to the wetting properties of the liquid organic from the paste components. The contact angle data shown in Figure 4.6(a) reveal that paste E wetted all three materials better than paste F, and a higher laser power threshold was therefore required to release this paste.

Another reason for a higher laser power threshold of paste E compared with paste F is the difference in boiling temperature between these pastes. The heat flow data presented in Figure 4.6(b) show that the peak attributed to the vaporization of the volatile components for paste F occurred at 10 °C lower temperature than for paste E. Accordingly, the latter demands a higher laser power threshold for the PTP laser transfer process. However, it should be noted that the observed differences are minor, and further investigations including pastes with a broader range of contact angles and boiling points may be helpful to corroborate the findings and to separate the contributions of wetting and boiling point differences.

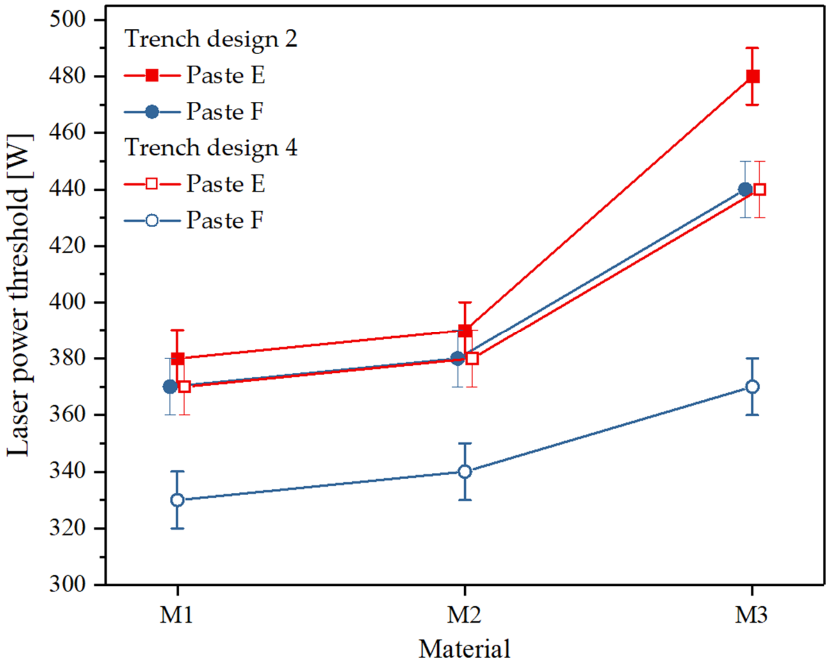

Figure 4.5: Nominal laser power threshold required to release pastes E and F from three different film materials with trench design 2 (closed symbols) and trench design 4 (open symbols) [74]. The lines serve as a guide to the eye.

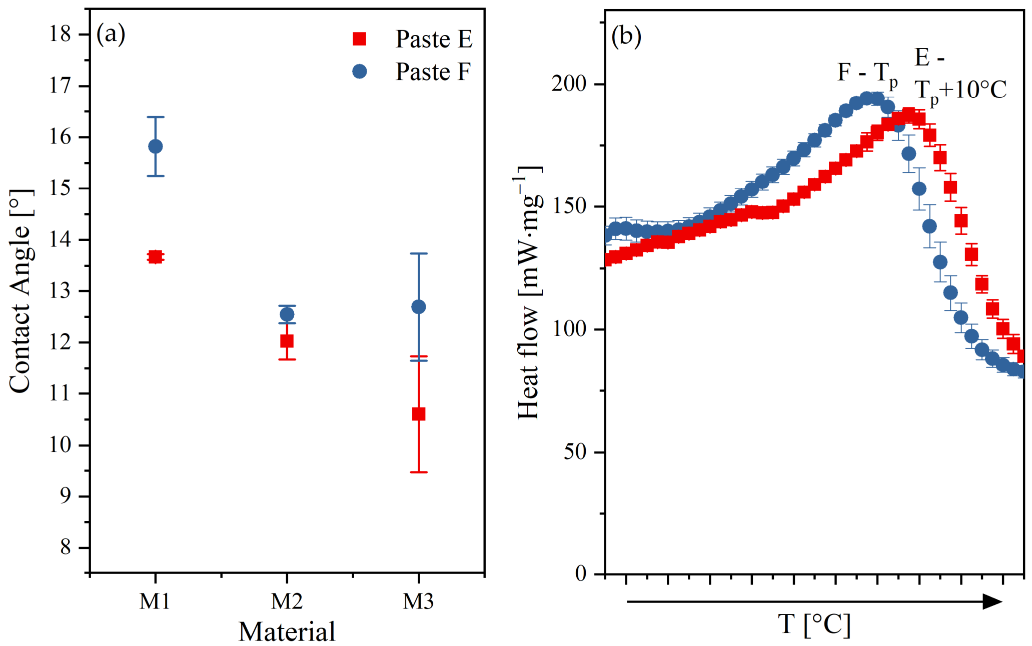

Figure 4.6: Influence of organic vehicles of pastes E and F on laser power threshold [74]: (a) contact angle of the organic vehicle of both pastes E and F on different film materials, (b) heat flow versus temperature for pastes E and F.

4.4.4 Investigation of film materials and thickness regarding how it relates to laser threshold

As presented in Figure 4.5(a), the transparent films are differently wetted by the pastes, and hence the film material significantly influences the laser power threshold. In this section, the optical properties of the polymer films are investigated on how it contributes to the differences observed in the laser power threshold. The optical properties of the three polymer film materials are listed in Table 4.4. Here, absorption is defined as the reduction of the laser irradiance due to the material itself. Material M1 with the lowest thickness of 80 µm absorbed the 0.7% laser irradiance at the wavelength of 1070 nm. Materials M2 and M3 had similar absorption of around 0.4%. Although films M2 and M3 are thicker, their absorption is lower than M1.

Table 4.4: Optical properties of three different materials for PTP at the working wavelength of 1070 nm [74].

Film material	Film Thickness [µm]	Reflection [%]	Transmission [%]	Absorption [%]
M1	80	10.63 ± 0.06	88.68 ± 0.07	0.69 ± 0.03
M2	150	9.36 ± 0.03	90.21 ± 0.02	0.43 ± 0.04
M3	200	10.01 ± 0.01	89.54 ± 0.03	0.45 ± 0.02

The low absolute absorption values and the small differences among the films indicate that the impact of light absorption on the laser power threshold is neglectable. Material M2 had the best optical properties with a transmission value of 90.21% and a reflection value of 9.36% at a wavelength of 1070 nm, followed by material M3 with a transmission of 89.54% and a reflection of 10.01%, and finally M1 with 88.68% transmission and 10.63% reflection. These data show that a significant amount of laser irradiance was reflected due to surface roughness, only a minor part of laser irradiance was absorbed by the polymer film, and the major fraction of incident laser irradiance was transmitted to the paste-film interface. Accordingly, the actual incident laser power at this interface was lower than the nominal laser power, which was set to the PTP machine for the printing experiment. This incident laser power is corrected with the transmission of the respective film to obtain the actual laser power threshold that induces paste release.

Figure 4.7 shows the comparison between the nominal and corrected laser power threshold at the paste-film interface. For both pastes E and F, as well as for both trench shapes, trench design 2 and trench design 4, the material M1 with a thickness of 80 µm still had the lowest laser power threshold, as a slightly higher value was found for material M2 with a thickness of 150 µm, and the by far highest laser power threshold was observed for M3 with a thickness of 200 µm. The results indicate that the thickness of the film material mainly defines the laser power threshold. The minor differences in light transmission do not change the clear correlation that material M1 with the lowest transmission still required the lowest laser power for paste release than M2 and M3. This result seems to be counterintuitive, but it should be kept in mind that the paste-film interface was shifted along the laser beam *z*-axis according to the material thickness, and it might not perfectly match the focal plane of the laser for all films. This seems to affect the laser power threshold and further investigations are required using films of similar thickness but made from different materials to resolve this issue. The various wetting properties of the film material of these two pastes could also play a certain role, as the lower adhesion between films and both pastes exhibited a lower laser power threshold (see Figure 4.8).

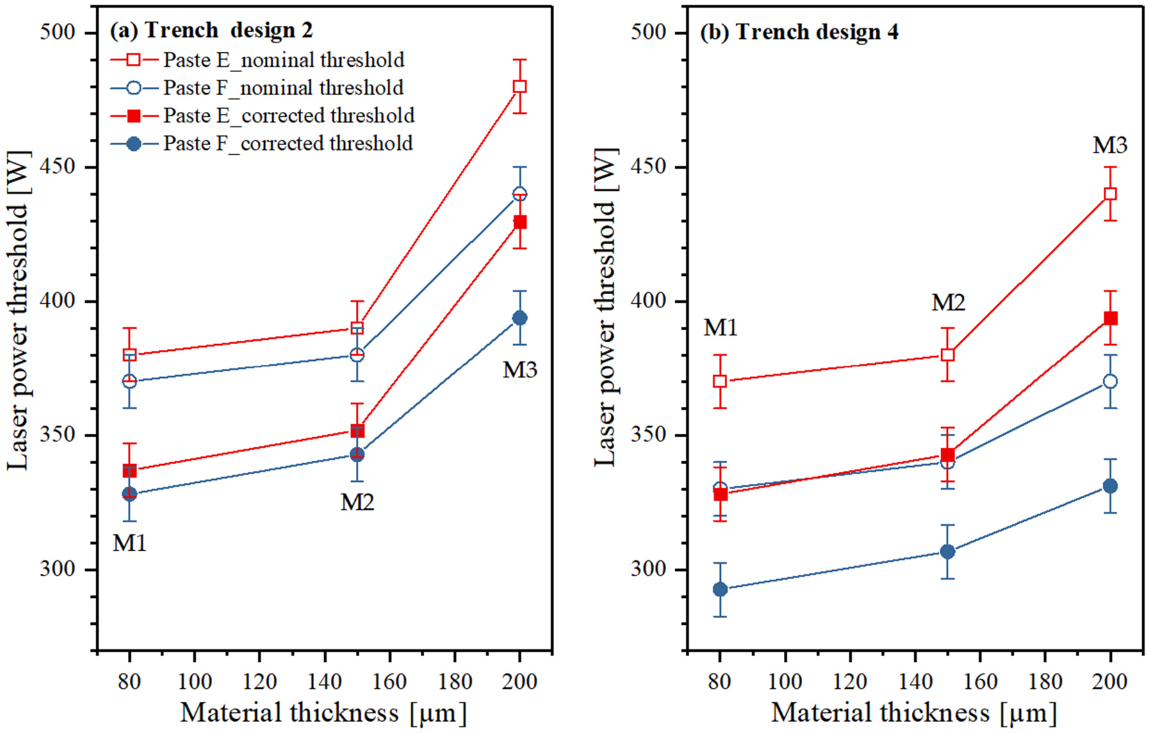

Figure 4.7: Comparison of the nominal and corrected laser power threshold of Ag pastes E and F [74]: (a) trench design 2; (b) trench design 3. The lines serve as a guide to the eye.

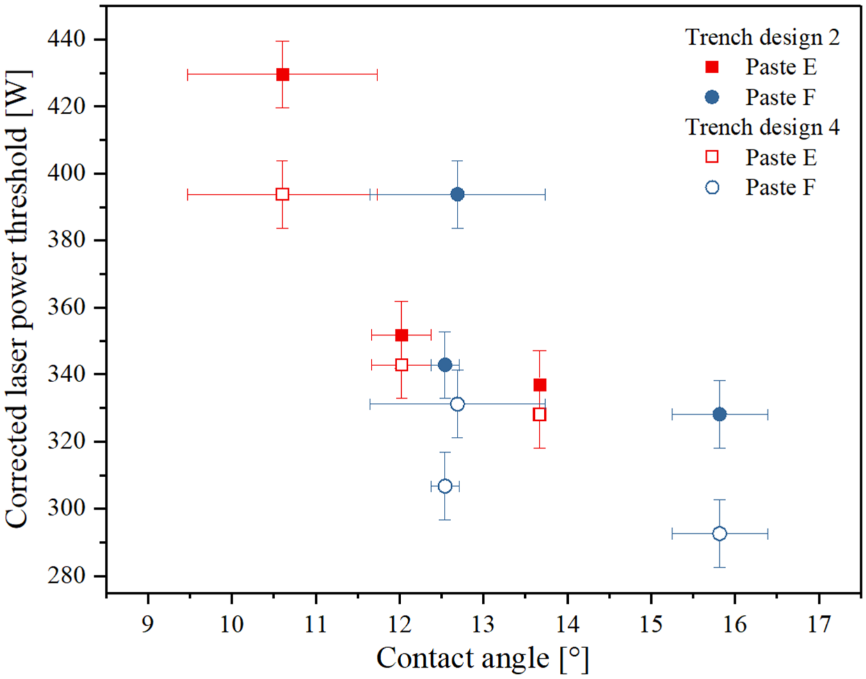

Figure 4.8: Corrected laser power threshold versus contact angle for Ag paste E (red squares) and F (blue circles), as well as trenches design 2 (closed symbols) and trench design 4 (open symbols) [74].

4.5 Chapter summary

A successful transfer process of PTP depends on the operating laser power to generate adequate pressure in the paste-film interface region. However, a higher operating laser power leads to wider finger lines of PTP and a higher amount of debris. This chapter aims to develop a better understanding of the laser transfer process of PTP technology. As the two main aspects of the PTP transfer process from a materials point of view, the influences of paste rheology and film materials on PTP application to the front metallization of solar cells are investigated. The aspect ratio of PTP printed electrodes clearly improves with increasing paste yield stress but do not correlate with its viscosity. A high paste yield stress is necessary to minimize line spreading after paste release, still even at the highest paste yield stress, the aspect ratio achieved in this experiment is still lower than the theoretical value for a given trench geometry. This suggest that the external pressure on the printed line must exceed the paste yield stress. Gravitational pressure during paste release is insignificant, but additional pressure is generated at the paste-film interface due to the vaporization of paste vehicle components. Moreover, the paste temperature increases according to localized heating due to laser irradiation leading to a reduction of paste yield stress, irrespective of the paste composition. Both phenomena seem to contribute to the observed spreading of the lines deposited on the wafer.

Four different trench designs available for PTP application require different laser power thresholds. This dependence of laser power threshold on the trench design is related to the ratio $r_{c/h}$, which is calculated by dividing the length of the interface region by the equivalent horizontal area. A higher laser power threshold is required for a trench design with a higher $r_{c/h}$ value. The trench design also defines the shape and the cross-sectional area of the printed fingers. The printed finger geometries are smaller than the trench design due to the incomplete filling process of F&C configuration and shrinkage during drying and firing.

A low laser power threshold for paste release can be achieved through a low boiling point of the organic vehicle of Ag pastes and low wettability between the paste and the film. The different film materials exhibit only slight differences regarding absorption, reflection or transmission of incident laser irradiance. Despite its low transmission ratio, material M1 with the lowest thickness of 80 µm requires the lowest laser power threshold than 150 and 200 µm for films made from M2 and M3. This may be due to the lower adhesion between material M1 and both pastes E and F, and also a better alignment with the focal plane of the laser due to a shift of the paste-film interface along the laser beam axis with varying film thickness. Further experiments are necessary to clear up this issue.

The findings in this chapter establish the basis and provide guidelines for future research into designing the Ag pastes and modifying the film materials for PTP-based solar cell metallization. Finally, narrower electrodes with a higher aspect ratio could be achieved using PTP technology at an even lower laser power threshold in the future.

5 PTP Application for Front Surface Metallization of c-Si Solar Cells

After discussing the development of PTP technology and improving the understanding of the PTP processes in previous chapters, this chapter[1] *focuses on the application of PTP technology to the front surface metallization of c-Si solar cells. The finger profiles and the performance of the solar cells fabricated using PTP technology are evaluated and compared with the state-of-the-art screen-printed solar cells as the reference. Further, the future potential of flatbed screen-printing technology is investigated using the latest screen designs available at R&D level. A radical design approach is chosen by reducing the screen aperture from 28 µm to 16 µm. I-V performance from industrial pre-processed p-type c-Si solar cells in PERC structure is shown, followed by a detailed analysis of finger geometry, finger homogeneity and printability issues. The effect of a higher busbar and finger number on the electrical parameters of PTP-metallized solar cells is studied using the cell simulation software Griddler 2.5 Pro and Gridmaster. Finally, the application of PTP technology in the mass production line of c-Si solar cells is evaluated and three possible challenges for PTP application in mass production are discussed.*

5.1 Screen-printing reference

In this section, the print quality of flatbed screen-printing technology with different screen specifications is evaluated in order to select an industrial fine-line screen available on the market as a reference from screen-printing technology for later experiments.

5.1.1 Experimental details

In the following experiment, three different fine-line screens from different screen suppliers were used to metalize Ag fingers on cell precursors. Here, industrial pre-processed *p*-type monocrystalline PERC precursors with aluminum back surface field and local contact opening on the back, as well as six busbars on the front side, from a pilot line of Hanwha Q Cells GmbH (Thalheim,

---

[1] This chapter 5 is partly adapted from the author´s publications:

A. Adrian, D. Rudolph, N. Willenbacher and J. Lossen, "Finger Metallization Using Pattern Transfer Printing Technology for c-Si Solar Cell," IEEE Journal of Photovoltaics, vol. 10, no. 5, pp. 1290-1298, Sept. 2020, DOI: 10.1109/JPHOTOV.2020.3007001. © 2020 IEEE.

A. Adrian, D. Rudolph, J. Lossen, M. Matusovsky, and V. Chandrasekaran, "Benefits of Pattern Transfer Printing Method for Finger Metallization on Silicon Solar Cells," in Proceedings of 35th European Photovoltaic Solar Energy Conference and Exhibition, Sep. 2018, pp. 434–438, DOI: 10.4229/35THEUPVSEC20182018-2CO.12.2.

Germany) were used. The precursors came from the same batch and had the same M2-size with a cell area of 244.32 cm^2. The precursors were divided randomly into four groups and each group consisted of 20 precursors. Table 5.1 lists the screen specifications and the Ag pastes used in four experiment groups to examine the state-of-the-art fine line screens from various manufacturers.

Groups G1–G3 were printed using an industrial screen-printing (SP) Ag paste SOL9641B available on the market for fine-line printing from the paste manufacturer Heraeus Precious Metals. Group G4 is a repetition of G3 using another Ag paste (the Ag paste modified for PTP, Ag paste F, from section 4.2.1). The printing step was performed using an industrial semiautomatic screen-printer from Baccini, and then all precursors were dried at 200 °C for 15 min duration using a Baccini paternoster drying oven. All samples were sintered using a Centrotherm fast-firing furnace at a peak temperature of 905 °C and a belt speed of 7 m·min^{-1}. The finger morphology was imaged at 50× magnification using a confocal LSM LEXT OLS4000 and the images were analyzed using the surface analysis software Mountains Technology Surface Texture Analysis Premium [102] to determine the height and the width of printed fingers. The *I-V* curves were measured using a flash-type solar simulator according to STC.

Table 5.1: Group distribution and the screen specifications used in this experiment.

Group	Ag paste	Screen manufacturer	Mesh angle [°]	Screen opening [µm]	Mesh count [/inch]	Wire diameter [µm]	Emulsion over mesh [µm]	Screen thickness [µm]
G1	Standard SP paste	Murakami	22.5	28	440	13	15	35
G2	Standard SP paste	Koenen	22.5	25	360	16	10	37
G3	Standard SP paste	Hans Frintrup	0	28	400	16	15	39
G4	PTP paste	Hans Frintrup	0	28	400	16	15	39

5.1.2 Results and discussions

The various screen parameters and Ag pastes resulted in different finger geometries. Figure 5.1 shows the finger geometry analysis from the four groups with various screen specifications using screen-printing technology. G1 and G2 had the same mesh angle of 22.5° and were printed using the same Ag paste. Even though the screen of G2 had a smaller nominal screen aperture by 3 µm than G1, the finger width of G2 was averagely 5 µm wider than the finger width of G1. The metalized fingers of G2 apparently could not maintain their form after the printing, which can be concluded from a lower finger height than G1 although its higher screen thickness and wider fingers despite its lower screen opening. The height loss was caused by a significant slumping of the Ag paste directly after the screen-printing process, similar behavior has been reported previously [88], [126]–[128] and affected enormously the aspect ratio of the printed fingers of G2. The screen of G3 with the knotless screen, where the mesh is aligned parallel to the screen openings (at 0° angle), aims to fabricate fingers with better geometries, which are narrower and higher than the fingers of G1 with an industrial mesh angle of 22.5°. This leads to a significant difference in the finger aspect ratio.

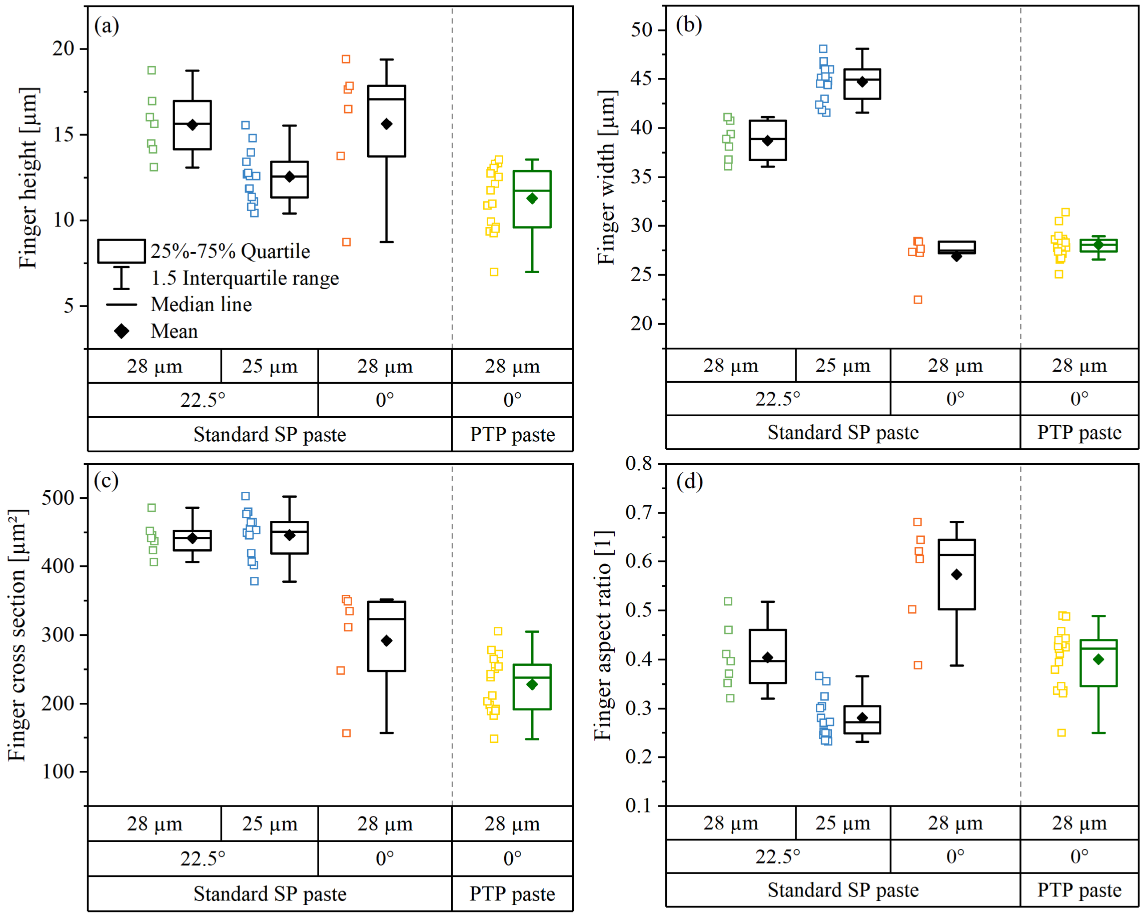

Figure 5.1: Finger geometry analysis from four groups printed using screen-printing technology with different Ag pastes and screen parameters: (a) finger height; (b) finger width; (c) finger cross-sectional area; (d) finger aspect ratio. CLSM images were taken at 50× magnification and analyzed using the surface analysis software Mountains Technology to obtain the finger geometries.

G1 has an average finger width of 39 µm with an average aspect ratio of 0.4, and G3 has significantly finer fingers with an average width of 28 µm and a high aspect ratio of 0.57. The same screen with a mesh angle of 0° for G3 and G4 resulted in a similar finger width of around 27.5 µm, but G3 has a better aspect ratio due to a higher finger height than G4 because the Ag paste F used for G4 was not designed for the screen-printing application. A similar finger cross-sectional area of around 445 µm^2 was achieved by groups G1 and G2. The knotless screen of G3 and G4 with the same screen opening of 28 µm as G1 resulted not only in a smaller finger width but also in a lower finger cross-sectional area of 285 µm^2 and 225 µm^2, respectively.

The electrical performance of the screen-printed cells of each group was characterized by the J_{sc}, V_{oc}, FF and cell efficiency η. Corresponding results for all groups with various screen specifications and Ag pastes are shown in Figure 5.2. The finger geometries affect the I-V parameters. G1 with an average finger width of 39 µm resulted in an average J_{sc} of 40.5 mA·cm^{-2}, and the average J_{sc} value of G2 is around 40.3 mA·cm^{-2} caused by its higher shading from 5 µm wider fingers. Although groups G3 and G4 had a similar finger width, both groups had different J_{sc} values due to the printability issue of G3. G3 achieved the lowest J_{sc} value, but G4 had the highest J_{sc} value of 40.7 mA·cm^{-2} due to its lowest shading loss compared with other groups. For all groups, the V_{oc} values are quite similar and varied between 672 and 677 mV. The slight difference in V_{oc} values can be attributed to different metal fraction areas, resulting in reduced recombination in groups G3 and G4.

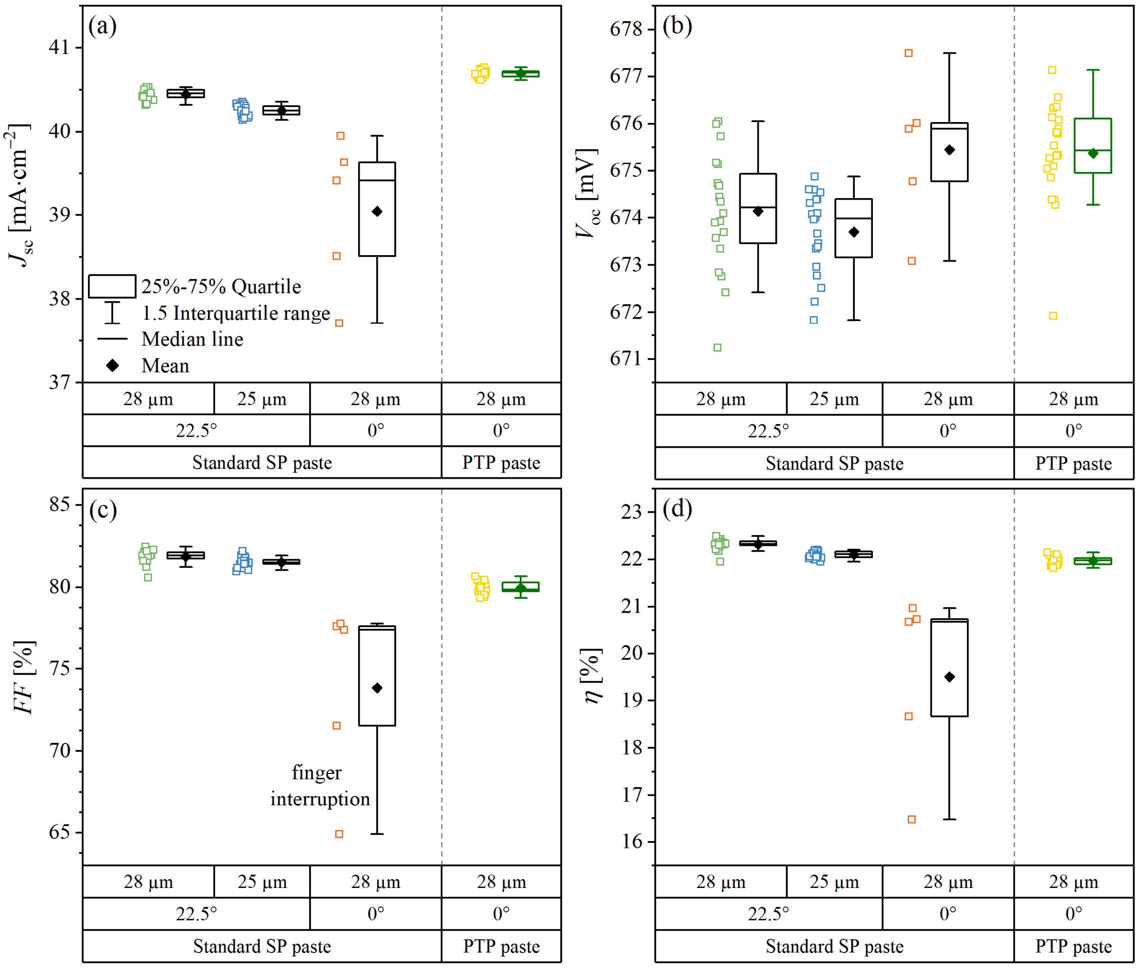

Figure 5.2: *I-V* parameters of four groups printed using screen-printing technology with different Ag pastes and screen specifications: (a) J_{sc}; (b) V_{oc}; (c) *FF*; (d) cell efficiency η. *I-V* measurements were conducted under STC.

Group G3 suffered greatly from the printability issue, which caused massive line interruptions over the cell area, leading to significantly high series resistance. Therefore, cells of G3 exhibited a substantial *FF* loss resulting in lower cell efficiency η values. The printability issue that appeared in G3 could be solved using the same screen but with a different Ag paste (G4). The average *FF*-value of G4 is 80% and lower than groups G1 and G2 caused by its lower finger cross-sectional area leading to higher series resistance. The highest η was achieved by G1 followed by G2 and G4. With the knotless screen used for G3 and G4, no continuous finger lines could be printed with the standard SP paste. This interruption problem could be solved by using the PTP paste, however, the resulting finger shape is not optimum since the finger cross-sectional area and aspect ratio are too low. This means that the industrial standard SP paste SOL9641B is incompatible with the knotless screen of G3 and G4, and a modified Ag paste could potentially perform better results. Solar cells of group G1 obtained the average finger width of 39 μm, which is equal to the average finger width achieved using the standard screen-printing technology on the industrial scale [16]. Therefore, the screen specifications of G1 with the best cell performance are chosen to be the reference from screen-printing technology for comparison with PTP technology.

5.2 Benefits of PTP technology for front metallization

In this section, the application of PTP technology to the front metallization of PERC solar cells is investigated. The deposited printed geometry and the electrical performance of PTP-printed solar cells are evaluated and compared with the screen-printed cells with the state-of-the-art screen for the industrial screen-printing application. In addition, the wet paste consumption of reference screen-printing and PTP groups with various trench designs are also investigated.

5.2.1 Experimental details

A different pre-processed batch of M2-sized PERC solar cells from a pilot line of Hanwha Q Cells with aluminum back surface field and local contact openings on the rear and six busbars on the front side were used in this experiment. The front metallization of four groups corresponding to various trench geometries, as shown in Figure 2.6, was printed using PTP technology, and the front metallization of one control group (reference) was applied using screen-printing technology. Table 5.2 lists the printing parameters for all groups in this experiment. As the reference group, 15 randomly selected precursors were printed using a commercially available Ag paste for ultra-fine line printing SOL9641B from Heraeus Precious Metals and a standard industrial screen from company Murakami Co., Ltd. (mesh angle of 22.5°, 440 meshes per inch, wire diameter of 13 μm, emulsion over mesh (EOM) of 15 μm and screen aperture of 28 μm; see section 5.1). Front metallization with 112 fingers was performed using an industrial semiautomatic screen printer from Baccini at the same printing speed and flooding speed of 150 $mm \cdot s^{-2}$. A snap-off distance was set at 1.8 mm, and the squeegee blade had a 75° Shore hardness and formed a 60° angle with the screen. The experimental PTP groups also consisted each of 15 randomly selected precursors. The Ag paste SOL1349 from Heraeus Precious Metals (see Ag paste E in section 4.2.1) was chosen, which was a rheologically adapted version for PTP application from the commercial screen-printing paste SOL9641B featuring a higher yield stress.

After the finger metallization, all samples were dried using a paternoster drying oven at a peak temperature of 200 °C with 15 min cycle duration and then sintered at a peak temperature of 890 °C and a belt speed of 7 $m \cdot min^{-1}$ using a fast-firing furnace. Three-dimensional confocal images of the printed fingers after sintering were taken using a CSLM LEXT OLS4000 and these images were analyzed using an analysis software Mountains Technology Surface Texture Analysis Premium [102] to determine the finger geometries, e.g. finger height, finger width and finger cross-sectional area. Furthermore, cross-sectional images of each group were taken using SEM. *I-V* curves of the solar cells were measured using a xenon flash-type solar simulator cetisPV. For the analysis of series resistance, the measurements were performed in two pasts; contact resistivity measurement and finger line resistance measurement. The contact resistivity was determined based on the transfer length method (TLM) using a GP 4-Test Pro. The lateral finger resistance was measured using a customized four-point-contact measurement setup. Two cells per group were randomly selected and each cell was cut into two strips of 22 mm for finger resistance measurement and six strips of 10 mm width, which were used for contact resistivity measurement.

Table 5.2: Group distribution and printing parameters of four PTP groups and the SP reference group. © [2020] IEEE. Reprinted, with permission, from ref [72].

Group	Trench geometry	Ag paste	Finger number	Trench opening area [μm^2]	Laser power threshold [W]
Ref-SP	Screen-printing	SOL9641B	112	-	-
PTP 1	Design 1	Paste E	112	400	350
PTP 2	Design 2	Paste E	112	390	480
PTP 3	Design 3	Paste E	126	255	360
PTP 4	Design 4	Paste E	126	300	450

5.2.2 Results and discussions

Figure 5.3 presents the cross-sectional SEM images of the printed fingers obtained by PTP using various trench geometries compared to those obtained by screen-printing. The fingers from the PTP groups were significantly lower than the SP reference group, and the shape of each PTP finger was similar to its trench shape. The printed finger geometries, i.e., finger width, finger height and finger cross-sectional area, were evaluated with better statistics from the CLSM images. The finger aspect ratio was calculated as the ratio between finger height and finger width, and corresponding results are shown in Figure 5.4.

The SP reference group has a roundish finger geometry, which is a typical finger shape from the actual solar cell production, with a finger width of around 38 μm and an aspect ratio of 0.37. The group PTP 1 exhibits an average finger width of 22 μm with an aspect ratio of 0.55. Although the PTP 1 and PTP 2 have the same trench bottom opening of 30 μm, the trench used in PTP 2 yields a narrower finger width of 20 μm and a higher aspect ratio ($AR = 0.63$). Using a smaller trench geometry for PTP 3 and PTP 4, a finger width below 20 μm was achieved. PTP 3 exhibits the lowest finger width ($w_f = 18$ μm) with an average finger aspect ratio of 0.51. The group PTP 4, which has the same trench wall slope angle of 63.4° as PTP 1, is expected to have a lower finger width than PTP 1 and maintain the same aspect ratio as PTP 1. The average finger width indeed was lower ($w_f = 20$ μm), but the finger aspect ratio was unexpectedly lessened ($AR = 0.48$). This may be caused by a higher laser power threshold required compared with the trench pattern with the same trench angle (PTP 1) and wider top trench with (PTP 3), as described in section 3.3.

Figure 5.5 displays the cross-sectional area of the fingers, the Ag paste laydown, and the shading area due to debris for four PTP groups in comparison with the reference group. The screen-printed reference has a finger cross-sectional area of 400 μm^2 and its wet paste laydown was 0.61 mg per contact finger. The finger cross-sectional area of PTP groups is related to the trench opening area on the transparent polymer film. The smaller the trench opening area, the smaller the cross-sectional area of the PTP fingers. The smallest finger cross-sectional area ($A_{\text{finger}} = 139\ \mu\text{m}^2$) was achieved for PTP 3 with a trench opening area of 255 µm^2. The area of trench opening also determines the paste laydown of PTP groups. PTP 1 with trench opening of 400 µm^2 consumed 0.28 mg of silver paste per finger, which was 54% less silver paste than the screen-printed reference group. Using the smallest trench opening area of 255 µm^2, only 0.16 mg of silver paste was required to fabricate fingers with a width of 18 µm and an aspect ratio of 0.51. Hence, 74% less silver paste was used for group PTP 3 than for the reference.

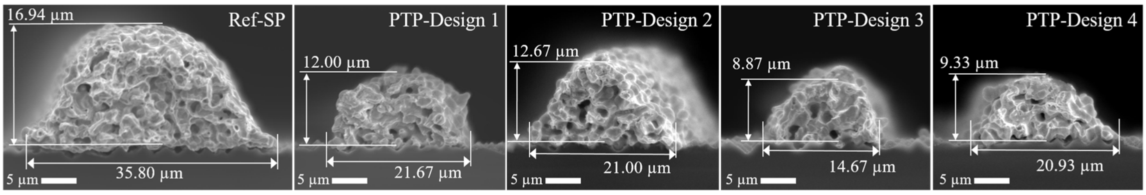

Figure 5.3: Cross-sectional SEM images of the finger lines printed using screen-printing technology (as reference) and PTP technology with four different trench shapes. The cross-sectional view of the printed fingers was recorded using a spot size of 40 µm at 10 kV with a magnification of 3000×. © [2020] IEEE. Reprinted, with permission, from ref [72].

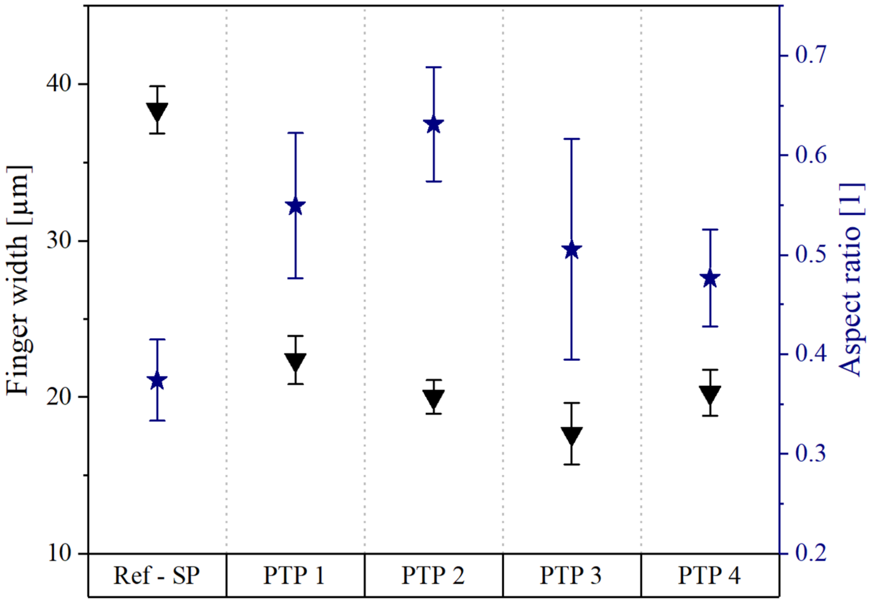

Figure 5.4: Finger geometry analysis for the four PTP groups with different trench geometries as well as the screen-printed (SP) reference: finger width (black triangle) and finger aspect ratio (blue star) [72].

Debris was observed around the PTP fingers. By converting the CLSM-images to binary images, the shading area due to debris around a finger with a length of 256 µm was determined. The total shading area of the debris of each group was calculated by multiplying the shading area caused by the debris of the observation area of 256 µm × 256 µm with the respective finger number and the ratio between the actual finger length and the observed finger length, and then by dividing it with the total area of a solar cell. The screen-printed fingers of the reference group also have some debris, but the amount is insignificant compared with the PTP groups. The average total shading area of the debris was different for each trench geometry and varied from 0.11% and 0.17% of the total cell active area.

The effect of the different PTP finger shapes obtained with various trench geometries on the *I*-*V* curve of the solar cells is shown in Table 5.3, where the average of electrical parameters and also the *I*-*V* data obtained for the cell with the highest efficiency from each group are listed. The short-circuit current density J_{sc} increases for all PTP groups compared with the screen-printed reference as a result of their narrow finger widths, which leads to less shading, and hence more light can be collected over the whole cell surface. The groups PTP 1 and PTP 2 with the same number of fingers ($N_{\mathrm{f}} = 112$ fingers) as the screen-printed reference offer a J_{sc} gain of around 0.4 mA·cm^{-2}. The increase in finger number for PTP 3 and PTP 4 to 126 fingers partially reduced the J_{sc} gain. Therefore, a J_{sc} gain of PTP 3 was only 0.4 mA·cm^{-2} despite the fingers from PTP 3 had the lowest width ($w_{\mathrm{f}} = 18$ µm), and PTP 4 ($w_{\mathrm{f}} = 20$ µm) just gained 0.23 mA·cm^{-2}. The narrow finger width achieved with PTP ($w_{\mathrm{f}} < 25$ µm) not only results in a J_{sc} gain but also provides a lower contact area fraction than screen-printing ($w_{\mathrm{f}} = 38$ µm). Therefore, the open-circuit voltage V_{oc} of the four PTP groups was 2 to 3 mV higher than for the SP reference. This V_{oc} gain can be rationalized based on its dependence on short-circuit current and recombination current [47] as follows:

$$V_{\mathrm{oc}} \approx V_{\mathrm{T}} \cdot (\ln J_{\mathrm{sc}} - \ln J_0) \tag{5.1}$$

where V_{T} is the thermal voltage and J_0 is the dark saturation current density. Calculating the influence of J_{sc} and J_0 on V_{oc} gain using equation (5.1) and the *I*-*V* parameters from Table 5.3, with the assumption of a constant V_{T} of 25.7 mV under STC, shows that 90% of the V_{oc} gain for the PTP groups is related to the reduced recombination losses of the narrower finger width and the remaining 10% is mainly due to the increase of J_{sc}.

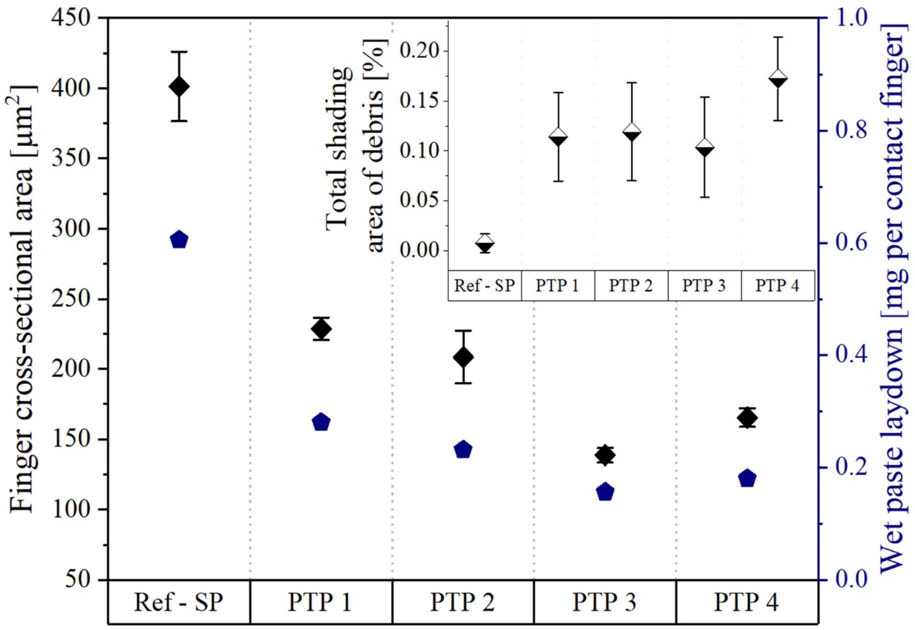

Figure 5.5: Comparison of finger cross-sectional area (black diamond), wet paste laydown (blue pentagon) and total shading area of the debris for the various PTP groups as well as the screen-printed reference [72].

Table 5.3: Best and average *I-V* parameters of the SP reference group and four PTP groups measured under STC. © [2020] IEEE. Reprinted, with permission, from ref [72].

Group		J_{sc} [mA·cm^{-2}]	V_{oc} [mV]	FF [%]	pFF-FF [%]	η [%]
Ref-SP	Best	40.05	671.0	80.4	2.30	21.61
	Average	40.00 ± 0.04	670.6 ± 1.0	80.1 ± 0.2	2.48 ± 0.1	21.49 ± 0.07
PTP 1	Best	40.41	673.1	79.9	2.77	21.73
	Average	40.40 ± 0.04	672.9 ± 0.9	79.4 ± 0.2	3.22 ± 0.3	21.58 ± 0.08
PTP 2	Best	40.42	674.1	79.5	3.26	21.66
	Average	40.43 ± 0.04	673.5 ± 1.0	79.2 ± 0.2	3.55 ± 0.3	21.53 ± 0.11
PTP 3	Best	40.43	674.0	78.7	4.18	21.44
	Average	40.45 ± 0.06	673.7 ± 1.0	78.0 ± 0.4	4.66 ± 0.4	21.25 ± 0.11
PTP 4	Best	40.30	673.0	79.4	3.35	21.54
	Average	40.23 ± 0.07	672.4 ± 2.4	78.6 ± 1.0	3.97 ± 0.6	21.24 ± 0.35

Although the J_{sc} and V_{oc} values for the PTP groups are higher than the SP group, the *FF* of the PTP groups is notably lower. The *FF* results are correlated with the finger cross-sectional area (see Figure 5.5). PTP 3, which has the lowest cross-sectional area and also finger width, suffers the highest *FF* loss of 2%. PTP 1 with the highest cross-sectional area of all PTP groups had an average *FF* loss of 0.7% compared with the reference group. Looking at the *pFF–FF* values, which represent the *FF* loss due to the total series resistance, the *FF* decrease for all PTP groups can be explained with the increase of series resistance. With the combination of J_{sc}, V_{oc} and *FF*, the cell efficiency η was determined. The groups PTP 1 and PTP 2 achieved a higher average cell efficiency compared to the reference. The J_{sc} and V_{oc} gain of groups PTP 3 and PTP 4 could not compensate for the significant *FF* loss, and their average cell efficiency was around $0.2\%_{abs}$ lower than the efficiency of screen-printed cells. The champion cell efficiency was 21.73%, which was $0.12\%_{abs}$ higher than the best screen-printed cell and was achieved in group PTP 1 with the trapezoidal trench geometry with trench opening of 30 µm.

Using the simulation software Gridmaster, the contribution of series resistance to the *FF* loss of PTP 3 compared to the best group PTP 1. A higher series resistance, mainly caused by a higher contact resistivity and a higher lateral line resistance of PTP 3, contributes to a *FF* loss of 0.64% and 0.77%, respectively. In order to take advantage of the narrow finger width and high aspect ratio of PTP 3, the series resistance loss should be further reduced, e.g., by paste development for lower contact resistivity and additionally by decreasing the total finger resistance by increasing the number of busbars, considering the current cell setup was using only six busbars.

In this experiment, the dominant contributions to the power loss due to the series resistance of the solar cells are expected to be the contact resistance between Ag fingers and emitter, as well as the lateral resistance of Ag fingers. Figure 5.6 displays the contact resistivity and the lateral finger resistance values for each group. The contact resistivity of the SP reference is around 4.5 mΩ·cm^2. The contact resistivity of PTP 1 and PTP 2 is lower than the contact resistivity of the SP group. The contact resistivity of PTP 3 and PTP 4 is slightly higher than PTP 1 and PTP 2 but on the same level as the reference. This increase in resistivity could be caused by its lower finger cross-sectional area than the cross-sectional area of PTP 1 and PTP 2, resulting in lack of glass frits for etching the SiN_x layer and forming Ag crystallites at the paste-emitter interface. These results suggest that the development of the Ag paste E is already suited for finger metallization with A_{finger} more than 200 µm^2, but a further reduction in the cross-sectional area ($A_{\text{finger}} < 200$ µm^2) will necessitate another paste modification to achieve a lower contact resistivity.

The average lateral finger resistance of the SP reference is around 0.56 $\Omega\cdot\text{cm}^{-1}$. The lowest lateral finger resistance for the PTP groups is achieved by PTP 1 with 1.23 $\Omega\cdot\text{cm}^{-1}$ and is approximately two times higher than SP reference. Among all PTP groups, PTP 3 gave the highest lateral finger resistance of 2.15 $\Omega\cdot\text{cm}^{-1}$ due to its lowest finger cross-sectional area. The variation of the lateral finger resistance of one finger correlates with the finger cross-sectional area A_{finger}, the finger length L, and the electrical conductivity of the finger ρ_{finger}. The lower the cross-sectional area of PTP fingers, the higher the lateral finger resistance R_{f}, as shown in the following equation [23]:

$$R_{\text{f}} = \frac{1}{3} \cdot \rho_{\text{finger}} \cdot \frac{L}{A_{\text{finger}}}. \tag{5.2}$$

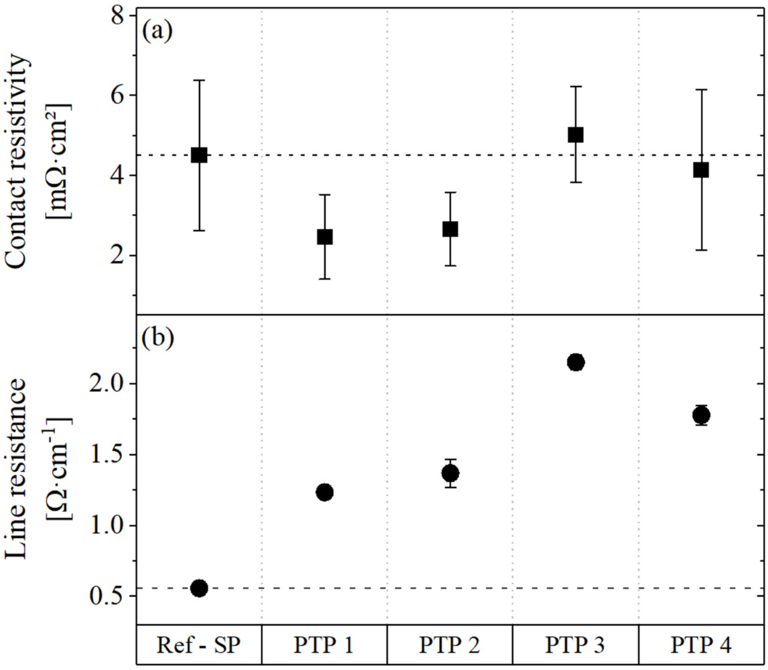

Figure 5.6: Series resistance analysis of four PTP groups compared with the screen-printed reference: (a) contact resistivity; (b) lateral finger resistance. © [2020] IEEE. Reprinted, with permission, from ref [72].

5.3 Optimization of metal grid design for PTP

The analysis of the contact resistivity and the lateral finger resistance shows that the high electrical series resistance of front metallization using PTP is caused mainly by the lateral finger resistance due to the smaller finger cross-sectional area. In this section, the electrical properties of a PERC cell were reproduced using the finite-element simulation software Griddler 2.5 Pro [129] to get a clear view of the cell efficiency dependence on the contact resistivity and the lateral resistance of PTP fingers. Figure 5.7 depicts the simulation analysis of the influence of contact resistivity on the *FF* and cell efficiency. Using the cell properties and the electrical properties of the best cell from the group PTP 1 as input parameters, the influence of contact resistivity of the front finger metallization on the *I-V* parameters. This simulation is based on the assumption that the metal fraction area and the metal recombination remain the same for all changes in the contact resistivity values. Thus, the J_{sc} and V_{oc} remain constant within the range of the contact resistivity simulated. By reducing the contact resistivity from 2.9 to 1.5 mΩ·cm^2, the *FF* increases by 0.77% and therefore the cell efficiency improves to 21.86%. Every increase in contact resistivity by 1 mΩ·cm^2 reduces the *FF* by 0.31% and the cell efficiency by 0.09%$_{abs}$.

To minimize resistive losses of the fingers printed using PTP technology, the transport distance of the generated electron muss be reduced, practically by increasing the number of busbars. The generated electrons flow from the bulk through the fingers to the busbars. Therefore, the lower the distance from the finger to the busbar, the lower the lateral finger resistance. By increasing the number of busbars, the distance between the fingers to the busbar can be shortened. The lateral finger resistance depends quadratically on the number of busbars [130], and an increase in busbar number significantly reduces the finger resistance contribution to the total series resistance. Using the Griddler software, the effect of the lateral finger resistance on the solar cell performance was simulated by varying the busbar numbers. Here, the busbar numbers for the groups PTP 1 (w_f = 22 µm and 112 fingers), PTP 3 (w_f = 18 µm and 126 fingers) and PTP 4 (w_f = 20 µm and 126 fingers) were varied between 3 to 18 busbars. The exact total busbar shading area for different busbar numbers was kept to neglect the influence of other parameters on the J_{sc} and V_{oc}.

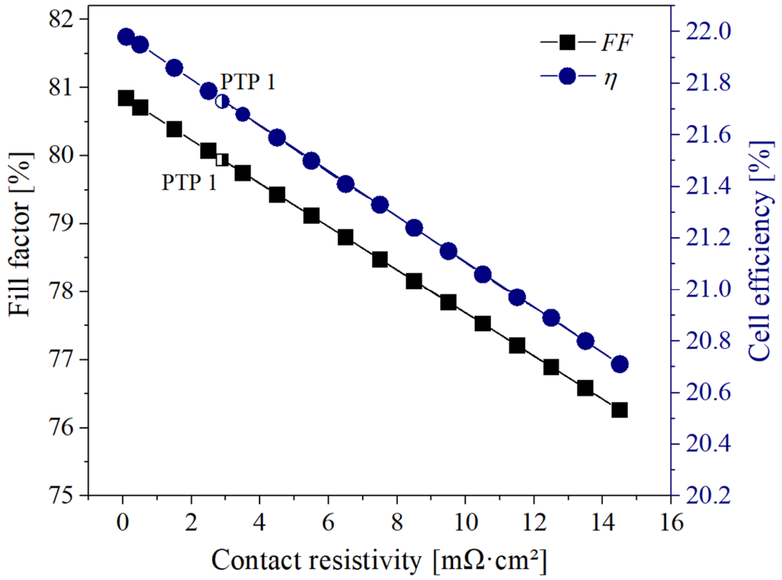

Figure 5.7: Influence of contact resistivity on the *FF* (black squares) and conversion cell efficiency η (blue circles) simulated with Griddler 2.5 Pro [72].

Figure 5.8 shows the effect of the busbar number on *FF* and cell efficiency using the simulation software Griddler 2.5 Pro. The grey dashed lines represent the *FF* and the cell efficiency of the best screen-printed reference cell with a six-busbar layout. Increasing the number of busbars from

6 to 12 reduces the contribution of the lateral finger resistance to the total series resistance by a factor of four. Therefore, the *FF* and cell efficiency for PTP groups are increased by 0.4% and $0.12\%_{abs}$, respectively. A further increase of the busbar number from 12 to 18 would enhance the *FF* by additional 0.12%. For PTP 3 to achieve a similar efficiency as the reference, 18 busbars would be required and for PTP 4 with a finger width of 20 µm, an upgrade from six to nine busbars is necessary.

These simulation results confirm that the six-busbar layout limits the full potential of PTP fingers. Narrow fingers on solar cells can be fully utilized with a higher number of busbars to mitigate the loss from lateral finger resistance. Therefore, many PV manufactures have started to upgrade the busbar number from six busbars to nine busbars, twelve busbars or busbarless cells with a multi-busbar interconnection [16]. However, increasing the number of busbars from six to 18 busbars without any loss due to the optical shading is still quite challenging with the current soldering technology. Therefore, the further development of cell interconnection for the current soldering technology is required for this increase in busbar number. Alternative technologies than the standard string-ribbons interconnection [131], [132] have been already available, such as solder-coated round copper wires on the busbars interconnected using infrared light [133], [134] and thin round copper wires that are embedded in a polymer film called smart wire connection technology (SWCT) [135], [136].

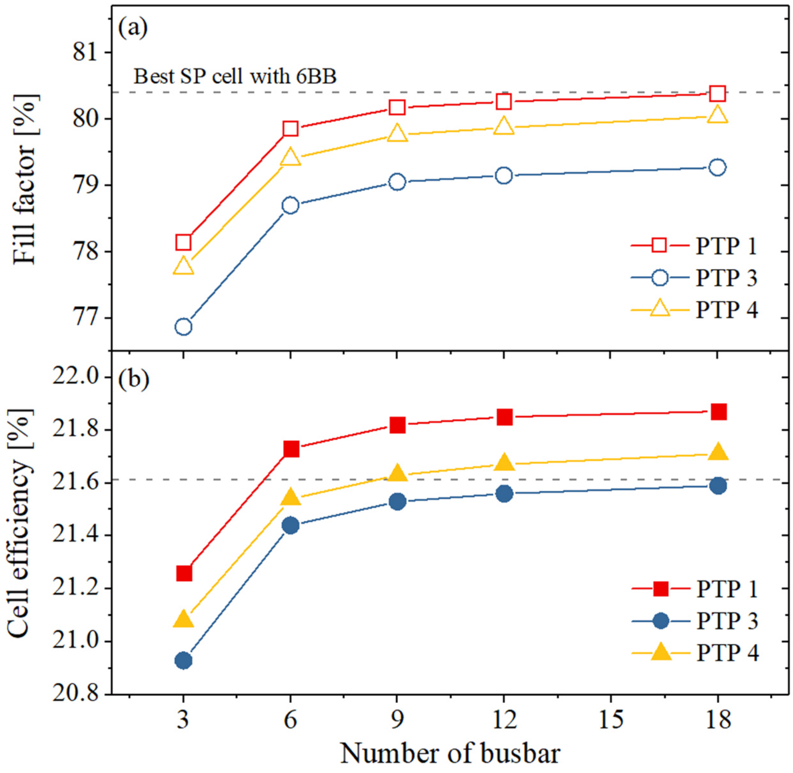

Figure 5.8: Influence of the number of busbar on the cell *I-V* parameters simulated with Griddler 2.5 Pro [72]: (a) *FF*; (b) cell efficiency. The dashed lines represent the values obtained from the best cells of the screen-printed reference and the solid lines serves as a guide to the eye.

Using the cell parameters from the best cell of PTP 1 as input parameters, the dependence of cell efficiency on finger width and finger number with a six-busbar cell layout was simulated using a cell simulation software Gridmaster [137], and the results are displayed in Figure 5.9. The best cell from PTP 1 had a cell efficiency of 21.73% from 112 fingers with a width of 22 µm. By keeping the finger width of 22 µm, a higher cell efficiency of PTP 1 can be increased to 21.77% using a higher finger number of 139 fingers. The J_{sc} and V_{oc} are slightly reduced due to an increase in the finger metal fraction of Ag fingers from 1.5% to 2%, but the *FF* is increased from 79.9% to 80.51% due to lower total series resistance. However, the increase in finger number from 112 to 139 fingers increases the total silver paste consumption by 7.6 mg (24% higher from 112 fingers). A lower finger width with the same aspect ratio as PTP 1 requires a higher finger number to maintain the series resistance at the same level. This will not only lead to a higher cell efficiency but also a higher silver paste consumption. A compromise between J_{sc} and *FF,* as well as a production cost, are necessary for designing an optimum finger grid layout.

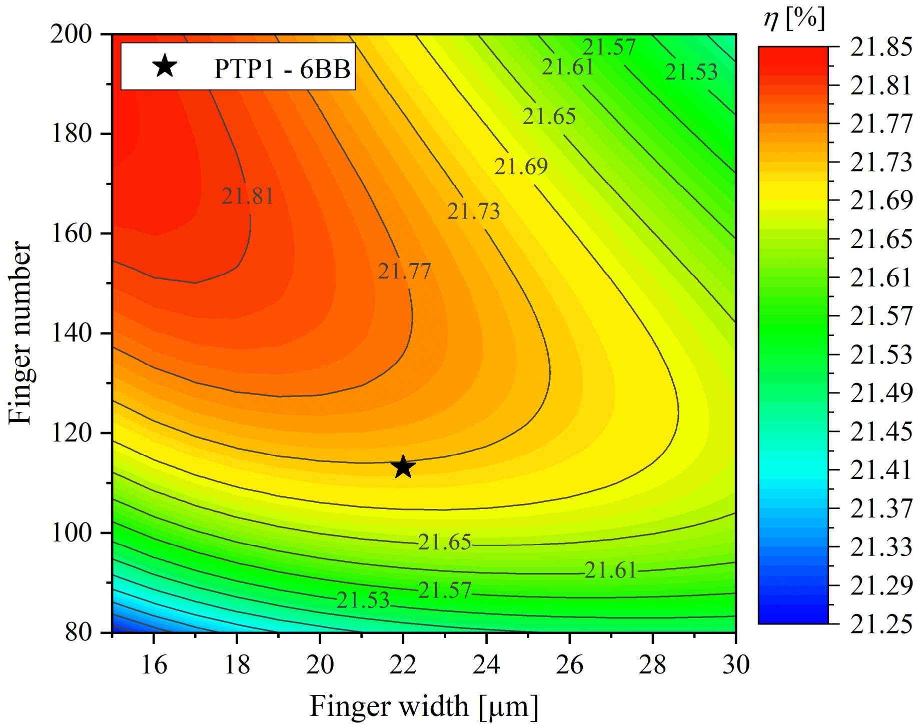

Figure 5.9: Two-dimensional contour map of cell efficiency in dependency of finger width and finger number for a six busbars cell layout with a fix finger aspect ratio of 0.55 simulated using Gridmaster. The input parameters were taken from the best cell parameter from PTP 1. The black star is the best efficiency value of PTP 1 with an average finger width of 22 µm and 112 fingers.

5.4 Current status of screen-printing technology

In the previous section, the screen made by manufacturer Murakami Co., Ltd. with 440 meshes per inch, wire diameter of 13 µm and mesh angle of 22.5° was chosen as the screen-printing reference group as it fabricates a similar finger width as the average industrial finger width of 39 µm [16]. The combination of these screen specifications and a screen opening of 28 µm results in a total open area (*OA*) of 64.6% within the screen opening, as shown in Figure 5.10(a). The open area defines the area without the emulsion in the screen aperture region, where the paste is transferred through the mesh onto a substrate during the squeegee process. The higher the open area of a screen, the more homogenous the screen-printed finger will be. By converting the CLSM images of the screen to a binary image, the open area is calculated by dividing the total area available for the paste transfer, which is not blocked with knots and wires, with the total aperture area. In this section, the current limit of screen-printing technology on the research level is investigated. The screen aperture is reduced to deposit narrow fingers similar to PTP technology. However, a further reduction of the screen opening to fabricate an even thinner finger will decrease the open area inside the screen aperture, which leads to a difficult squeegee process resulting in inhomogeneous fingers or even in the worst-case scenario line interruptions.

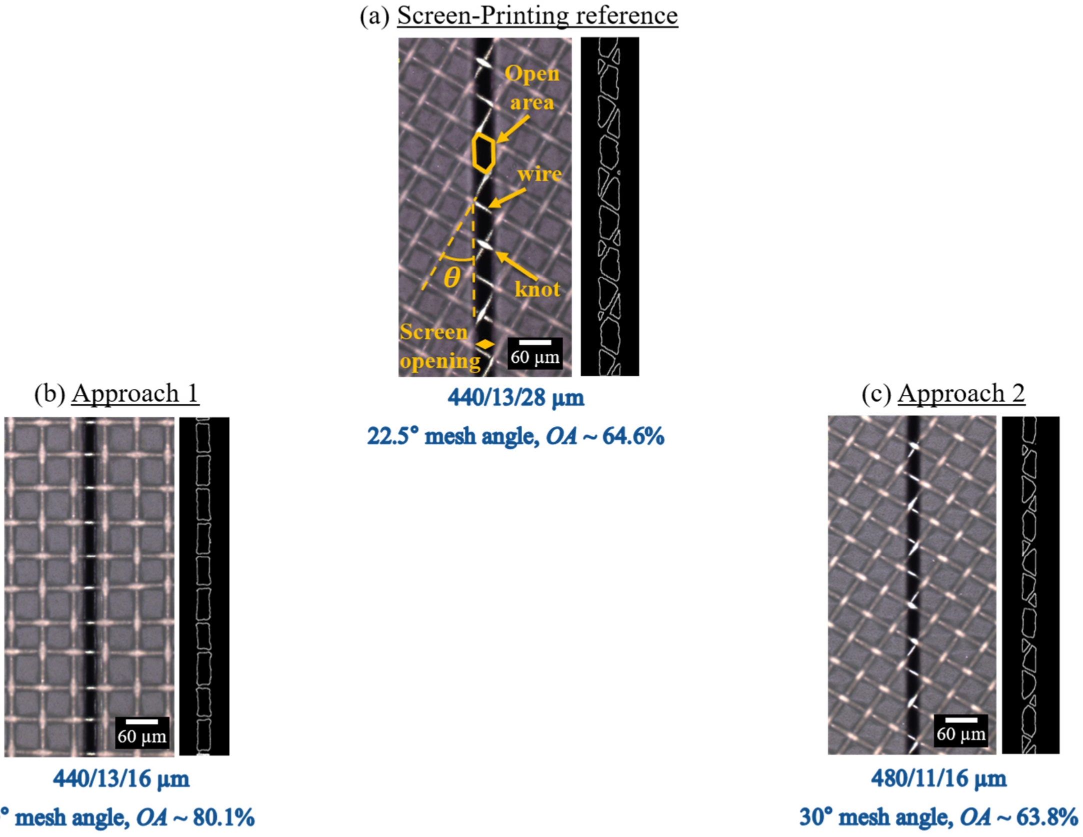
(a) Screen-Printing reference

440/13/28 µm

22.5° mesh angle, *OA* ~ 64.6%

(b) Approach 1

440/13/16 µm

0° mesh angle, *OA* ~ 80.1%

(c) Approach 2

480/11/16 µm

30° mesh angle, *OA* ~ 63.8%

Figure 5.10: Microscope top-view images of current screen-printing reference screen and two possible development routes to achieve a narrower finger: (a) screen-printing reference with a screen opening of 28 µm, which represents the state-of-the-art industrial screen; (b) the first approach for a smaller screen opening of 16 µm by applying the 0° mesh angle, which results in an increase of the open area to 80.1% within the screen opening; (c) the second approach to design a screen with a smaller screen opening of 16 µm by using a smaller wire diameter of 11 µm, which keeps the open area around 63.8% as the SP reference although the higher number of knots due to its higher mesh counts of 480 meshes per inch. The images were taken using CLSM at 50× magnification. The smaller images on the right side are the binary images of the CLSM images, which are used to calculate the open area inside the screen aperture using image processing software ImageJ.

Here, the two approaches to design a mesh screen with a smaller screen aperture are introduced. The first approach is the “knotless (or zero-degree mesh)” screen, in which the mesh angle of the screen is modified from the industry-standard angle of 22.5° [33], [34] to 0°. The zero-degree angle of the wires allows the knots to be located outside the screen opening region. It enlarges the open area further because the screen aperture region is blocked only with wires, as depicted in Figure 5.10(b). Therefore, the knotless screen improves the paste transfer and minimizes the mesh mark effect on the fingers. Using the same screen specifications as the SP reference screen, such as 440 meshes per inch and wire diameter of 13 µm, an opened area of 80.1% is achieved by changing the mesh angle to 0°.

However, the knotless screens have some disadvantages over the standard 22.5° angle mesh screen, which are a lower screen lifetime, the inflexibility to design the screen parameters, precise alignment of the finger pattern in regard to the mesh, which is associated with a higher manufacturing cost [138], [139]. The second approach is by using a screen with a smaller wire diameter. The mesh angle is slightly changed from 22.5° to 30° since the 30° provides less area with knots inside the screen opening for smaller screen aperture [34]. The mesh count is increased from 440 to 480 meshes per inch to allow sufficient screen tension. Using the smallest wire diameter available on the market (d_{wire} = 11 µm), a similar open area of around 64% as the SP reference screen is achieved within the screen aperture of 16 µm, as depicted in Figure 5.10(c). The print quality of these two different approaches is studied here and compared with the industrial-standard SP reference screen. The finger geometry as well as the homogeneity of the fingers are analyzed and their effects on the *I*-*V* parameters are investigated.

5.4.1 Experimental details

In this experiment, two different approaches are compared with the state-of-the-art industrial screen for the front side metallization of solar cells, which is used as a reference in section 5.1. Table 5.4 shows an overview of the screen specifications used in this experiment. A new commercially available Ag paste SOL9651B from the paste manufacturer Heraeus Precious Metals was used since the SP reference Ag paste SOL9641B was not available anymore on the market. This experiment includes two reference groups: a SP reference screen with a screen aperture of 28 µm and a reference group printed using PTP technology with trench design 1 and Ag paste E (best-known method of PTP from section 5.2).

Two different screen openings and two different screen specifications are investigated. To investigate the print quality for smaller screen aperture, the reduction of screen opening from the SP reference (screen opening of 28 µm) was divided into two levels; intermediate reduction (screen opening of 22 µm) and extreme reduction (screen opening of 16 µm). The knotless screen design with 440 meshes per inch, wire diameter of 13 µm and emulsion over mesh (EOM) of 12 µm had a screen opening of 22 µm (G2-A) and 16 µm (G3-A). The screen design with a mesh angle of 30° with 480 meshes per inch, wire diameter of 11 µm and EOM of 12 µm applied the same finger opening of 22 µm (G2-B) and 16 µm (G3-B). For G2 and G3, the same EOM thickness was chosen to neglect its influence during the flooding process. Thus, the paste transfer and finger geometries are affected mainly by the screen opening and the mesh angle of each screen configuration.

To minimize the effect of the finger cross-sectional area on the contact resistivity, the finger number for the smaller screen opening was optimized with simulation software Griddler 2.5 Pro [129]. The finger number for the screens with 22 µm opening was increased to 120 fingers and the screens with 16 µm opening were adjusted to have 135 fingers.

To evaluate the printability of the various screens with different specifications, industrial Cz-Si *p*-type PERC precursors local contact opening for Al-BSF formation from a pilot line of Hanwha Q Cells (Thalheim, Germany) were used. The front side of the precursors had a six-busbar layout. After the front metallization, all samples were dried using a Baccini paternoster drying oven at a peak temperature of 200 °C with 15 min cycles duration, and then sintered at a peak temperature of 890 °C and a belt speed of 7 $m \cdot min^{-1}$ using a Centrotherm fast-firing furnace. CLSM images at five different positions on three different cells for each group, as listed in Table 5.4, were taken by a CLSM LEXT OLS4000, and the finger geometries of each group were statistically analyzed using an image analysis software Mountains Technology Surface Texture Analysis Premium [102]. In addition to the typical finger geometries, such as finger height, finger width, finger aspect ratio and finger cross-sectional area, a height distribution profile of each group was generated to analyze the homogeneity of the printed fingers. The *I-V* parameters of the cells with six-busbar layout were measured using a xenon flash-type solar simulator. Additionally, the contact resistivity measurement was performed based on the transfer length method and the lateral finger resistance was measured using the four-point-contact measurement method.

Table 5.4: Various screen specifications and Ag pastes used in this experiment.

Group		Ag paste	Mesh angle [°]	Screen opening [µm]	Mesh count [/inch]	d_{wire} [µm]	EOM [µm]	Screen thickness [µm]	Finger number
G1-Ref	SP-28µm-22.5°	SOL9651B	22.5	28	440	13	15	37	112
G2A	SP-22µm-0°	SOL9651B	0	22	440	13	12	29	120
G2B	SP-22µm-30°	SOL9651B	30	22	480	11	12	28	120
G3A	SP-16µm-0°	SOL9651B	0	16	440	13	12	29	135
G3B	SP-16µm-30°	SOL9651B	30	16	480	11	12	28	135
G4-Ref	PTP-30µm-Ref	PTP paste E	-	-	-	-	-	-	112

5.4.2 Results and discussions

Figure 5.11 shows the finger height histogram and its normal distribution for the various screen parameters and the PTP reference group. The screen-printing reference group (G1-Ref) has a relatively broad distribution with an average finger width of 13 µm and finger height variation between 6 and 20 µm. Both screens with a mesh angle 30° of groups G2-B and G3-B have a narrower height distribution with a lower standard deviation than G1-Ref and an average finger height of 13 µm and 11 µm, respectively. The knotless screen proves to have a narrower distribution and a lower standard deviation among the other screen printing groups. Hence, the uniformity of the screen-printed fingers is much better using a zero-degree mesh screen. The finger height varied from 9 to 19 µm for G2-A and from 9 to 18 µm for G3-A. The reference group G4 obtained by PTP technology has the smallest finger height distribution in the range between 9 and 17 µm compared with the screen printing groups.

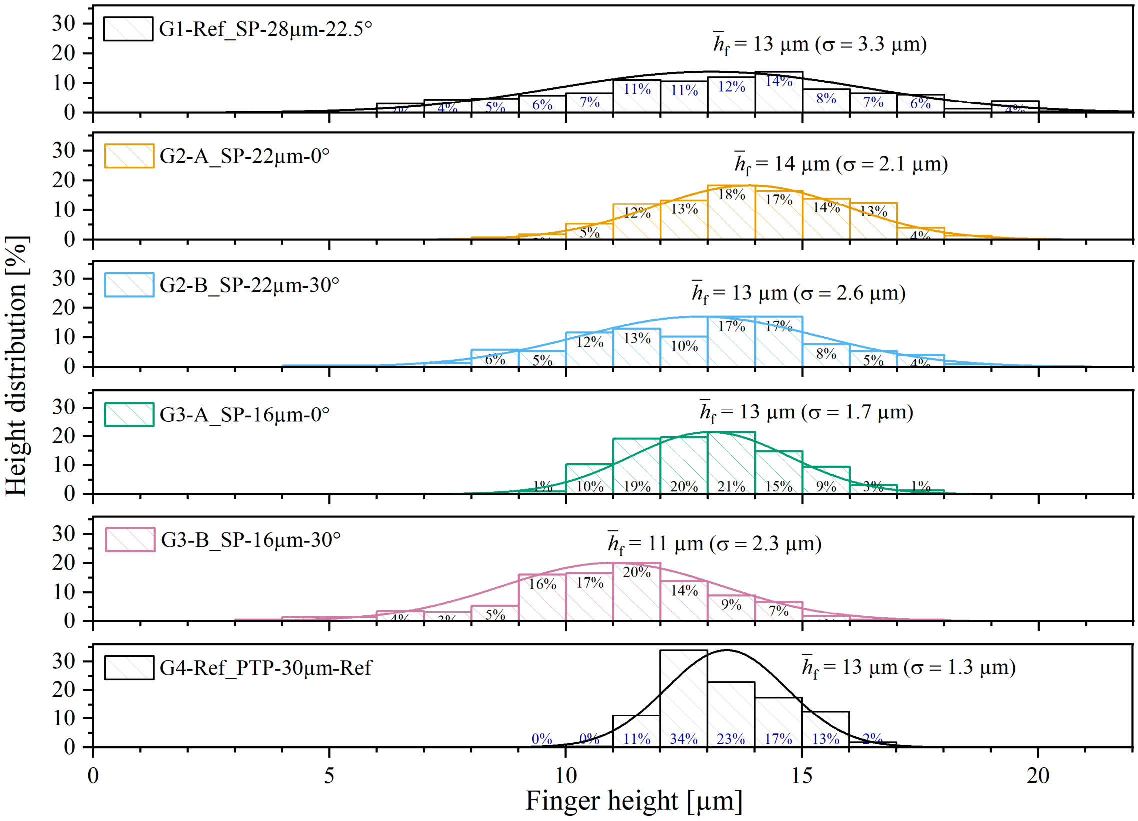

Figure 5.11: Finger height histogram and its normal distribution of various screen parameters and a PTP reference group. The average finger width and the standard deviation of each group are presented. Each height normal distribution curve from a total data of 224 values is measured using the image analysis software Mountains Technology. Each data value is the average finger height from a scanning area of 256 µm × 16 µm.

Figure 5.12(a) displays the finger width of each group. The SP reference screen fabricated fingers with a width of 39 ± 1.1 µm, similar to the finger width obtained from the previous sections 5.1 and 5.2. The screens with the same screen aperture have a similar finger width, although the screens with a mesh angle of 30° had slightly narrower fingers. The screens from groups G2-A and G2-B with the screen opening of 22 µm resulted in an average finger width of 29.6 µm and 29.2 µm, respectively. The knotless screen with the screen opening of 16 µm fabricated fingers with an average width of 22.1 µm and the screen with 30° mesh angle had an average finger width of 21.8 µm. The smallest finger width (w_f = 21 ± 1 µm) was achieved using PTP with Ag paste E and trench design 1. As shown in Figure 5.12(b), the finger cross-sectional area decreases toward the smaller screen opening, and the highest finger cross-sectional area of 410 µm^2 was achieved using 28 µm screen opening. For the screen openings of 22 and 16 µm, the zero-degree mesh angle exhibited a higher finger cross-sectional area than the screens with a mesh angle of 30° caused by a higher open area inside the screen aperture. Fingers with a cross-sectional area of

233 µm^2 were achieved by the PTP reference group and the screen-printed group with the screen opening of 16 µm and the mesh angle of 0°.

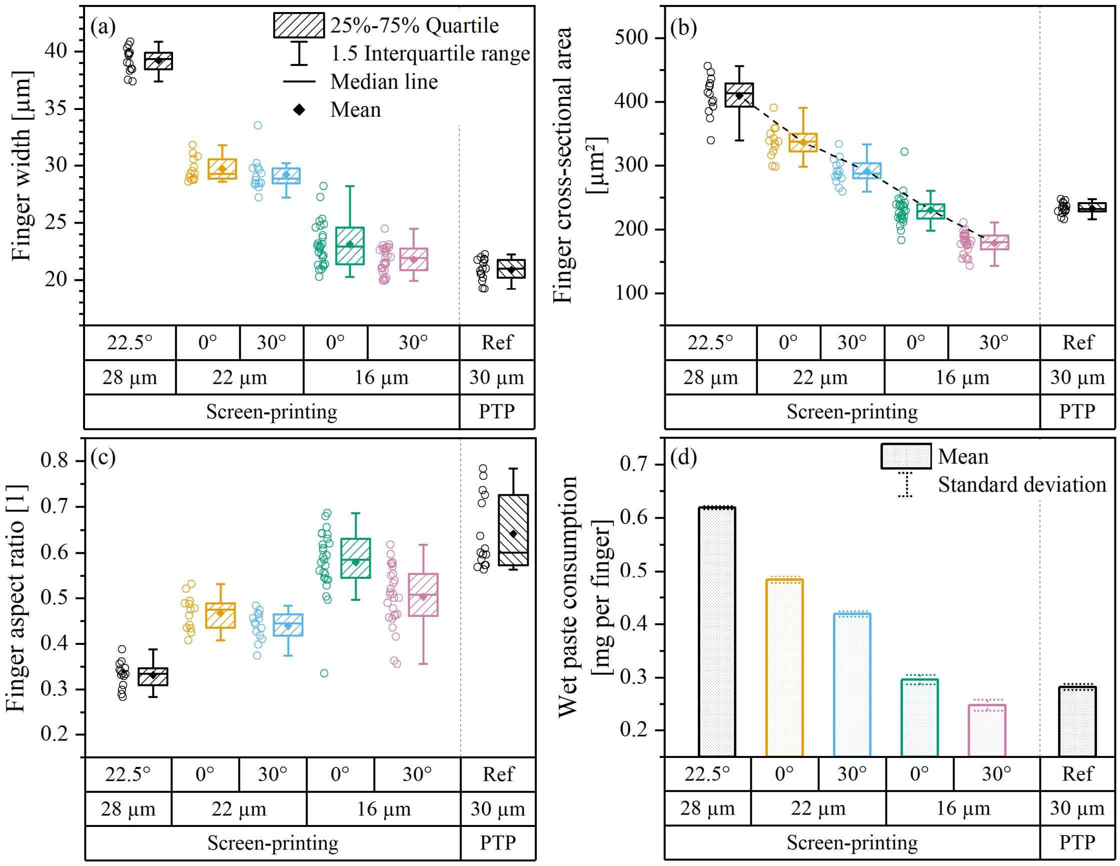

Figure 5.12: Finger geometries of various screen parameters and a PTP reference group analyzed using an image analysis software Mountains Technology as well as its wet paste laydown: (a) finger width; (b) finger cross-sectional area; (c) finger aspect ratio; (d) Ag paste laydown.

Figure 5.12(c) shows the finger aspect ratio of the printed fingers from all groups. The SP reference group achieved the lowest finger aspect ratio due to its widest finger, as the average finger height was similar to other groups. The fingers obtained by the knotless screens had a higher aspect ratio than the screen with a mesh angle of 30°. However, the highest aspect ratio was achieved by the PTP reference group ($AR = 0.64$). The advantage of the knotless screen is more apparent for a smaller screen opening. Figure 5.12(d) shows the wet Ag paste laydown from all groups, and it is proportional to the trend of the finger cross-sectional area. The lower the screen opening, the lower the wet paste laydown per contact finger. The same wet paste laydown was achieved for both reference groups compared with the experiment from the previous section, showing the reproducibility of both technologies. The screen-printing reference group used 0.62 mg per finger and the PTP reference group 0.28 mg per finger. By lowering the screen opening from 28 µm to 22 µm, the wet paste laydown for the screen with 0° and 30° mesh angle was reduced to 0.48 mg per finger and 0.42 mg per contact finger, respectively. Using a screen opening of 16 µm, a similar paste laydown as PTP reference group was achieved with the screen-printing group utilizing a screen with zero-degree mesh angle. The group with 16 µm screen opening and 30° mesh angle has an even lower paste laydown of 0.22 mg per contact finger. However, this smaller paste consumption was caused by an improper paste transfer, leading to finger interruptions and bad finger shapes.

The higher open area for the knotless screen facilitated a higher paste transfer than the open area of the standard mesh screen, minimizing the mesh marks and improving the finger uniformity, as shown in Figure 5.13. The mesh marks on the fingers with a mesh angle of 22.5° were distinctly observed and caused inhomogeneous fingers for SP reference group G1. The further reduction of screen opening reveals that the uniformity of the fingers improved for knotless screens leaving only minor mesh marks along the fingers. The screens with mesh angle of 30° and smaller wire diameter of 11 µm achieved fingers with a better homogeneity for a screen aperture of 22 µm than for a 16 µm screen aperture. This related to an unequal paste transfer along with the finger, resulting in less transfer or in the worst scenario no paste transfer in a particular area for the group using the screen aperture of 16 µm and may cause an increase in line resistance caused by inhomogeneous fingers or in the worst-case line interruption. The laser transfer process of PTP technology proved to be able to fabricate homogeneous fingers. The PTP reference group using trench design 1 accomplished uniform contact fingers for an even smaller finger width ($w_f = 21 \pm 1$ µm) than the knotless screen-opening group with a screen aperture of 16 µm ($w_f = 22 \pm 1$ µm), which was optimal for the front metallization of silicon solar cells.

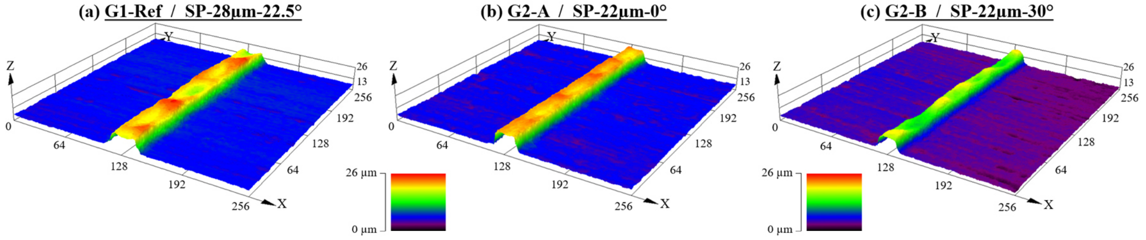
(a) G1-Ref / SP-28µm-22.5°
(b) G2-A / SP-22µm-0°
(c) G2-B / SP-22µm-30°

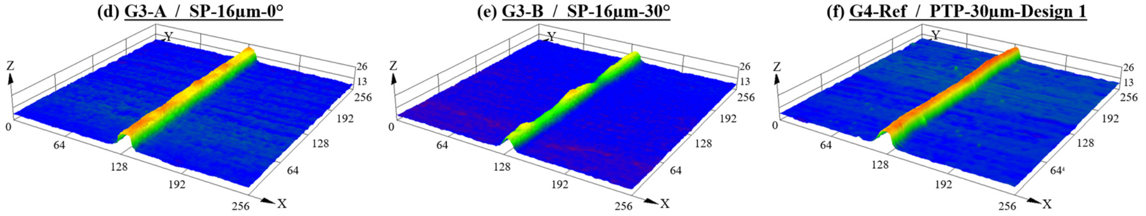
(d) G3-A / SP-16µm-0°
(e) G3-B / SP-16µm-30°
(f) G4-Ref / PTP-30µm-Design 1

Figure 5.13: Tilted top-view 3D-CLSM images of the printed fingers from five different screen specifications and one PTP reference group. These images serve as an overview of the print quality and the finger uniformity along the contact fingers of all groups. CLSM images were obtained at 50× magnification.

Figure 5.14 presents the *I-V* parameters of solar cells from all groups with a six-busbar layout. For the screen opening of 22 µm, there is no significant difference in J_{sc} values to be seen between the screens with zero-degree mesh angle and the screens with the mesh angle of 30°. Some of the cells printed with the screen with 16 µm opening suffered from severe finger interruptions over the whole area of the cells, as displayed in Figure 5.15. As a result, the generated current in these regions cannot be transported via a path of a low ohmic resistance to the contacts at the busbars. In EL images, these regions appear dark because also no current can be injected via the busbars.

Finger interruptions also caused the generated current maybe not transported to fingers and busbars, which explained the decrease in J_{sc}. The *FF* suffered from this finger line interruption due to a significant increase in series resistance induced by a longer electron transport length and the finger uniformity, especially for the screen with a mesh angle of 30°. Nevertheless, the best cell of group G3-A produced the highest J_{sc} value among the other screen printing groups.

Additionally, a minor increase of V_{oc} due to a smaller metal fraction of narrower finger width from screen-printing groups can be observed. The highest cell efficiency of 22.1% was achieved using a knotless screen with a screen aperture of 22 µm. On the other hand, the PTP reference group achieved a lower average cell efficiency (η = 21.8%). A significant gain of J_{sc} due to its narrowest finger width cannot overcome a higher loss in *FF* and V_{oc} value compared with screen-printing groups. The difference in V_{oc} is probably caused by the different paste composition between the Ag paste for screen-printing and Ag paste E for the PTP group, as from the covered area metal fraction, this group should have been the highest V_{oc}. The cell efficiency of PTP group is expected to be higher than the cell efficiency of the SP groups if the Ag paste SOL9651B is rheologically modified for PTP application resulting in the similar contact formation and at the same time utilizing the narrow fingers (w_f = 21 ± 1 µm) of PTP technology.

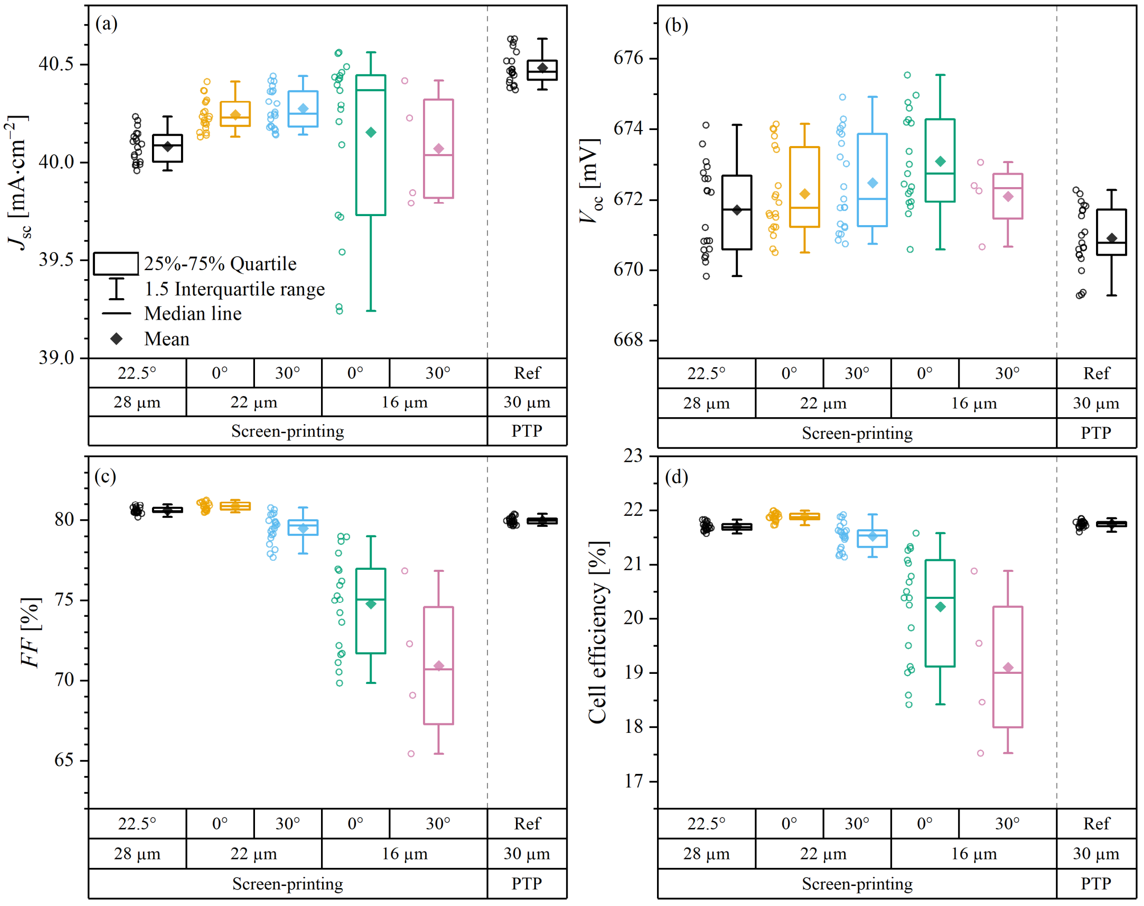

Figure 5.14: *I-V* measurements for five different screen parameters and one reference obtained by PTP technology under STC: (a) J_{sc}; (b) V_{oc}; (c) *FF*; (d) cell efficiency.

Figure 5.15 displays the electroluminescence (EL) images for all groups. The EL measurement device from GreatEyes is equipped only with a five-busbar connection, leaving the second busbars of the cell unconnected. The dark region found in EL images depicts the improperly contacted area caused by line interruptions. The reduction of screen aperture from 28 to 22 µm accomplishes a proper contact for all fingers either for a knotless screen or a screen with a mesh angle of 30°. For a further reduction of screen aperture to 16 µm, a significant amount of dark area was observed for both screen specifications. Two EL images for the group with a knotless screen and a screen with 30° mesh angle show the best cell and the worst cell from each group (see Figure 5.15(d) and (e)). The dark area was caused by unsuccessful paste transfer in the certain area, leading to non-proper contacts explaining the significant J_{sc} and FF loss of groups G3-A and G3-B of some cells. Further adjustment of the printing parameter and Ag paste modification may be necessary to improve the interruption problem and printability for both screens that might result in a better homogeneous finger shape with a lower height distribution. For the PTP group, there was no dark region observed, and hence, no improper contact finger observed in EL images display a good print quality and homogenous contacts for the cells with the smallest finger width ($w_f = 21 \pm 1$ µm) and finger cross-sectional area ($A_{finger} = 233$ µm^2) achieved by PTP technology.

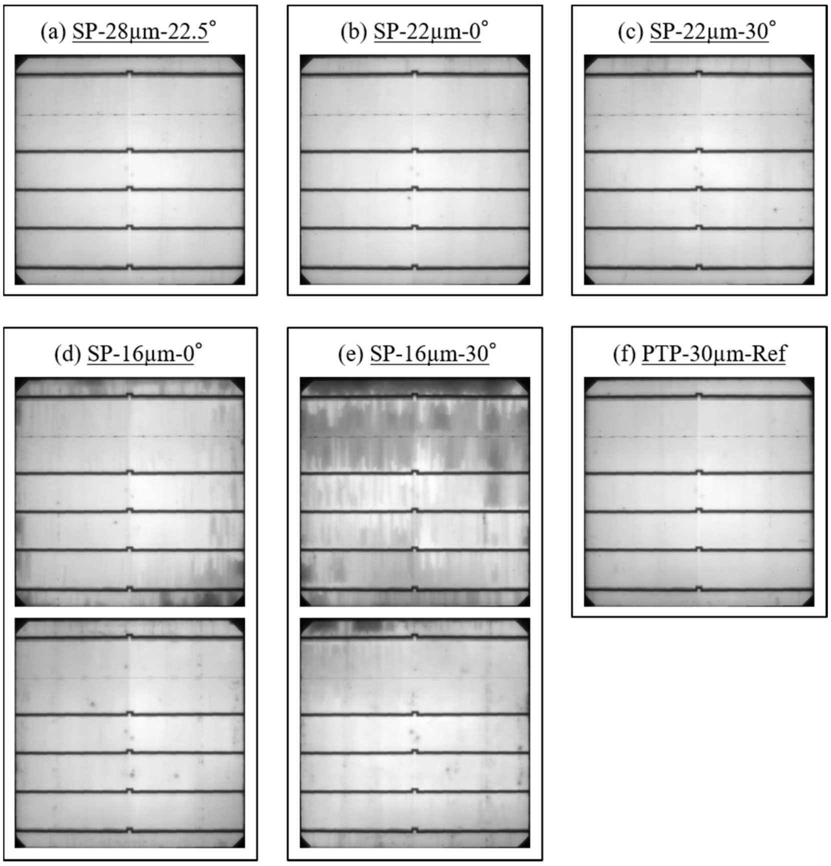
(a) SP-28µm-22.5°

(b) SP-22µm-0°

(c) SP-22µm-30°

(d) SP-16µm-0°

(e) SP-16µm-30°

(f) PTP-30µm-Ref

Figure 5.15: EL images obtained for five different screen-printing (SP) groups and a PTP reference group. The dark regions represent the position of the cell, which has an improper paste transfer caused by screen printability resulting in line interruptions for some cells. The EL measurement device from GreatEyes was equipped only with connection for five busbars, leaving the second busbars of each cell unconnected.

Figure 5.16 shows the contact resistivity values and the lateral finger resistance value from all groups. The finger contact resistivity for screen-printing groups can be controlled below 2 mΩ·cm^2 by applying a higher finger number for the smaller finger width. The Ag paste SOL9651B reduced the average contact resistivity of SP reference group G1-Ref to 1.3 ± 0.4 mΩ·cm^2. PTP finger still has the lowest contact resistivity among other SP groups. However, the contact resistivities of screen printing groups using a new generation Ag paste SOL9651B were improved and better than the previous results using the fine line Ag paste SOL9641B (see section 5.2 and 5.3). The contact resistivity results showed that the Ag paste development nowadays focuses on ultra-fine line printing and is more or less similar to the Ag pastes modified for PTP technology, which features a higher yield stress and a reduction of slumping and spreading. Hence, a direct comparison between the new generation of paste SOL9651B and PTP paste based on the old generation of SOL9641B is not straightforward.

The adjustment of organic vehicle and glass frit may help to establish a proper contact formation for the ultrafine line screen-printing. The contactless laser printing method of PTP offers greater flexibility to modify the rheological properties of Ag paste than the rheological adjustment of Ag pastes dedicated for screen-printing technology. The lateral finger resistance depends strongly on the cross-sectional area and the print quality. The lateral finger resistance increased from 0.6 Ω·cm^{-1} for screen opening of 28 μm to 1.5 Ω·cm^{-1} for the screen for screen opening of 16 μm with 0° mesh angle and to 2.4 Ω·cm^{-1} for the screen for screen opening of 16 μm with 30° mesh angle. The knotless screen exhibited a smaller line resistance than the screen with 30° mesh angle for the same screen aperture resulting from a better finger uniformity and higher finger cross-sectional area.

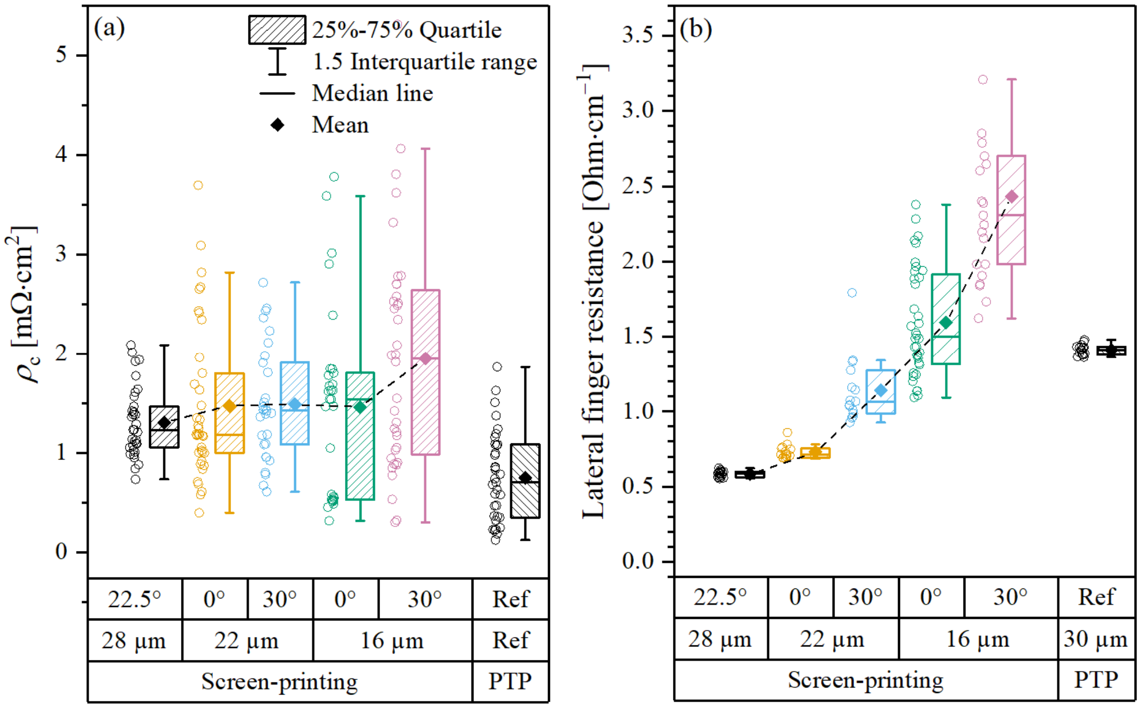

Figure 5.16: Series resistance measurements for five different screen parameters and one reference group obtained by PTP technology: (a) finger contact resistivity; (b) lateral finger line resistance.

The narrowest finger width of 22 µm with an aspect ratio of 0.6 was achieved in this study using Ag paste SOL9651B and a knotless screen with 440 meshes per inch, wire diameter of 13 µm, EOM of 15 µm and screen aperture of 16 µm. Tepner *et al.* reported an average finger width of 19 µm with an aspect ratio of 0.95, a lateral finger resistance between 1 and 3 $\Omega\cdot\text{cm}^{-1}$ and minor mesh marks using a knotless screen with 440 meshes per inch, wire diameter of 13 µm, EOM of 15 µm and screen aperture of 15 µm [34]. Therefore, it can be suspected that further optimization of printing parameters and adjustment of Ag paste might lead to better printing results for a smaller screen aperture.

5.5 Implementation and Challenge of PTP into PV metallization line

A standard metallization line for the production of PERC solar cells consists of three or four screen-printing steps. The first and the second screen printers are required for the back metallization, i.e., pads on specific cell areas for cell interconnection and Al printing on the area without pads, either as full area Al-print for monofacial PERC solar cells or a grid of Al fingers and busbars for bifacial PERC solar cells. Then, the cells are dried and flipped 180° to continue with the front metallization. There are three possibilities of front metallization using screen-printing technology, namely single print, dual print [140]–[142] and double print (or print-on-print) [126], [143]–[146]. In single print, fingers and busbars are printed in one step and with the same paste. This might lead to a higher metal fraction for the front metallization leads to a lower V_{oc} compared to other methods.

For the dual print metallization, the busbars are printed first utilizing the busbar paste with low laydown and reduced silver content. Then, the finger grid with Ag paste for ultrafine line printing with a high aspect ratio. Besides saving silver, the recombination in the busbar area can be reduced by using non-contacting Ag paste, which gives mechanical adhesions but does not completely destroy the passivation of the SiN_x layer. The double print process requires the busbars and the finger grid to be printed together, and then the second print of the finger grid on top of the first layer. The second print increases the finger height and simultaneously enhances the finger uniformity by minimizing mesh marks. Therefore, a higher aspect ratio and lower lateral finger resistance can be achieved. PTP technology showed its capability as an alternative for a contactless front metallization step to fabricate ultrafine line fingers with a higher aspect ratio than flatbed screen-printed references, as shown in section 5.2.

The implementation of PTP technology in the industrial PERC production line is relatively straightforward. The dual print metallization needs to be chosen, and the fourth screen-printing step is replaced by a PTP printer. Furthermore, the third drying step before the finger deposition of screen-printing can be skipped thanks to the contactless printing of PTP. Afterward, the wet Ag pastes for fingers and busbars can be dried together before the cells are transported to the fast-firing furnace for the sintering step. The PTP printer is designed in a way that it can easily fit into the production line due to a smaller dimension of 715 mm × 1770 mm × 1674 mm compared to a standard industrial screen printer. After the front metallization, metalized cells are dried and then sintered using a fast-firing furnace.

PTP technology proved its capability to significantly reduce the Ag paste consumption and fabricate ultrafine line fingers, resulting in a higher cell efficiency than screen-printing cells [70], [72]. However, PTP technology has not yet been applied in series production since its debut in 2015 [15]. To the best of author´s knowledge, only some pilot tests have been performed so far. Several issues might obstruct the implementation of PTP technology in an industrial production line for PERC solar cell performance: throughput, polymer recycling problem, and rapid development of screen-printing technology.

Throughput of metallization lines is an important topic in the PV industry because it is related to the production cost of solar cells. The higher the throughput, the lower the price of a solar cell. A standard screen-printer has a throughput between 3200 and 3600 wafers per hour [147], [148] and a current PTP pilot machine 1800i at the ISC Konstanz has a throughput of 3000 wafers per hour. By applying the PTP technology in an industrial PV production line, the throughput of the first, the second and third screen-printers for other metallization steps needs to be reduced to 3000 wafers per hour to accommodate the lower throughput of a PTP machine. Slightly higher production costs due to lower throughput may reduce the attractiveness of PTP technology for lowering wet paste laydown for finger metallization by 54-74% when compared to screen-printed references [72].

Recycling of polymer film might be an issue as well. A polymer film of size 202 mm length and 200 mm wide with a thickness of 200 µm is required to metalize nine solar cells with 112 fingers. As the number of fingers per section is fixed, a different line count would result in a different number of cells per section. Assuming a standard PERC industrial production output of nearly 75000 cells per day, it will produce around 0.673 m^3 polymer film per day by using PTP technology (equivalent to 90 kg APET waste per one day or 30 ton APET waste per year). Until now, already used polymer film cannot be reused for the next printing steps. This recycling problem is a bit contradictory since PTP technology wants to accelerate the growth of renewable energy by lowering the production cost and increasing cell efficiency but simultaneously creating a significant amount of polymer waste.

Rapid development of screen-printing technology might be the most substantial hindrance for implementing the PTP technology into the PV production line. Figure 5.17 shows the finger width reduction trend for the front metallization of crystalline silicon solar cells on the industrial level since 2009. In addition, the average finger widths with a single print process and mesh screens from various studies are displayed as the achievable reported finger width on the research level. The PTP showed a promising result as an alternative technology for front metallization due to the performance to fabricate narrow fingers [15], [70], [72]. This significant gap with the screen-printing technology has been reduced thanks to the rapid and steady development of paste and screen technology. The screen-printing performance on the research level to fabricate fingers with a width below 20 µm has already been proved [34], [149]. A similar average finger width was also obtained with PTP technology [72]. Although the gap with the average industrial finger width is still substantial, these promising results of screen-printing technology on the research level could deter the implementation of PTP technology in the mass production of PV industries because it may not necessary to invest in a new technology just yet. Further improvement to fabricate even narrower fingers might improve the chance of PTP technology to enter the PV mass production lines.

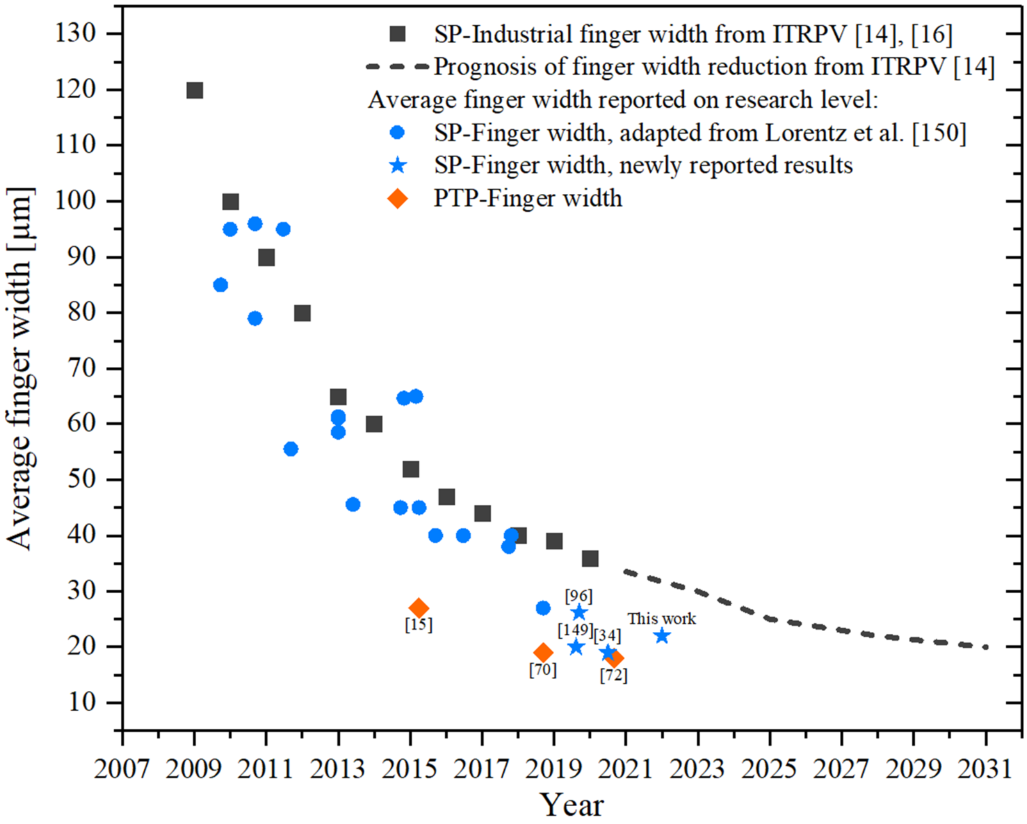

Figure 5.17: Development of finger width reduction for the front metallization of silicon solar cells since 2009 on the industrial and research level. The average finger width from each year at the industrial level is obtained from ITRPV 11th [16] and 12th edition [14]. The dashed line represents the prognosis of the width reduction on the industrial level for the next ten years, according to [14]. On the research level, the best average finger width single printed with mesh screens from various studies are shown in symbols with blue color; the blue circles are the data up to 2018, partially adapted from Lorenz *et al.* [150]; the reported finger width from recent studies starting from 2018 [34], [96], [149] are symbolized with blue stars. Additionally, the achieved finger width using PTP technology from published results [15], [70], [72] are displayed.

5.6 Chapter summary

In this chapter, the PTP technology for the application of front metallization of PERC solar cells was assessed, and its performance was compared with the reference group screen-printed with the state-of-the-art industrial mesh screen. To find the best screen parameters for the SP reference, three state-of-the-art industrial mesh screens from different screen manufacturers were analyzed. Average finger width of 38 µm with an aspect ratio of 0.37 was obtained by using the industrial screen with 440 meshes per inch, wire diameter of 13 µm, EOM of 15 µm and screen aperture of 28 µm. This finger width is in agreement with the finger width achieved in the industrial mass production [16] and hence this screen parameter was chosen as the reference from screen-printing technology.

Four different trench geometries from the same polymer film material were investigated. The geometry of the metalized fingers and its effect on the *I-V* performance of PERC solar cells with a six-busbar layout were observed. PTP 1 with the trapezoidal trench geometry and 30 µm bottom opening (trench design 1) achieved an average finger width of 22 µm with an aspect ratio of 0.55, resulting in the best cell efficiency among other PTP groups of 21.73%, which is $0.12\%_{\text{abs}}$ higher than the best screen-printed cell and. At the same time, the wet paste consumption using trench design 1 with 112 fingers was reduced by 54% compared with the Ag paste consumption for the SP reference. The narrowest finger of PTP groups was accomplished with PTP 3. A layout with126 fingers with a finger width of 18 µm and an aspect ratio of 0.51 resulted in J_{sc} gain of 0.45 $\text{mA}\cdot\text{cm}^{-2}$ compared to the SP reference. Still, the increase in series resistance caused by a lower finger cross-sectional area impeded the conversion efficiency of the best cell from PTP 3 to be only 21.44%. Nevertheless, Ag paste consumption could be reduced by 74% for 126 fingers metallization using PTP trench design 3.

The series resistance analysis showed that for the PTP-printed fingers with a cross-sectional area of 200 μm^2, the contact resistivity was lower than for the screen-printed fingers with a finger cross-sectional area of 400 μm^2. The Ag pastes for PTP technology are already suited to metalize ultrafine fingers, and this furthermore proves that the contact resistivity is not the limiting factor when going to the finger cross-sectional areas as small as 200 μm^2. However, for the finger cross-sectional areas smaller than 200 μm^2, the contact resistivity as well as the lateral finger resistance are currently the limiting factors, which compromise the J_{sc} and V_{oc} gain by a significant *FF* loss.

The simulation results showed that the current six-busbar layout limits the efficiency potential of ultrafine fingers of PTP. By doubling the number of busbars from six to twelve and maintaining the total busbar shading area, the contribution of the lateral finger resistance could be reduced by a factor of four. Thus, the *FF* can be increased significantly, and a higher cell efficiency than SP reference can be achieved. For a current cell layout with six busbars, an even higher cell efficiency of 21.77% can be achieved with an increase in finger number from 112 to 139 fingers, but at the same time, the paste consumption increases by 24%. Hence, a compromise between J_{sc} gain and *FF* loss, as well as paste consumption, needs to be considered before designing the metal grid using PTP technology.

For screen-printing technology, two methods to improve the printability for a smaller screen aperture were investigated; knotless screen (or zero-degree mesh screen) creating a higher open area inside the screen aperture and the reduction of wire diameter to maintain a similar open area as the standard industrial mesh screen. The knotless screen improves the homogeneity of printed fingers significantly and minor mesh marks were detected. Although the screen aperture was decreased aggressively from 28 to 16 µm, the reduction of wire diameter from 13 to 11 µm preserved the same open area. However, it was still inadequate for a good paste transfer creating inhomogeneous fingers and in worst case finger interruption. The PTP reference group using trench design 1 resulted in more uniform contact fingers of the smallest width of 21 ± 1 µm. Using the zero mesh degree screen with 440 meshes per inch, a wire diameter of 13 µm, a screen aperture of

16 µm and EOM of 15 µm, a similar finger width of 22 ± 1 µm with an aspect ratio of 0.6 was achieved.

The new paste SOL9651B resulted in a better contact formation than the precious Ag paste SOL9641B used for SP reference. Therefore, the cell efficiency of the SP groups was slightly higher than the PTP group, which was printed with a paste that is a rheologically modified version from the old paste specification of SOL9641B. For the screen aperture of 16 µm, the zero mess degree screen accomplished a better paste transfer resulting in a higher cell efficiency than 30° mesh screen. However, even the knotless screen still had the printing problem creating interruption on some cells. To solve this printability problem, another adjustment of printing parameters and Ag paste might be necessary.

6 Impact of Sheet Resistance and Paste Volume on Contact Resistance

The sheet resistance and the doping profile of the emitter affect the emitter saturation current of PERC solar cells. This chapter studies the effect of homogeneous emitter profiles with different sheet resistances on cell efficiency and contact formation of PERC structure. Further, the influence of paste volume of two different Ag pastes on the contact formation is investigated. Additionally, two front metallization approaches, namely firing with busbars and firing without busbars, are introduced to examine their effect on the contact formation of PERC solar cells.

6.1 Influence of sheet resistance on contact resistance

In this section, the effect of emitter sheet resistance of PERC solar cells on cell efficiency and contact formation is investigated. For this purpose, three different surface doping profiles with different depth are generated by varying the parameters of $POCl_3$ diffusion, creating homogeneous emitters with sheet resistances ranging from 70 to 120 Ω/sq. Finally, the advantage and challenges of a higher emitter sheet resistance for PERC solar cells are discussed.

6.1.1 Experimental details

For this experiment, PERC precursors with three different phosphorous doping profiles for the n^+-emitter layer were processed using the *Centaurus* processing route with SiO_x passivation on the rear [21], [151], [152]. At first, the *p*-type boron-doped Czochralski-grown Si wafers with an area of 244.32 cm^2, a thickness of 180 µm and base resistivity of 1.6 Ω·cm were etched around 8 µm for each side in an alkaline solution to remove the saw damage and subsequently cleaned. The rear dielectric passivation layer stack of SiO_x/SiN_y was deposited by plasma-enhanced chemical vapor deposition (PECVD), thereby acting as a diffusion mask and a capping layer to protect the rear side against etching. Then, the front surface was textured in an alkaline solution and a homogeneously-doped *n*-layer was achieved via in-diffusion of phosphorous atoms from phosphosilicate glass (PSG) in a quartz tube with $POCl_3$ atmosphere, creating the *p-n* junction. The different phosphorous doping profiles of the *n*-layer as measured with the electrochemical capacitance-voltage (ECV) method are shown in Figure 6.1. The first profile had the highest dopant surface concentration of approximately $2 \cdot 10^{20}$ cm^{-3}, a junction depth of 0.48 µm and an emitter sheet resistance of 70 Ω/sq. The second doping profile had a lower surface doping concentration of $8 \cdot 10^{19}$ cm^{-3} and a junction depth of 0.42 µm, resulting in a higher sheet resistance of 90 Ω/sq.

The third profile had an even lower dopant surface concentration of $1.5 \cdot 10^{19}$ cm^{-3}, a junction depth of 0.46 µm and a sheet resistance of 120 Ω/sq.

The phosphorous glass on the front side was removed in a diluted hydrofluoric acid (HF). Then, SiN_x layers by PECVD process were deposited on the front side, creating a passivation layer and anti-reflection coating. With "green" laser pulses in the nanosecond range of a frequency-doubled Nd:YAG laser, local contact openings were formed on the rear of SiO_2/SiN_x layer. A full area rear metallization was screen-printed with a commercially available Al paste and then dried. After that, on the front side six busbars were screen-printed using Ag paste followed by a drying step. The metallization of 112 fingers was performed using PTP technology with a trench design 1 (see Figure 2.6) and Ag paste F (see Table 4.1). After drying, all samples were sintered with a fast-firing belt furnace at a peak temperature of 840 °C and a belt speed of 5.4 $m \cdot min^{-1}$. The finger geometry was analyzed with a confocal laser scanning microscope and an image analysis software Mountains Technology Surface Texture Analysis Premium [102]. *I-V* measurements were conducted under STC with a xenon flash-type solar simulator. Several cells from each group were cleaved using laser scribing and then broken by hand into several strips to measure the contact resistivity via transfer length method (TLM) and lateral finger resistance with four-point measurement method. The external quantum efficiency for the three different groups was measured with a spectral response measurement system from pv-tools GmbH.

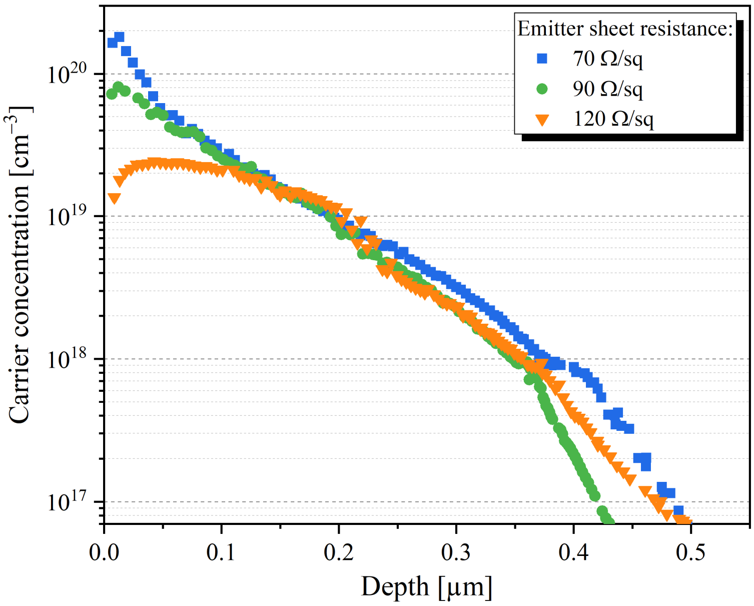

Figure 6.1: Three different phosphorous doing profiles of the *n*-type layer analyzed with ECV measurement method after the $POCl_3$ diffusion.

6.1.2 Results and discussions

The CLSM analysis of the fingers printed on the cells with different emitter sheet resistance, as shown in Figure 6.2, indicates that the finger geometries are not affected by the emitter sheet resistance. Average geometric values of all groups are quite similar: finger width of 26.4 µm with an aspect ratio of 0.41 and a finger cross-sectional area of 227 µm^2. Figure 6.2(d) shows that the lowest contact resistivity was acquired by the cells with the lowest emitter sheet resistance of 70 Ω/sq. A raise in the emitter sheet resistance increased the contact resistivity further. The contact resistivity value for the group with 120 Ω/sq fluctuated between 8 and 100 mΩ·cm^2. This enormous variation might be caused by a non-uniform emitter generating a high contact resistance at local points over the cells. A high emitter sheet resistance is renowned for its contacting problem between metal finger lines with silicon. To improve this contact resistance for a high emitter sheet resistance, several developments might be required, such as applying a higher number of fingers [153], improving the $POCl_3$ diffusion parameter to achieve a more homogeneous sheet resistance over the cell area, further adjustment of Ag paste [154], or the application of selective emitter creating a heavily doped n^+-layer under the contact fingers [155]–[157].

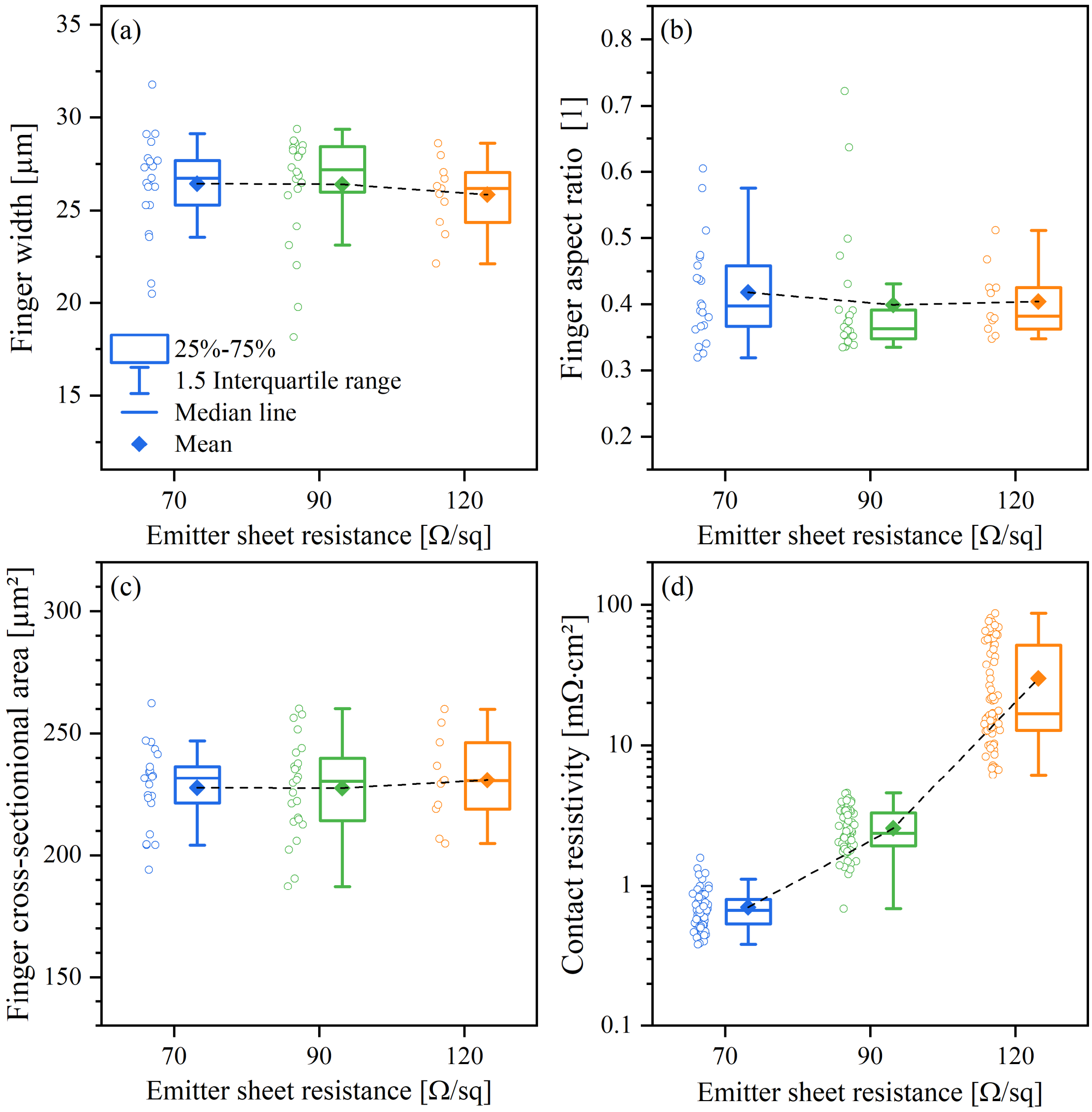

Figure 6.2: Finger geometries and contact resistivity from three different emitter sheet resistances: (a) finger width; (b) finger aspect ratio; (c) finger cross-sectional area; (d) contact resistivity.

The *I*-*V* results presented in Figure 6.3 reveal that V_{oc} values are improved with increasing emitter sheet resistance caused by a decrease in the emitter saturation current density [158], [159]. A V_{oc} gain of approximately 2 mV was achieved by increasing the emitter sheet resistance from 70 to 120 Ω/sq. An increase of sheet resistance from 70 to 90 Ω/sq resulted in a J_{sc} gain caused by the improvement of spectral response in the low wavelength regime, as shown in Figure 6.4. The further increase in sheet resistance to 120 Ω/sq should in principle enhance the J_{sc} gain further in the form of an even better improvement of external quantum efficiency (EQE) in the low wavelength region. Unfortunately, a too-thick ARC layer shifted the lowest reflection to a higher wavelength region and caused a higher reflection for the wavelength below 600 nm. Thus, the group with 120 Ω/sq has a poor light absorption in this wavelength region (see Figure 6.4), resulting in a significant drop in J_{sc}. From the loss calculation using EQE and reflection value, a higher reflection of the group with 120 Ω/sq contributed to a higher J_{sc} loss by 0.74 mA·cm^{-2} than the J_{sc} of the group with 90 Ω/sq. According to this calculation, with an optimum ARC layer thickness (similar reflection loss as 90 Ω/sq), a potential J_{sc} value of 39.32 mA·cm^{-2} can be achieved.

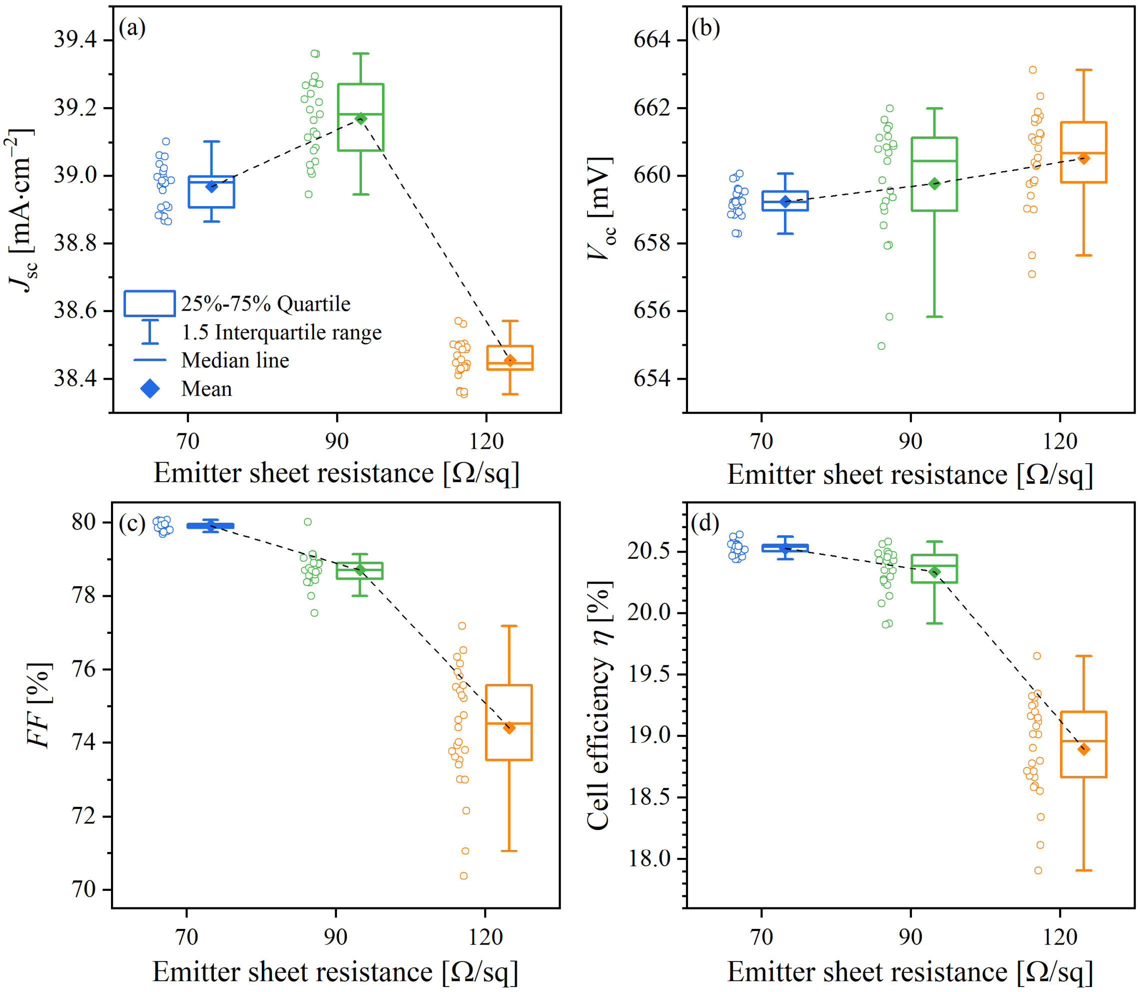

Figure 6.3: *I*-*V* results from three groups with various emitter sheet resistance measured according to STC: (a) J_{sc}; (b) V_{oc}; (c) *FF*; (d) cell efficiency η.

The total series resistance of a solar cell contributes to the *FF*. An increase of emitter sheet resistance affects the total series resistance generating a higher power loss in the emitter region $P_{\text{loss,emitter}}$, as shown in the following equation [107]:

$$P_{loss,emitter} = \frac{1}{3} \cdot J_{\text{MPP}}^2 \cdot s^2 \cdot R_{\text{Emitter}}. \tag{6.1}$$

where J_{MPP} is the generated current density at MPP, s is the distance between two fingers and R_{Emitter} is the emitter sheet resistance. A higher contact resistivity for the cells with a higher emitter sheet resistance also contributes to a higher total series resistance of a solar cell. Therefore, the *FF* decreases for groups with a higher emitter sheet resistance quite significantly.

From equation (6.1), the power loss in the emitter region $P_{\text{loss,emitter}}$ due to a high sheet resistance can be reduced by reducing the finger to finger distance (finger pitch). Thus, ultrafine Ag finger lines are required for a high emitter sheet resistance to reduce the distance between fingers by increasing the finger number without limiting J_{sc} due to a higher shading loss. Jeong *et al*. simulated the effect of finger number and aspect ratio for different emitter sheet resistance for a PERC structure, and they came to a similar conclusion that a higher sheet resistance requires a higher finger number and narrow fingers to achieve a higher cell efficiency due to lower total series resistance [153].

The highest cell efficiency was achieved by solar cells with an emitter sheet resistance of 70 Ω/sq. The J_{sc} and V_{oc} gain of the group with 90 Ω/sq was compromised with a significant *FF* loss resulting in a lower cell efficiency than the group with an emitter sheet resistance of 70 Ω/sq. The group with an emitter sheet resistance of 120 Ω/sq requires further developments to resolve the inhomogeneous emitter, a too thick ARC layer and contacting problem between Ag fingers and silicon to achieve a higher cell efficiency.

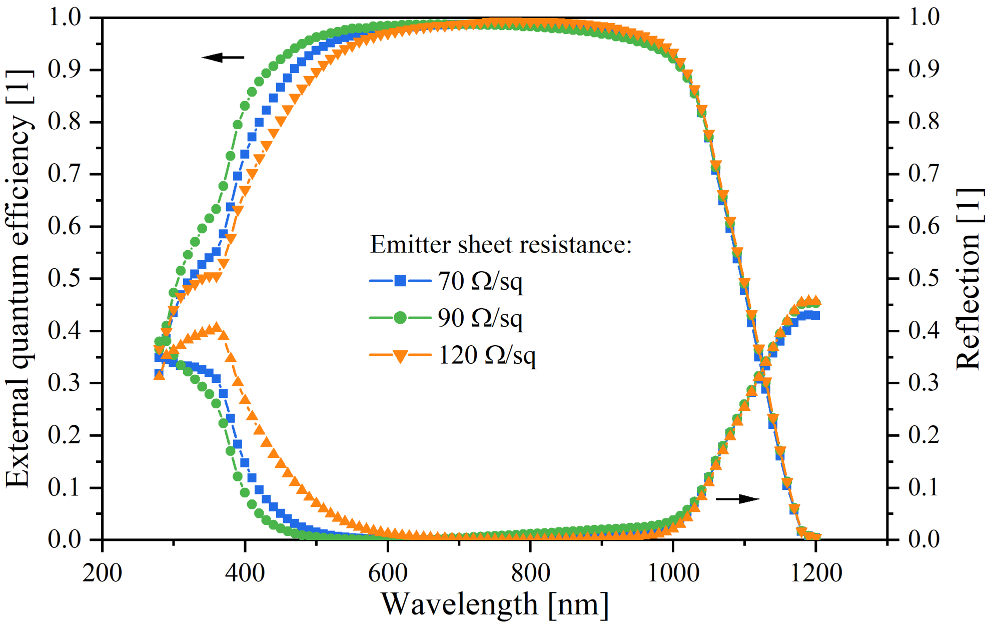

Figure 6.4: External quantum efficiency (EQE) and reflection curve of three groups with different emitter sheet resistance measured from the wavelength of 280 to 1200 nm using a spectral response measurement device.

6.2 Impact of paste volume and grid pattern on the contact resistance

Rudolph *et al.* investigated different paste volume for the rear metallization of *n*-type PERT solar cell and they showed a significant impact of the paste volume on the contact formation [160]. In the sintering step, all organic components inside the Ag paste will be burned away due to the high temperature, leaving only Ag particles and glass frits. This phase is known as the burned-out phase. By varying the paste volume, the amount of glass frit per contact area can be controlled, and its influence on the contact formation of PERC solar cells can be investigated. In this section, the effect of paste volume through multiple printing steps of two different Ag pastes on the contact formation at the emitter of PERC solar cells is studied. The multiple prints using the print-on-print approach are conducted as a helping method to increase the paste volume by keeping the same contact area. However, on the production line, a similar high paste amount can be accomplished in a single printing step by modifying the screen specification, such as EOM thickness and mesh diameter. Two different commercial Ag pastes were chosen for finger metallization as representative of the standard printing paste and the fine-line printing paste. Furthermore, two different metallization routes for the front metallization, namely firing with and without busbars, are introduced to review its impact on the contact formation.

6.2.1 Experimental details

In this experiment, *p*-type boron-doped Cz-Si wafers with an average resistivity of 1.6 Ω·cm, a thickness of 180 μm and a cell size of 244.32 cm^2 were used. The solar cells with PERC structure were fabricated based on the *Centaurus* processing route [21], [151], [152], similar as mentioned before in section 6.1.1. This time, only one emitter layer with in situ oxidation was used and it has a dopant surface concentration of approximately $8 \cdot 10^{19}$ cm^{-3}, resulting in an emitter sheet resistance of 90 Ω/sq (see Figure 6.1). After the front end process was finished, the precursors were ablated with dot-LCO pattern on the rear side. A full area of aluminum was screen-printed on the rear without featuring Ag/Al soldering pads and then dried.

Figure 6.5 displays two different front metallization routes used in this experiment. In the metallization route (a) “firing with busbars,” six busbars were screen printed at first followed by the drying step. Then, the Ag fingers were screen-printed with two different Ag pastes. Two commercial Ag pastes for finger metallization were chosen to represent the standard printing paste (Ag paste X) and the fine-line printing paste (Ag paste Y). The finger metallization steps were repeated up to three times with subsequent drying steps to generate various paste volumes. The number of prints is labeled as 1P for one print, 2P for two prints and 3P for three prints. Each metallization step was performed with screen-printing technology from Baccini. All samples were sintered with a Centrotherm fast-firing furnace at a peak temperature of 840 °C and a belt speed of 5.4 $m \cdot min^{-1}$. For the metallization route (b) “firing without busbars,” six busbars were screen-printed for all samples after the sintering step with a non-firing through Ag paste, which required an additional curing step at a temperature of 200 °C. Finger geometry and *I*-*V* data were measured and analyzed as in 6.2.1.

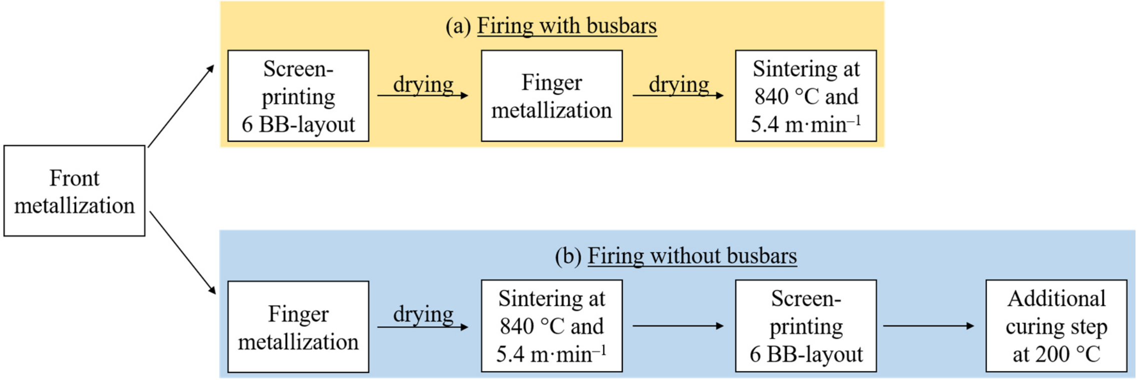
(a) Firing with busbars
Screen-printing 6 BB-layout
drying
Finger metallization
drying
Sintering at 840 °C and 5.4 m·min⁻¹
Front metallization
(b) Firing without busbars
Finger metallization
drying
Sintering at 840 °C and 5.4 m·min⁻¹
Screen-printing 6 BB-layout
Additional curing step at 200 °C

Figure 6.5: Two metallization routes for the front surface: (a) firing with busbars; (b) firing without busbars.

6.2.2 Results and discussions

Figure 6.6 presents the finger geometries of both Ag pastes X and Y for multiple printing steps of 1P to 3P. For both pastes, the finger height was raised significantly by increasing the number of prints, and an incremental increase of finger width by 2 µm was observed for each step of finger metallization. The finger aspect ratio and the finger cross-sectional area for both pastes were significantly increased by multiplying the printing steps. Although a wider finger was observed, the fine-line printing Ag paste Y achieved a higher aspect ratio than the standard Ag paste X due to a significant increase in finger height. The print-on-print method proved to be a good method to increase the paste volume, which is reflected in the finger cross-sectional area. The first print of Ag paste X resulted in a finger cross-sectional area of 300 µm^2 and three prints achieved a finger cross-sectional area of 420 µm^2. In contrast, Ag paste Y significantly increased finger cross-sectional from 1P to 3P, which increased from 484 µm^2 to 868 µm^2. Hence, the multiple Ag printing steps successfully increased the paste volume without significantly widening the contact area. As a result of these multiple printing steps, the amount of glass frit per contact area will rise linearly to the increase in finger cross-cross sectional area. No difference in finger geometries was observed for two different metallization routes considering the same Ag paste and screen were used.

The series resistance analysis for all groups is displayed in Figure 6.7. The contact resistivity of Ag pastes X and Y showed a different trend by increasing the printing steps. The increase of paste volume from 1P to 3P decreased the contact resistivity for the cells fired with busbars of the standard paste X significantly from 10 to 2 mΩ·cm^2. A lower improvement of contact resistivity from 0.5 to 0.2 mΩ·cm^2 was discovered of the cells fired without busbars from 1P to 3P. For the fine-line Ag paste Y, the outcome was inverted: a lower contact resistivity was achieved for a lower paste volume, for both metallization routes. This observation could be explained by the fact that Ag paste Y was designed for fine-line printing, and therefore a further increase of paste volume deteriorates the contact formation of Ag paste with silicon.

This different behavior between two pastes X and Y might be caused by the difference in the paste composition, possibly glass frit content. A certain amount of glass frit is required to etch the passivation and antireflection SiN_x layer, enabling a good contact formation between Ag finger and silicon [99], [154], [161]. One-time print of standard Ag paste X appears to have less glass frits than necessary, resulting in a bad contact formation. Therefore a further increase in the paste volume surges the glass frit amount above the threshold to form a good ohmic contact. This paste was designed a few years back, when higher laydown was still achieved through meshes with bigger wire diameter, higher emulsion over mesh and wider screen openings. On the contrary, Ag paste Y for fine-line printing is developed with the necessary amount of glass frit to eliminate the need for numerous printing steps. Therefore, a raise in paste volume of Ag paste Y through multiple print increased the amount of glass frit unnecessarily, producing a bad contact formation caused by the increase in interfacial glass thickness [160]. The interfacial glass layer between the Ag fingers and silicon performs as an insulation layer and increases contact resistivity.

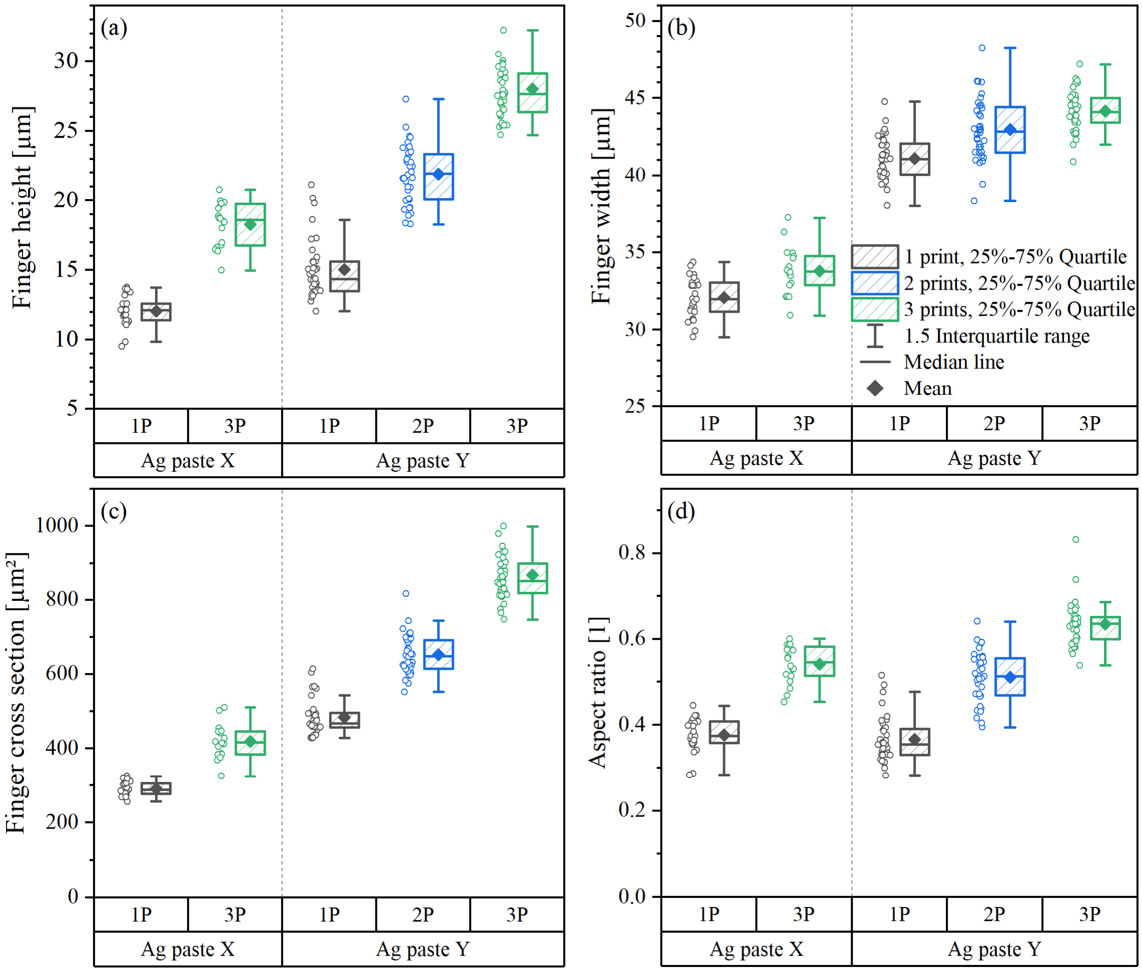

Figure 6.6: Finger geometries of two different Ag pastes X and Y for a various number of prints from one print, two prints and three prints: (a) finger height, (b) finger width; (c) finger cross-sectional area; (d) finger aspect ratio.

The metallization route "firing without busbars" achieved a lower contact resistivity for both pastes than the cells fired with busbars due to the short-circuit effect. Kim *et al.* [162] and Chu *et al.* [163] studied this short-circuit effect, and they concluded that the existence of busbars during firing allows the generated electron from one metal grid (finger) to flow along the busbars to the other metal grids. Separating the busbars from the metal grid during the firing process minimized the electron flow to only one finger and improved the contact resistivity. Therefore, the contact resistivity can be further reduced by the metallization route "firing without busbars." As displayed in Figure 6.7(b), the lateral finger resistance analysis reveals that the increase in paste volume reduced the lateral finger resistance for both Ag pastes. The standard Ag paste X achieved an average finger line resistance of 0.75 Ω·cm^{-1} by increasing the paste volume from 300 to 420 µm^2. With a finger cross-sectional area of 484 µm^2 for the first print of the fine-line Ag paste Y, the average lateral finger resistance of 0.56 Ω·cm^{-1} was achieved. The group with three prints (A_{finger} = 868 µm^2) reduced the finger line resistance down to 0.31 Ω·cm^{-1}.

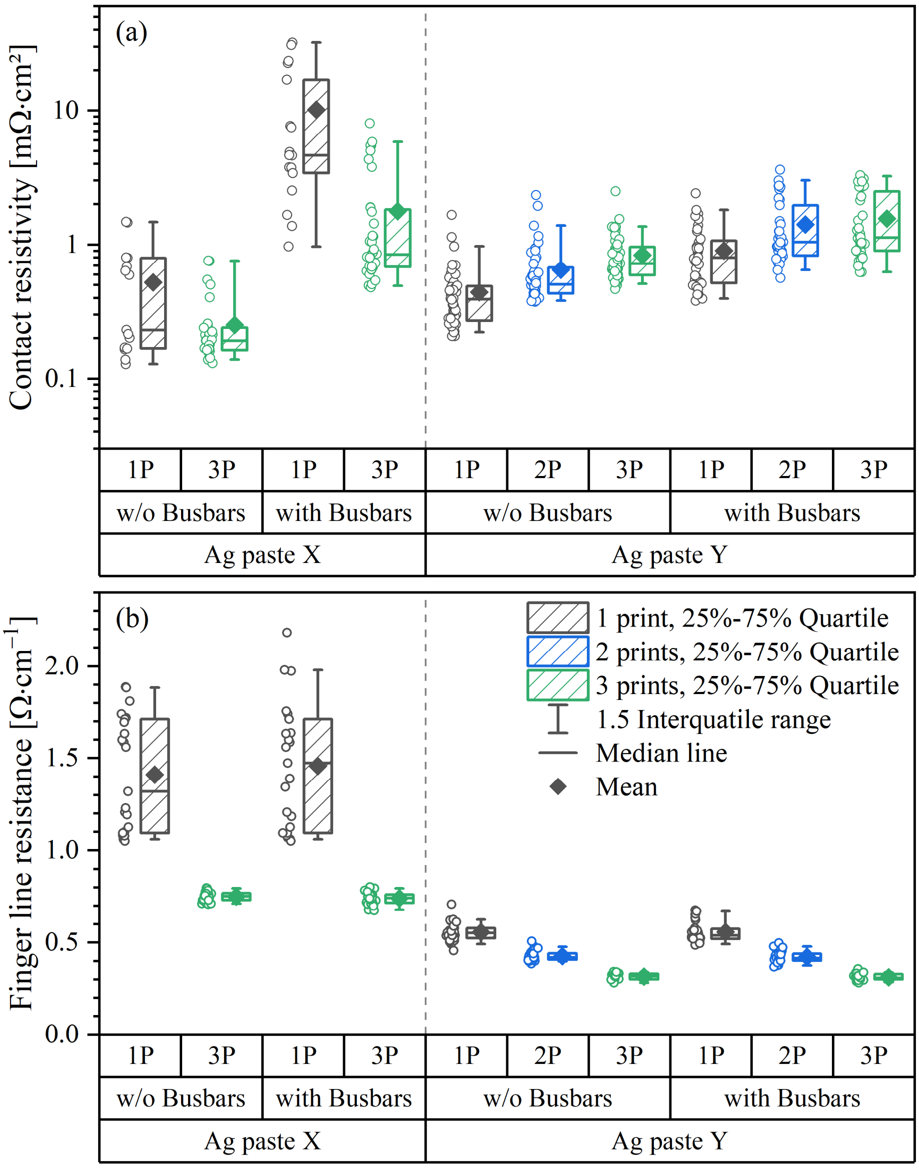

Figure 6.7: Analysis of series resistances for two different Ag pastes, two different metallization routes and various number of prints: (a) contact resistivity; (b) lateral finger resistance.

Figure 6.8 shows the *I-V* values of each printing step for both Ag pastes and two different metallization routes. The J_{sc} is correlated to the finger width. The wider fingers of paste Y resulted in a lower J_{sc} than paste X. The metallization route firing without busbars achieved a lower J_{sc} value for both Ag pastes and all printing steps due to the light-induced degradation mechanism based on the boron-oxygen complex [165]–[168]. The additional curing step at 200 °C after sintering step accelerates the degradation of solar cells for the groups of firing without busbars. The boron-doped *p*-type PERC solar cells are required to undergo another treatment to eliminate the boron-oxygen complexes and stabilize the PERC solar cells, called the regeneration step [169], [170], or must be measured in a freshly annealed state. No significant difference in J_{sc} was detected considering the almost similar finger width between the different printing steps. The V_{oc} value was identical for various printing steps.

However, separating the busbars for the firing steps reduces the V_{oc} values caused by the boron-oxygen light-induced degradation effect explained above. The *FF* values of standard Ag paste X improved significantly with increasing paste volume for both metallization approaches due to the significant improvement of contact resistivity and the lateral finger resistance. The improvement of lateral finger resistance for a higher paste volume of Ag paste Y was minimized by a slight increase in contact resistivity, resulting in a similar *FF* value for each printing step. Hence, a higher cell efficiency was achieved by a higher paste volume of Ag pastes X and Y caused by a considerable reduction in lateral finger resistance. The average cell efficiency of the groups “firing without busbars” for both pastes X and Y were lower than the group “firing with busbars” resulting from the significant losses of J_{sc} and V_{oc}. These losses were caused by the light-induced degradation mechanism based on the boron-oxygen complex.

6.2.3 Chapter summary

In this chapter, the influence of emitter sheet resistance and the paste volume on the contact formation of PERC solar cells are studied. A higher emitter sheet resistance of PERC solar cells is essential to achieve a higher J_{sc} and V_{oc} value due to a higher absorption in the low wavelength region and lower front surface recombination velocity. However, a rise in emitter sheet resistance increases the resistance of lateral transport in the emitter and makes a contact formation with low contact resistivity more challenging: non-uniform emitter regions at local points over the cells results in a big spread of contact resistivity from 8 to 100 $m\Omega \cdot cm^2$. By increasing the number of fingers, the *FF* can be improved resulting from a lower resistance in the emitter region but simultaneously the finger width needs also to be reduced to mitigate the power loss due to higher shading. Here, the ultrafine line fingers can play a significant role in achieving a higher cell efficiency. Other solutions to improve the contact formation for a PERC cell with higher sheet resistance are by applying a selective n^+-layer under the contact fingers [155]–[157] or modifying the Ag paste to improve further the contact formation for a low dopant surface concentration and low emitter depth [154].

The paste volume affects the contact formation depending on its paste composition. The standard Ag paste X achieved a higher contact resistivity for a lower paste volume due to its low amount of glass frit. By increasing the paste volume from 300 to 400 μm^2, the amount of glass frit required for a good contact formation was achieved, resulting in a lower contact resistivity of paste X. On the contrary, the fine-line Ag paste Y showed the lowest contact resistivity for a low paste volume indicating that the Ag paste Y has a sufficient amount of glass frit, enabling a good contact between Ag finger and emitter. Increasing the paste volume of paste Y further worsens the contact formation between Ag fingers and silicon, possibly by the increase in thickness of the interface glass that acts as isolation barrier at the interface region [160].

Therefore, the Ag paste modification and adjustment for different finger geometries and emitter profiles could play a significant role in achieving an excellent ohmic contact. The front metallization route of firing the fingers without the busbars exhibits a lower contact resistance for both pastes than the firing process with busbars due to the short-circuit effect. However, in this experiment, the additional curing step for the non-firing through busbars led to a degeneration of PERC solar cells resulting in J_{sc} and V_{oc} loss due to the formation of boron-oxygen complexes. To minimize this degradation and stabilize the PERC solar cells, after the curing step the cells are required to be simultaneously illuminated at a high irradiation degree and a high annealing temperature [168]–[170].

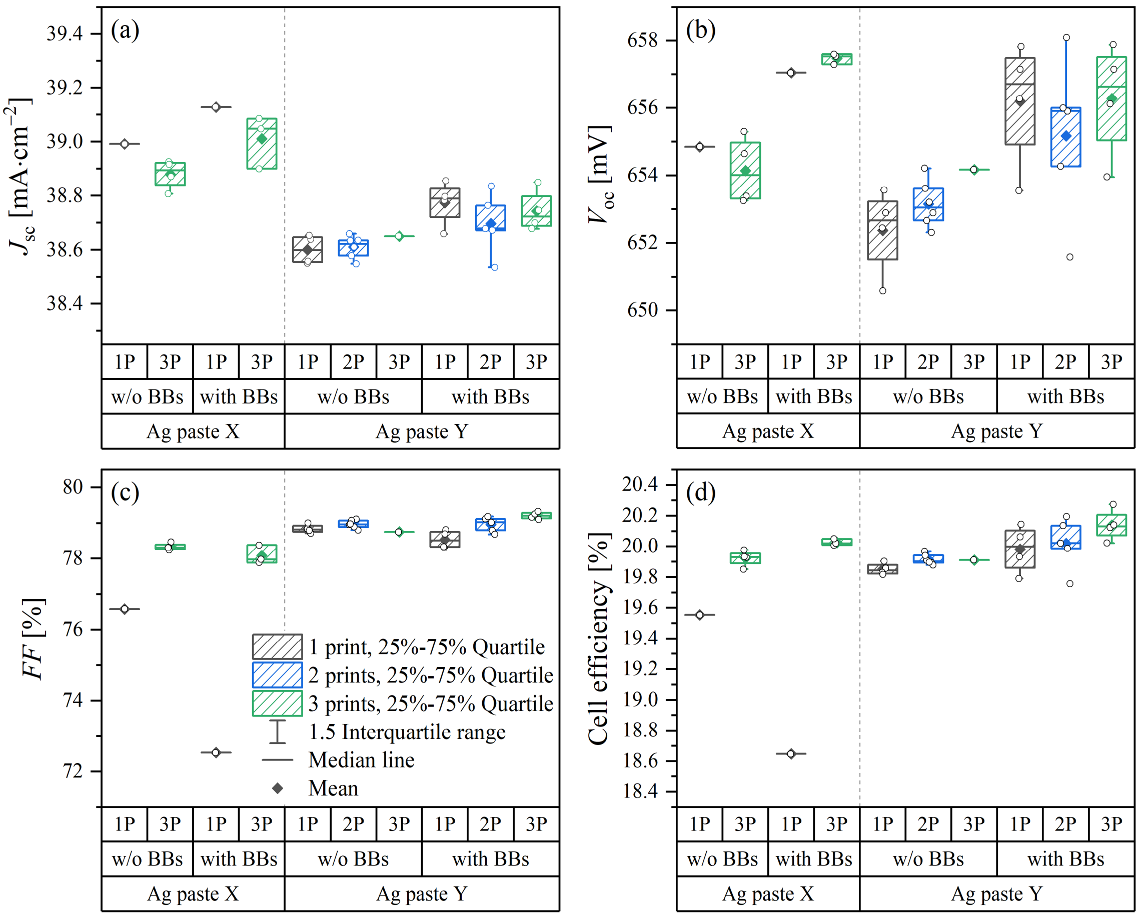

Figure 6.8: *I*-*V* parameters versus the number of prints for two different pastes, Ag pastes X and Y, and two front metallization routes, firing without busbars (w/o BBs) and firing with busbars (with BBs): (a) J_{sc}, (b) V_{oc}; (c) *FF*; (d) cell efficiency.

7 Summary and Outlook

7.1 Summary

Despite a steady reduction in silver consumption per cell, the Ag demand of the PV industry has increased yearly, as the global production volume of photovoltaic modules has risen rapidly in the last few years. This growth is projected to accelerate in the future as PV will undoubtedly be one of the dominant future energy sources due to its low cost and high maturity, as well as the zero-greenhouse emissions energy policies of an increasing number of countries. However, the speed of silver reduction might be stagnant, and it may require ten years to reduce the silver consumption from the current standard of 90 mg per cell to 50 mg per cell due to the limitation in industrial standard screen-printing technology. Therefore, an alternative to screen-printing technology for the front metallization is an attractive way to prevent Ag depletion in the future, and its readiness in mass production must be proved. The work in this thesis has explored the potential of the laser-based Pattern Transfer Printing (PTP) technology for reducing silver consumption while simultaneously maintaining a good characteristic of a solar cell.

PTP technology was first introduced in 2015, presenting its ability to fabricate Ag fingers with an average finger width of 27 µm [15]. The main goal of this thesis is to enhance the understanding of the PTP process and to optimize the PTP technology further, targeting narrower Ag fingers below 20 µm with a good aspect ratio above 0.5. Thus, a lower production cost due to less Ag consumption and a higher cell efficiency due to less shading at the front surface with an insignificant increase in series resistance can be achieved by PTP technology. PTP application to the front metallization of c-Si solar cells as an alternative to industrial screen-printing technology and its readiness for mass production were assessed, comparing the finger shape, electrical properties of the solar cells and the difference in silver paste consumption between both technologies. Various Ag pastes with different rheological properties and various polymer materials were investigated to understand the governing principle of the laser transfer process of PTP for achieving narrower Ag fingers. Furthermore, the effect of ultrafine fingers obtained with PTP technology on contact formation was investigated.

The **development and optimization** of two PTP printing steps, namely filling and transfer, were presented. The initial angle of two squeegee blades was designed to be 60° toward the film surface. This resulted in cavities inside trenches due to scooping with depths between 3 and 9 µm, producing inhomogeneous fingers and thus a higher lateral finger resistance. By increasing the angle of the second squeegee from 60° to 130°, this scooping effect was limited to be around 1 and 2 µm. Hence, the paste filling process of PTP was improved, producing more homogeneous finger height across the cell area.

The laser power investigation presented the strong influence of laser power for the transfer process of PTP. A certain amount of laser power is required to create sufficient pressure at the paste-film interface, enabling a complete paste release onto a substrate underneath. An increase in laser power improved the straightness of Ag fingers, but it simultaneously created more debris around the printed fingers due to stronger splashing. Three possible scenarios in the dependence on the laser power applied during the transfer process of PTP were observed: no transfer, optimum transfer and explosive transfer.

The “no transfer” scenario happens when the operating laser power is insufficient to generate enough pressure at the paste-film interface to overcome the adhesion of Ag pastes to the polymer film. Thus, Ag paste cannot be transferred and stays inside the trench. The “optimum transfer” scenario occurs when the operating laser power is just high enough to generate adequate pressure in the interface region to overcome the adhesion between Ag paste and polymer film. Hence, Ag paste is released and deposits onto the substrate underneath. Using the optimum laser power, the Ag fingers had the narrowest finger width and the highest aspect ratio with only a slight trace of splashing. In the “explosive transfer” scenario, where the operating laser power is notably higher than in the previous scenarios, the pressure at the paste-film interface is not only high enough to exceed the adhesive strength ensuring a successful paste transfer, but also overcomes the paste cohesion strength, creating a considerable amount of debris and accelerating the ejected paste onto the substrate in such a way as to deform the Ag fingers towards a broader line width.

The applied laser power determines the **success of the transfer process** of PTP technology and affects the print quality, including finger width, finger aspect ratio and amount of debris. Therefore, an optimization of laser power is mandatory when using PTP technology to achieve optimum print quality. The increase in laser power reduces the aspect ratio of the finger lines. Even though the optimum laser power obtained the narrowest finger lines with the highest aspect ratio, a slightly higher laser power than the laser power for the optimum transfer was principally used to avoid local line interruptions resulting from laser inhomogeneity in certain areas. The term “laser power threshold” was introduced, describing the laser power required to completely transfer the paste from the entire trenches without any interruptions over the whole area of a solar cell. However, the laser power threshold creates a certain amount of debris around the paste main body and sacrifices the best aspect ratio of printed lines.

Although the laser process is quite destructive, it is still utilized in several manufacturing steps in the PV industries, such as scribing and ablation of solar cells. Therefore, it is necessary to conduct an investigation of the laser-induced damage of the PTP technology on the passivation quality of solar cells. No significant differences were observed on the I-V parameters and PL images before and after the laser process of PTP. Hence, it can be concluded that the laser irradiation during the laser transfer process of PTP technology is harmless and non-destructive for the substrate surface and the passivation quality of c-Si solar cells.

Two key aspects that control the PTP laser transfer process from a material point of view were studied, namely the physico-chemical properties of the Ag pastes and film materials. A **deeper understanding of the laser transfer process** related to the relationship between the materials and the laser power threshold was attained, providing guidelines for adjusting the Ag paste and film properties, and therefore facilitating narrower Ag fingers using PTP technology.

The contactless laser printing method of PTP technology allows the modification of Ag pastes with a wide range of yield stress, even above the typical yield stress of commercialized Ag pastes dedicated for screen-printing application, since several screen-printing issues such as paste clogs inside the screen aperture, no adhesion, and a reduction of screen lifetime, are irrelevant for PTP technology. A high yield stress Ag paste exhibits a higher aspect ratio in PTP-printed fingers than a low yield stress one. Two phenomena were considered for the contribution to the spreading of the paste with low yield stress. First, laser power dissipation results in vaporization of volatile components in Ag paste, and the corresponding gas pressure at the paste-film interface exceeds the adhesion between paste and polymer film, providing an additional contribution to the force acting on the paste during deposition. Second, the laser energy is absorbed within the Ag paste at the interface and raises the paste temperature. The Ag surface at the paste-film interface sustains the highest temperature increase. However, due to the high thermal conductivity of Ag paste, the Ag paste temperature inside the trenches is also raised quite significantly. Accordingly, the yield stress of the Ag paste decreases.

The trench shape and geometry were observed to affect the laser power threshold. The trench design with a lower ratio between the circumference and the equivalent horizontal area $r_{\mathrm{c/h}}$ required a lower laser power threshold than the trench design with a higher $r_{\mathrm{c/h}}$ value. This relationship is related to the top-hat laser beam of PTP technology. The longer the equivalent horizontal of a trench, the lower the laser power threshold required for a successful paste transfer. The shape of PTP fingers was identical to the shape of their respective trenches. However, the finger geometries were smaller than the respective trench shape due to shrinkage, which was mainly caused by the incomplete filling process with a depth of one to two µm, the evaporation of the solvent during the drying process, the removal of the organic binder during the burn-out phase, and the sintering of the Ag particles at the firing process.

The influences of film and paste properties on the laser power threshold were also investigated to gain a deeper understanding of the laser transfer process of PTP technology. It was observed that a low laser power threshold for paste release can be achieved through a low boiling point of the organic vehicle and low wettability between the Ag paste and the film material. The film materials exhibit only minor differences regarding absorption, reflection or transmission of incident laser irradiance. These results establish the basis and provide guidelines for future research on designing the Ag paste and modifying film materials for solar cell metallization based on PTP technology. Hence, narrower fingers with a higher aspect ratio can be achieved using PTP technology at an even lower laser power threshold.

The **application of PTP** to the front metallization of PERC solar cells with a six-busbar layout was evaluated and compared to the state-of-the-art screen-printing technology. Using a mesh screen with 400 meshes per inch with an angle of 22.5°, wire diameter of 13 µm, EOM of 15 µm and screen aperture of 28 µm, an average finger width of 38 µm with an aspect ratio of 0.37 was obtained. This is in line with the finger width achieved in industrial mass production [16]. Four different trench geometries from the same polymer film material were investigated and compared with the state-of-the-art screen-printing technology. Using the trench design 1 (trapezoidal trench shape with a bottom opening of 30 µm), an average finger width of 22 µm with an aspect ratio of

0.55 could be achieved, resulting in the best cell efficiency of 21.73% (as-measured) among the PTP groups. Despite a modest *FF* loss caused by a higher series resistance, a significant gain in J_{sc} and a smaller gain in V_{oc} increased the cell efficiency by 0.12%$_{abs}$ compared to the reference screen-printed cells. More importantly, the amount of silver used for the front metallization was reduced by 54% compared with the screen-printing reference.

The trapezoidal trench shape with a bottom opening of 20 µm (trench design 3) resulted in the narrowest Ag finger lines with an average width of 18 µm and an aspect ratio of 0.51, enabling 74% silver reduction vs. the screen-printing reference. The J_{sc} and V_{oc} were increased by 0.45 mA·cm^{-2} and 3.1 mV, respectively. Still, a higher series resistance due to a higher finger contact resistance and lateral finger resistance reduced the *FF* by 2.1%, resulting in an efficiency loss of 0.17%$_{abs}$ for PTP-metallized cells with trench design 3. The contact resistivity analysis shows that the modification of commercially available screen-printing pastes to PTP requirements has successfully improved the contact resistance of PTP-printed fingers with a cross-sectional area around 200 µm^2 (PTP group with trench design 1 and 2). The contact resistivity of these groups was lower than for the screen-printed fingers with a cross-sectional area of 400 µm^2. This also proves that the contact resistivity is not the limiting factor when going to cross-sectional areas as small as 200 µm^2. However, for finger cross-sectional areas smaller than 200 µm^2, namely PTP groups using trench designs 3 and 4, the contact resistivity and the lateral line resistance of Ag fingers remain the limiting factors.

The current six-busbar setup of the PERC cells minimizes the gain in cell efficiency from significant J_{sc} and V_{oc} improvements of PTP groups due to a higher lateral finger resistance. The simulation results concluded that the *FF* could be increased significantly by doubling the busbar number from six to twelve while maintaining the total busbar shading area. Therefore, a higher cell efficiency of all PTP groups compared to the reference group could be achieved. A different simulation experiment was also conducted, presenting the importance of the front contact grid optimization for a **good trade-off** between cell efficiency and silver consumption. For the current cell layout with six busbars, an increase in cell efficiency from 21.73% to 21.77% may be achievable for trench design 1, by increasing the finger number from 112 to 139 fingers. In the simulations, this reduced the contribution of contact resistivity to the total series resistance, and therefore, a higher *FF* and cell efficiency might be obtained via this route. However, it also increases the Ag consumption by 24%. Hence, a compromise between J_{sc} gain, *FF* loss, and the production cost is mandatory in designing the layout of the PTP grid to achieve cost-efficient solar cells.

Two screen approaches to improve the printability using a smaller screen aperture were investigated; zero-degree mesh screen (or knotless screen) and the screen with a smaller wire diameter. By modifying the conventional mesh angle from 22.5° to 0°, the open area inside the screen aperture is increased from 64.6% to 80.1%. Therefore, the knotless screen reduces the mesh marks significantly, improving the homogeneity of printed fingers. A significant reduction of screen aperture from 28 to 16 µm results in a smaller open area inside the aperture, but the same open area of 64% inside the screen aperture of 16 µm can be maintained using the smallest wire available on the market, with a diameter of 11 µm. Both screen approaches achieved a similar finger width for the same screen aperture. However, the knotless screen significantly improved the finger aspect ratio and the finger cross-sectional area, resulting in higher *FF* and cell efficiency than the screen with a mesh angle of 30° and smaller wire diameter. In this experiment, the narrowest finger from screen-printing technology had an average width of 22 µm with an aspect ratio of 0.6, using a knotless screen with 440 mesh count per inch, wire diameter of 13 µm, EOM of 15 µm and screen aperture of 16 µm.

A higher emitter sheet resistance of PERC solar cells is essential to achieve a higher J_{sc} and V_{oc} caused by a higher absorption in the low wavelength region and lower front surface recombination velocity. However, it causes a contacting problem between Ag fingers and silicon due to the non-uniform emitter region at local points over the cells resulting in a big spread of contact resistivity from 8 to 100 $m\Omega \cdot cm^2$. This high contact resistivity value can be compensated by increasing the number of fingers, and here, the ultrafine fingers play a significant role in minimizing the cell power loss caused by shading. The Ag paste volume affects the contact formation depending on its paste composition. The Ag paste for fine-line printing is designed to enable a good contact between the Ag finger and emitter for a certain amount of paste volume. An increase of this paste volume threshold worsens the contact formation due to the rise in interface glass acting as the isolation barrier in the interface region between Ag finger and silicon.

7.2 Outlook

The results presented in this thesis demonstrate the vast potential of ultrafine Ag fingers using PTP technology to fabricate cost-effective silicon solar cells. However, the demonstrated efficiency gain is probably to be insufficient to stimulate investments of cell producers in PTP technology, which involve substantial capital investment and long-term modification of production lines. Furthermore, the intellectual property protection of PTP and suitable polymer film might hamper the market introduction, as producers are very adverse towards investments that would bind them to a single source of suppliers.

The contactless laser printing method of PTP allows Ag pastes with higher yield stress than conventional screen printing technology. Although the actual pressure that acted on the deposited line and the paste resistance against deformation cannot be quantified in this thesis, the narrowest Ag finger with the higher aspect ratio was achieved using Ag paste D with a yield stress of 1623 Pa. However, a yield stress limit for the PTP process is still unknown and excessively high yield stress might deteriorate trench filling, reducing the filling quality of PTP and therefore increasing the inhomogeneity of the Ag fingers. Therefore, future investigations with even higher yield stress may be required to investigate its influence not only on the finger geometry but also on the filling quality of the PTP process.

Laser power plays a significant role in the transfer process of PTP, determining a successful paste transfer as well as affecting the geometry of Ag fingers. The optimum laser power produces the narrowest Ag lines and also the best aspect ratio. However, the laser power threshold applied during the transfer process of PTP is slightly higher than the optimum laser power to compensate for lower laser power in particular cell areas due to the geometry of the laser deflection system, causing local line interruptions. Hence, a better laser deflection system for better optimization of laser power would be helpful in future work, ensuring a homogeneous laser power over the whole cell area and the narrowest fingers possible without debris.

A low laser threshold was observed for Ag paste with a lower boiling temperature and a higher contact angle. However, it must be noted that the observed differences were relatively small, and further investigations, including a new batch of Ag pastes with a broader range of contact angles and boiling points, may be helpful to corroborate the findings in this thesis and to separate the contributions of wetting of Ag paste on polymer film and boiling point differences. It would also be interesting to look at the effect of debris around the PTP-printed fingers on cell efficiency.

The influence of three different film materials with various thicknesses on the laser power threshold was investigated. The results of the investigation of material properties indicate that the laser power threshold is mainly defined by the thickness of the film material, even though the transmission of the thickest film material is the lowest. This result appears to be contradictory, however, it should be kept in mind that the paste-film interface is shifted along the axis of the laser beam according to the material thickness, so the laser focus plane may not completely match for all film materials. Hence, further investigations into these aspects are mandatory to resolve the issue of polymer material and film thickness by comparing films of similar thickness but made from different materials.

The present work demonstrates the great potential of PTP technology for the front metallization step of silicon solar cells. PTP produces finer line Ag fingers than screen-printed references, leading to a lower silver consumption and increasing the cell efficiency. The simulation results show that a higher cell efficiency of all PTP groups could be achieved by changing from the current six-busbar layout to nine or twelve busbars. Increasing the number of busbars is a similar trend in mass production since the cell size has been changed quite rapidly over the last few years from M2 with an area of 244.32 cm^2 to M6 with 274.15 cm^2, M10 with 399.98 cm^2, or M12 with 440.96 cm^2. Further investigation to evaluate the PTP performance on a bigger cell size with a higher busbar number of twelve is therefore essential.

To raise the competitiveness vs. screen-printing technology, the current throughput of PTP needs to be increased from 3000 wafers per hour to 4000 wafers per hour or a similar throughput as standard screen-printing in mass production. The attractiveness of PTP might be increased if the used polymer film can be recycled and used several times again, reducing the material cost of PTP significantly and simultaneously reducing plastic waste. The results in this work can serve as basic guidelines for further development of PTP technology and also as a starting point for applying PTP technology to other cell structures, such as PTP technology for silicon heterojunction solar cells using a low-temperature silver or copper paste.

Bibliography

[1] CONSTRAIN, "ZERO IN ON: A new generation of climate models, COVID-19 and the Paris Agreement," Zenodo, The CONSTRAIN Project Annual Report, 2020. doi: 10.5281/ZENODO. 4282461.

[2] IRENA, "Global Renewables Outlook. Energy transformation 2050," International Renewable Energy Agency, Abu Dhabi, UAE, 2020. Accessed: Sep. 17, 2021. [Online]. Available: https://www.irena.org/publications/2020/Apr/Global-Renewables-Outlook-2020

[3] R. Manish *et al.*, "Global Energy System based on 100% Renewable Energy – Power, Heat, Transport and Desalination Sectors," Study by Lappeenranta University of Technology and Energy Watch Group, Lappeenranta, Berlin, 2019, pp. 1–321, ISBN: 978-952-335-339–8.

[4] Solar Power Europe, "Global Market Outlook for Solar Power 2021-2025," Jul. 2021. Accessed: Sep. 09, 2021. [Online]. Available: https://www.solarpowereurope.org/wp-content/uploads/2021/07/SolarPower-Europe_Global-Market-Outlook-for-Solar-2021-2025_V1.pdf

[5] International Energy Agency IEA, "World Energy Outlook 2020," IEA, Paris, France, Oct. 2020. Accessed: Jul. 22, 2021. [Online]. Available: https://www.iea.org/reports/world-energy-outlook-2020

[6] IRENA, "World Energy Transitions Outlook: 1.5°C pathway," International Renewable Energy Agency, Abu Dhabi, UAE, 2021. Accessed: Aug. 17, 2021. [Online]. Available: https://www.irena.org/publications/2021/Jun/World-Energy-Transitions-Outlook

[7] IRENA, "Renewable capacity statistics 2021 International Renewable Energy Agency (IRENA)," Abu Dhabi, UAE, 2021. Accessed: Jul. 17, 2021. [Online]. Available: https://www.irena.org/publications/2021/March/Renewable-Capacity-Statistics-2021

[8] Fraunhofer-Institut für Solare Energiesysteme ISE, "Photovoltaics Report, updated: 30 June 2021," 2021. Accessed: Jul. 17, 2021. [Online]. Available: https://www.ise.fraunhofer.de/content/dam/ise/de/documents/publications/studies/Photovoltaics-Report.pdf

[9] D. Bogdanov *et al.*, "Low-cost renewable electricity as the key driver of the global energy transition towards sustainability," *Energy*, vol. 227, p. 120467, Jul. 2021, doi: 10.1016/j.energy.2021.120467.

[10] Y. Nakao and T. Hiyama, "Silicon-based cross-coupling reaction: an environmentally benign version," *Chem. Soc. Rev.*, vol. 40, no. 10, pp. 4893–4901, Sep. 2011, doi: 10.1039/C1CS15122C.

[11] M. Okil, M. S. Salem, T. M. Abdolkader, and A. Shaker, "From Crystalline to Low-cost Silicon-based Solar Cells: a Review," *Silicon*, Mar. 2021, doi: 10.1007/s12633-021-01032-4.

[12] The Silver Institute and Metal Focus, *World Silver Survey 2021*, 31st Edition. Washington, D.C.: Silver Institute. ISBN: 978-1-9162526-5-3, 2021.

[13] M. Fischer, A. Metz, and S. Raithel, "Semi International Technology Roadmap for Photovoltaics (ITRPV) - Challenges in c-Si Technology for Suppliers and Manufacturers," in *27th European Photovoltaic Solar Energy Conference and Exhibition*, Frankfurt am Main, Germany, 2012, pp. 527–532.

[14] VDMA Photovoltaic Equipment, "International technology roadmap for photovoltaic (ITRPV) - 2020 Results, 12th Edition," Frankfurt am Main, Germany, 2021. Accessed: Apr. 30, 2021. [Online]. Available: https://itrpv.vdma.org/en/

[15] J. Lossen, M. Matusovsky, A. Noy, Ch. Maier, and M. Bähr, "Pattern Transfer Printing (PTP^{TM}) for c-Si Solar Cell Metallization," *Energy Procedia*, vol. 67, pp. 156–162, Apr. 2015, doi: 10.1016/j.egypro.2015.03.299.

[16] VDMA Photovoltaic Equipment, "International technology roadmap for photovoltaic (ITRPV) - 2019 Results, 11th Edition," Frankfurt am Main, Germany, 2020. Accessed: Apr. 23, 2021. [Online]. Available: https://itrpv.vdma.org/en/

[17] M. A. Green, "The Passivated Emitter and Rear Cell (PERC): From conception to mass production," *Sol. Energy Mater. Sol. Cells*, vol. 143, pp. 190–197, Dec. 2015, doi: 10.1016/j.solmat.2015.06.055.

[18] K. Chen, Y. Liu, X. Wang, L. Zhang, and X. Su, "Novel texturing process for diamond-wire-sawn single-crystalline silicon solar cell," *Sol. Energy Mater. Sol. Cells*, vol. 133, pp. 148–155, Feb. 2015, doi: 10.1016/j.solmat.2014.11.016.

[19] H. Seigneur, E. J. Schneller, N. S. Shiradkar, and W. V. Schoenfeld, "Effect of Diamond Wire Saw Marks on Solar Cell Performance," *Energy Procedia*, vol. 92, pp. 386–391, Aug. 2016, doi: 10.1016/j.egypro.2016.07.117.

[20] H. Sekhar, T. Fukuda, Y. Kida, K. Tanahashi, and H. Takato, "The impact of damage etching on fracture strength of diamond wire sawn monocrystalline silicon wafers for photovoltaics use," *Jpn. J. Appl. Phys.*, vol. 57, no. 12, p. 126501, Nov. 2018, doi: 10.7567/JJAP.57.126501.

[21] T. Dullweber and J. Schmidt, "Industrial Silicon Solar Cells Applying the Passivated Emitter and Rear Cell (PERC) Concept—A Review," *IEEE J. Photovolt.*, vol. 6, no. 5, pp. 1366–1381, Sep. 2016, doi: 10.1109/JPHOTOV.2016.2571627.

[22] D. Kray, M. Hermle, and S. W. Glunz, "Theory and experiments on the back side reflectance of silicon wafer solar cells," *Prog. Photovolt. Res. Appl.*, vol. 16, no. 1, pp. 1–15, 2008, doi: 10.1002/pip.769.

[23] A. Goetzberger, B. Voß, and J. Knobloch, *Sonnenenergie: Photovoltaik: Physik und Technologie der Solarzelle*. Stuttgart, Germany: Teubner, 1994.

[24] K. Mertens, *Photovoltaik: Lehrbuch zu Grundlagen, Technologie und Praxis*, 4th Edition. München: Carl Hanser Verlag, 2018.

[25] P. Würfel and U. Würfel, *Physics of solar cells: from basic principles to advanced concepts*, 3rd edition. Weinheim: Wiley-VCH Verlag GmbH & Co. KGaA, 2016.

[26] A. Richter, M. Hermle, and S. W. Glunz, "Reassessment of the Limiting Efficiency for Crystalline Silicon Solar Cells," *IEEE J. Photovolt.*, vol. 3, no. 4, pp. 1184–1191, Oct. 2013, doi: 10.1109/JPHOTOV.2013.2270351.

[27] C. M. Proctor and T.-Q. Nguyen, "Effect of leakage current and shunt resistance on the light intensity dependence of organic solar cells," *Appl. Phys. Lett.*, vol. 106, no. 8, p. 083301, Feb. 2015, doi: 10.1063/1.4913589.

[28] O. Breitenstein, J. P. Rakotoniaina, M. H. A. Rifai, and M. Werner, "Shunt types in crystalline silicon solar cells," *Prog. Photovolt. Res. Appl.*, vol. 12, no. 7, pp. 529–538, 2004, doi: https://doi.org/10.1002/pip.544.

[29] D. E. Riemer, "The Theoretical Fundamentals of the Screen Printing Process," *Microelectron. Int.*, vol. 6, no. 1, pp. 8–17, Jan. 1989, doi: 10.1108/eb044350.

[30] S. Thibert, J. Jourdan, B. Bechevet, D. Chaussy, N. Reverdy-Bruas, and D. Beneventi, "Influence of silver paste rheology and screen parameters on the front side metallization of silicon solar cell," *Mater. Sci. Semicond. Process.*, vol. 27, pp. 790–799, Nov. 2014, doi: 10.1016/j.mssp.2014.08.023.

[31] Z. Fortu and L. X. Song, "Identifying Screen Properties to Optimise Solar Cell Efficiency and Cost," *Energy Procedia*, vol. 33, pp. 84–90, Jan. 2013, doi: 10.1016/j.egypro.2013.05.043.

[32] J. Stalnecker, "Stencil Screens for Fine-Line Printing," *Electrocompon. Sci. Technol.*, vol. 7, no. 1–3, pp. 47–53, 1980, doi: 10.1155/APEC.7.47.

[33] S. Tepner, L. Ney, M. Linse, A. Lorenz, M. Pospischil, and F. Clement, "Studying Knotless Screen Patterns for Fine-line Screen Printing of Si-Solar Cells," *IEEE J. Photovolt.*, vol. 10, no. 2, pp. 319–325, Mar. 2020, doi: 10.1109/JPHOTOV.2019.2959939.

[34] S. Tepner *et al.*, “Screen pattern simulation for an improved front-side Ag-electrode metallization of Si-solar cells,” *Prog. Photovolt. Res. Appl.*, vol. 28, no. 10, pp. 1054–1062, 2020, doi: https://doi.org/10.1002/pip.3313.

[35] T. Falcon, R. Anderson, and D. A. Clark, “Fine Line Printing of Front Side Metallisations Using Ultra Fine Mesh and Stencil Technologies,” in *27th European Photovoltaic Solar Energy Conference and Exhibition*, Frankfurt am Main, Germany, Sep. 2012, pp. 1739–1743. doi: 10.4229/27thEUPVSEC2012-2CV.5.39.

[36] H. Hannebauer, T. Falcon, J. Cunnusamy, and T. Dullweber, “Single Print Metal Stencils for High-efficiency PERC Solar Cells,” *Energy Procedia*, vol. 98, pp. 40–45, Nov. 2016, doi: 10.1016/j.egypro.2016.10.079.

[37] H. Hannebauer, S. Schimanke, T. Falcon, P. P. Altermatt, and T. Dullweber, “Optimized Stencil Print for Low Ag Paste Consumption and High Conversion Efficiencies,” *Energy Procedia*, vol. 67, pp. 108–115, Apr. 2015, doi: 10.1016/j.egypro.2015.03.294.

[38] V. Shanmugam *et al.*, “Analysis of Fine-Line Screen and Stencil-Printed Metal Contacts for Silicon Wafer Solar Cells,” *IEEE J. Photovolt.*, vol. 5, no. 2, pp. 525–533, Mar. 2015, doi: 10.1109/JPHOTOV.2014.2388073.

[39] J. Hoornstra and B. Heurtault, “Stencil Print Applications and Progress for Crystalline Silicon Solar Cells,” in *24th European Photovoltaic Solar Energy Conference*, Hamburg, Germany, Sep. 2009, pp. 989–992. doi: 10.4229/24thEUPVSEC2009-2BO.1.3.

[40] A. Lorenz, “Evaluierung von Rotationsdruckverfahren für die Metallisierung von Silicium-Solarzellen,” Ph.D. Dissertation, Albert-Ludwigs-Universität Freiburg, Freiburg im Breisgau, Germany, 2017. [Online]. Available: https://www.bookshop.fraunhofer.de/buch/evaluierung-von-rotationsdruckverfahren-fuer-die-metallisierung-von-silicium-solarzellen/248848

[41] A. Lorenz *et al.*, “High-throughput front and rear side metallization of silicon solar cells using rotary screen printing,” *Energy Procedia*, vol. 124, pp. 680–690, Sep. 2017, doi: 10.1016/j.egypro.2017.09.343.

[42] A. Lorenz *et al.*, “Project ‘Rock-Star’ – High-Speed Rotary Printing for Solar Cell Metallization: From Vision to Reality,” in *37th European Photovoltaic Solar Energy Conference and Exhibition*, Online Conference, Sep. 2020, pp. 400–403. doi: 10.4229/EUPVSEC20202020-2CV.1.53.

[43] A. Lorenz *et al.*, “Progress with Rotational Printing for the Front Side Metallization of Silicon Solar Cells,” in *32nd European Photovoltaic Solar Energy Conference and Exhibition*, Munich, Germany, Jun. 2016, pp. 413–419. doi: 10.4229/EUPVSEC20162016-2CO.2.4.

[44] A. Lorenz *et al.*, “Screen Printed Thick Film Metallization of Silicon Solar Cells - Recent Developments and Future Perspectives,” in *35th European Photovoltaic Solar Energy Conference and Exhibition*, Brussels, Belgium, 2018, pp. 819–824. doi: 10.4229/35THEUPVSEC20182018-2DV.3.65.

[45] M. Pospischil *et al.*, “High Speed Dispensing with Novel 6” Print Head,” *Energy Procedia*, vol. 98, pp. 61–65, Nov. 2016, doi: 10.1016/j.egypro.2016.10.081.

[46] M. Pospischil *et al.*, “Applications of parallel dispensing in PV metallization,” *AIP Conf. Proc.*, vol. 2156, no. 1, p. 020005, Sep. 2019, doi: 10.1063/1.5125870.

[47] M. Pospischil *et al.*, “Paste Rheology Correlating With Dispensed Finger Geometry,” *IEEE J. Photovolt.*, vol. 4, no. 1, pp. 498–503, Jan. 2014, doi: 10.1109/JPHOTOV.2013.2278657.

[48] K. Gensowski *et al.*, “Dispensing of low-temperature silver pastes,” Genk, Belgium, 2021, p. 020007. doi: 10.1063/5.0056103.

[49] David R. Lide, ed., *CRC Handbook of Chemistry and Physics*, 89th Edition (Internet Version 2009). CRC Press/Taylor and Francis, Boca Raton, FL.

[50] J. T. Horzel *et al.*, “Industrial Si Solar Cells With Cu-Based Plated Contacts,” *IEEE J. Photovolt.*, vol. 5, no. 6, pp. 1595–1600, Nov. 2015, doi: 10.1109/JPHOTOV.2015.2478067.

[51] N. Bay *et al.*, “Reliable Contact Formation for Industrial Solar Cells by Laser Ablation and Ni/Cu Plating,” in *29th European Photovoltaic Solar Energy Conference and Exhibition*, Amsterdam, Netherland, 2014, pp. 1272–1276. doi: 10.4229/EUPVSEC20142014-2CV.4.1.

[52] N. Bay *et al.*, “Adaptation of the industrial PERC solar cell process chain to plated Ni/Cu/Ag front contact metallization,” *AIP Conf. Proc.*, vol. 2147, no. 1, p. 110001, Aug. 2019, doi: 10.1063/1.5123877.

[53] A. Wenham *et al.*, “Copper plated contacts for large-scale manufacturing,” in *IEEE 43rd Photovoltaic Specialists Conference (PVSC)*, Portland, OR, USA, Jun. 2016, pp. 2990–2993. doi: 10.1109/PVSC.2016.7750211.

[54] A. ur Rehman and S. H. Lee, “Review of the Potential of the Ni/Cu Plating Technique for Crystalline Silicon Solar Cells,” *Materials*, vol. 7, no. 2, pp. 1318–1341, Feb. 2014, doi: 10.3390/ma7021318.

[55] H. Jee *et al.*, “Characterization of the Laser Scribing Process of HIT Cells for a Photovoltaic Shingled Module,” *J. Korean Phys. Soc.*, vol. 77, no. 11, pp. 971–974, Dec. 2020, doi: 10.3938/jkps.77.971.

[56] P. Gečys, G. Račiukaitis, E. Miltenis, A. Braun, and S. Ragnow, “Scribing of Thin-film Solar Cells with Picosecond Laser Pulses,” *Phys. Procedia*, vol. 12, pp. 141–148, Jan. 2011, doi: 10.1016/j.phpro.2011.03.116.

[57] P. Baliozian *et al.*, “Thermal Laser Separation of PERC and SHJ Solar Cells,” *IEEE J. Photovolt.*, vol. 11, no. 2, pp. 259–267, Mar. 2021, doi: 10.1109/JPHOTOV.2020.3041251.

[58] S. Eiternick, K. Kaufmann, J. Schneider, and M. Turek, “Loss Analysis for Laser Separated Solar Cells,” *Energy Procedia*, vol. 55, pp. 326–330, Jan. 2014, doi: 10.1016/j.egypro.2014.08.094.

[59] H. Booth, “Laser Processing in Industrial Solar Module Manufacturing,” *J. Laser MicroNanoengineering*, vol. 5, no. 3, pp. 183–191, Dec. 2010, doi: 10.2961/jlmn.2010.03.0001.

[60] M. Kim, D. Kim, D. Kim, and Y. Kang, “Impact of laser pulse width on laser ablation process of high performance PERC cells,” *Sol. Energy*, vol. 110, pp. 208–213, Dec. 2014, doi: 10.1016/j.solener.2014.09.001.

[61] D. K. Kim *et al.*, “Optimization of Laser-opening Pattern for the Efficiency Improvement of Industrial PERC Solar Cell,” in *2018 IEEE 7th World Conference on Photovoltaic Energy Conversion (WCPEC) (A Joint Conference of 45th IEEE PVSC, 28th PVSEC 34th EU PVSEC)*, Jun. 2018, pp. 2142–2144. doi: 10.1109/PVSC.2018.8547984.

[62] M. Kim, D. Kim, D. Kim, and Y. Kang, “Analysis of laser-induced damage during laser ablation process using picosecond pulse width laser to fabricate highly efficient PERC cells,” *Sol. Energy*, vol. 108, pp. 101–106, Oct. 2014, doi: 10.1016/j.solener.2014.06.020.

[63] M. Morales, Y. Chen, D. Munoz-Martin, S. Lauzurica, and C. Molpeceres, “High volume transfer of high viscosity silver pastes using laser direct-write processing for screen printing of c-Si cells,” in *Proc. SPIE 9351, Laser-based Micro- and Nanoprocessing IX*, San Fransisco, California, United States, Mar. 2015, p. 93510B. doi: 10.1117/12.2080092.

[64] M. Colina *et al.*, “Laser Induced Forward Transfer for front contact improvement in silicon heterojunction solar cells,” *Appl. Surf. Sci.*, vol. 336, pp. 89–95, May 2015, doi: 10.1016/j.apsusc.2014.09.172.

[65] D. Munoz-Martin, C. F. Brasz, Y. Chen, M. Morales, C. B. Arnold, and C. Molpeceres, “Laser-induced forward transfer of high-viscosity silver pastes,” *Appl. Surf. Sci.*, vol. 366, pp. 389–396, Mar. 2016, doi: 10.1016/j.apsusc.2016.01.029.

[66] Y. Chen, D. Munoz-Martin, M. Morales, C. Molpeceres, E. Sánchez-Cortezon, and J. Murillo-Gutierrez, “Laser Induced Forward Transfer of High Viscosity Silver Paste for New Metallization Methods in Photovoltaic and Flexible Electronics Industry,” *Phys. Procedia*, vol. 83, pp. 204–210, Jan. 2016, doi: 10.1016/j.phpro.2016.08.010.

[67] F. Kleine-Jäger *et al.*, “BASF´s CypoSol metallization inks for newly developed laser transfer printing (LTP) technology,” presented at the 2nd Workshop on Metallization for Crystalline Silicon Solar Cells, Konstanz, Germany, Apr. 14, 2010.

[68] F. K. Jaeger and J. Kaczun, “Method and Printing Press for Printing a Substrate,” Patent number: WO/2010/069902 A1, Jun. 24, 2010.

[69] F. K. Jaeger, J. Kaczun, and U. Lehmann, “Printing machine and method for printing a substrate,” Patent number: US8840237B2, Sep. 23, 2014

[70] A. Adrian, D. Rudolph, J. Lossen, M. Matusovsky, and V. Chandrasekaran, “Benefits of Pattern Transfer Printing Method for Finger Metallization on Silicon Solar Cells,” in *Proceedings of 35th European Photovoltaic Solar Energy Conference and Exhibition*, Sep. 2018, pp. 434–438. doi: 10.4229/35THEUPVSEC20182018-2CO.12.2.

[71] C. Yüce, K. Okamoto, L. Karpowich, A. Adrian, and N. Willenbacher, “Non-volatile free silver paste formulation for front-side metallization of silicon solar cells,” *Sol. Energy Mater. Sol. Cells*, vol. 200, p. 110040, Sep. 2019, doi: 10.1016/j.solmat.2019.110040.

[72] A. Adrian, D. Rudolph, N. Willenbacher, and J. Lossen, “Finger Metallization Using Pattern Transfer Printing Technology for c-Si Solar Cell,” *IEEE J. Photovolt.*, vol. 10, no. 5, pp. 1290–1298, Sep. 2020, doi: 10.1109/JPHOTOV.2020.3007001.

[73] A. Noy, “Printing high aspect ratio patterns,” International Publication Number: WO 2015/140775 A1, Sep. 24, 2015.

[74] A. Adrian, D. Rudolph, J. Lossen, and N. Willenbacher, “Investigation of Thick-Film-Paste Rheology and Film Material for Pattern Transfer Printing (PTP) Technology,” *Coatings*, vol. 11, no. 1, Art. no. 1, Jan. 2021, doi: 10.3390/coatings11010108.

[75] L. Karpowich, K. Murphy, and W. Zhang, “Advancements in low-silver metallization paste for Si solar cells,” in *38th IEEE Photovoltaic Specialists Conference*, Austin, TX, USA, Jun. 2012, pp. 002171–002174. doi: 10.1109/PVSC.2012.6317975.

[76] Q. Che, H. Yang, L. Lu, and Y. Wang, “A new environmental friendly silver front contact paste for crystalline silicon solar cells,” *J. Alloys Compd.*, vol. 549, pp. 221–225, Feb. 2013, doi: 10.1016/j.jallcom.2012.09.080.

[77] J. Zhou, N. Xu, H. Yang, and Q. Zhang, “Effect of Ag Powder and Glass Frit in Ag Paste on Front Contract of Silicon Solar Cells,” *Procedia Eng.*, vol. 94, pp. 1–5, Jan. 2014, doi: 10.1016/j.proeng.2013.10.007.

[78] J. Qin, S. Bai, W. Zhang, Z. Liu, and H. Wang, “Effects of organic medium on rheological properties of silver pastes for crystalline silicon solar cells,” *Circuit World*, vol. 42, no. 2, pp. 77–83, Jan. 2016, doi: 10.1108/CW-07-2015-0032.

[79] C. Xu, “Screen Printing and Rheology of Pastes,” Ph.D. Dissertation, Karlsruher Instituts für Technologie, Karlsruhe, Germany, 2018.

[80] J. C. Lin and C. Y. Wang, “Effects of surfactant treatment of silver powder on the rheology of its thick-film paste,” *Mater. Chem. Phys.*, vol. 45, no. 2, pp. 136–144, Aug. 1996, doi: 10.1016/0254-0584(96)80091-5.

[81] N. Q. Dzuy and D. V. Boger, “Yield Stress Measurement for Concentrated Suspensions,” *J. Rheol.*, vol. 27, no. 4, pp. 321–349, Aug. 1983, doi: 10.1122/1.549709.

[82] C. Xu and N. Willenbacher, “How rheological properties affect fine-line screen printing of pastes: a combined rheological and high-speed video imaging study,” *J. Coat. Technol. Res.*, vol. 15, no. 6, pp. 1401–1412, Nov. 2018, doi: 10.1007/s11998-018-0091-2.

[83] R. Faddoul, N. Reverdy-Bruas, and J. Bourel, “Silver content effect on rheological and electrical properties of silver pastes,” *J. Mater. Sci. Mater. Electron.*, vol. 23, no. 7, pp. 1415–1426, Jul. 2012, doi: 10.1007/s10854-011-0607-3.

[84] S. Tepner, N. Wengenmeyr, M. Linse, A. Lorenz, M. Pospischil, and F. Clement, “The Link between Ag-Paste Rheology and Screen-Printed Solar Cell Metallization,” *Adv. Mater. Technol.*, vol. 5, no. 10, p. 2000654, 2020, doi: 10.1002/admt.202000654.

[85] C. Yüce, M. König, and N. Willenbacher, “Rheology and Screen-Printing Performance of Model Silver Pastes for Metallization of Si-Solar Cells,” *Coatings*, vol. 8, no. 11, Art. no. 11, Nov. 2018, doi: 10.3390/coatings8110406.

[86] T. G. Mezger, *The Rheology Handbook: for users of rotational and oscillatory rheometers*, 4th. Edition. Hannover: Vincent Network GmbH & Co. KG, 2014.

[87] N. Willenbacher and K. Georgieva, “Rheology of Disperse Systems,” in *Product Design and Engineering*, U. Bröckel, W. Meier, and G. Wagner, Eds. Weinheim, Germany: Wiley-VCH Verlag GmbH & Co. KGaA, 2013, pp. 7–49. doi: 10.1002/9783527654741.ch1.

[88] M. Neidert, W. Zhang, D. Zhang, and A. Kipka, “Screen-printing simulation study on solar cell front side AG paste,” in *IEEE Photovolatic Specialists Conference*, San Diego, CA, USA, May 2008, pp. 1–4. doi: 10.1109/PVSC.2008.4922793.

[89] Y. Zhou *et al.*, “Rheological effect on screen-printed morphology of thick film silver paste metallization,” *J. Mater. Sci. Mater. Electron.*, vol. 28, no. 7, pp. 5548–5553, Apr. 2017, doi: 10.1007/s10854-016-6219-1.

[90] J. Hoornstra, A. W. Weeber, H. de Moor, and S. Wim, “The importance of paste rheology in improving fine line, thick film screen printing of front side metallization,” in *Proceedings of the 14th European Photovoltaic Solar Energy Conference*, Barcelona, Spain, Jul. 1997, pp. 823-826. ISBN: 1-901675-01–09.

[91] K. Abdel Aal and N. Willenbacher, “Front side metallization of silicon solar cells – A high-speed video imaging analysis of the screen printing process,” *Sol. Energy Mater. Sol. Cells*, vol. 217, p. 110721, Nov. 2020, doi: 10.1016/j.solmat.2020.110721.

[92] DIN SPEC 91143-2, “Modern rheological test methods - Part 2: Thixotropy - Determination of the time-dependent structural change - Fundamentals and interlaboratory test.” Sep. 2012.

[93] E. H. Amalu, N. N. Ekere, and S. Mallik, “Evaluation of rheological properties of lead-free solder pastes and their relationship with transfer efficiency during stencil printing process,” *Mater. Des.*, vol. 32, no. 6, pp. 3189–3197, Jun. 2011, doi: 10.1016/j.matdes.2011.02.045.

[94] K.-Y. Law and H. Zhao, *Surface Wetting: Characterization, Contact Angle, and Fundamentals*. Cham: Springer International Publishing, 2016. doi: 10.1007/978-3-319-25214-8.

[95] T.-X. Liang, W. Z. Sun, L.-D. Wang, Y. H. Wang, and H.-D. Li, “Effect of surface energies on screen printing resolution,” *IEEE Trans. Compon. Packag. Manuf. Technol. Part B*, vol. 19, no. 2, pp. 423–426, May 1996, doi: 10.1109/96.496047.

[96] S. Tepner, N. Wengenmeyr, L. Ney, M. Linse, M. Pospischil, and F. Clement, “Improving Wall Slip Behavior of Silver Pastes on Screen Emulsions for Fine Line Screen Printing,” *Sol. Energy Mater. Sol. Cells*, vol. 200, p. 109969, Sep. 2019, doi: 10.1016/j.solmat.2019.109969.

[97] D.-H. Neuhaus and A. Münzer, “Industrial Silicon Wafer Solar Cells,” *Adv. Optoelectron.*, vol. 2007, pp. 1–15, Apr. 2007, doi: 10.1155/2007/24521.

[98] G. Schubert, F. Huster, and P. Fath, “Physical understanding of printed thick-film front contacts of crystalline Si solar cells—Review of existing models and recent developments,” *Sol. Energy Mater. Sol. Cells*, vol. 90, no. 18, pp. 3399–3406, Nov. 2006, doi: 10.1016/j.solmat.2006.03.040.

[99] K.-K. Hong, S.-B. Cho, J.-Y. Huh, H. J. Park, and J.-W. Jeong, “Role of PbO-based glass frit in Ag thick-film contact formation for crystalline Si solar cells,” *Met. Mater. Int.*, vol. 15, no. 2, pp. 307–312, Apr. 2009, doi: 10.1007/s12540-009-0307-1.

[100] S. W. Paddock, “Confocal Laser Scanning Microscopy,” *BioTechniques*, vol. 27, no. 5, pp. 992–1004, Nov. 1999, doi: 10.2144/99275ov01.

[101] N. S. Claxton, T. J. Fellers, and M. W. Davidson, “Microscopy, Confocal,” in *Encyclopedia of Medical Devices and Instrumentation*, American Cancer Society, 2006. doi: 10.1002/0471732877.emd291.

[102] Digital Surf, *Mountains Technology Surface Texture Analysis Premium v. 5.1.0.5338*. Besançon, France, 2009.

[103] L. Reimer, *Scanning Electron Microscopy: Physics of Image Formation and Microanalysis*, 2th Edition. Berlin Heidelberg: Springer-Verlag, 1998. doi: 10.1007/978-3-540-38967-5.

[104] B. Fischer, M. Keil, P. Fath, and E. Bucher, “Scanning IQE-measurement for accurate current determination on very large area solar cells,” in *Conference Record of the Twenty-Ninth IEEE Photovoltaic Specialists Conference*, New Orleans, LA, USA, May 2002, pp. 454–457. doi: 10.1109/PVSC.2002.1190557.

[105] K. Mertens, *Photovoltaics: fundamentals, technology and practice*, First Edition. Chichester: Wiley, 2014.

[106] D. K. Schroder, *Semiconductor material and device characterization*, 3rd ed. Hoboken, New Jersey, USA: John Wiley & Sons, Inc., 2006.

[107] D. L. Meier and D. K. Schroder, “Contact resistance: Its measurement and relative importance to power loss in a solar cell,” *IEEE Trans. Electron Devices*, vol. 31, no. 5, pp. 647–653, May 1984, doi: 10.1109/T-ED.1984.21584.

[108] S. Guo, G. Gregory, A. M. Gabor, W. V. Schoenfeld, and K. O. Davis, “Detailed investigation of TLM contact resistance measurements on crystalline silicon solar cells,” *Sol. Energy*, vol. 151, pp. 163–172, Jul. 2017, doi: 10.1016/j.solener.2017.05.015.

[109] D. L. Meier *et al.*, “Determining Components of Series Resistance from Measurements on a Finished Cell,” in *IEEE 4th World Conference on Photovoltaic Energy Conference*, Waikoloa, HI, USA, May 2006, vol. 2, pp. 1315–1318. doi: 10.1109/WCPEC.2006.279656.

[110] M. Dhimish and V. Holmes, “Solar cells micro crack detection technique using state-of-the-art electroluminescence imaging,” *J. Sci. Adv. Mater. Devices*, vol. 4, no. 4, pp. 499–508, Dec. 2019, doi: 10.1016/j.jsamd.2019.10.004.

[111] T. Trupke, R. A. Bardos, M. C. Schubert, and W. Warta, “Photoluminescence imaging of silicon wafers,” *Appl. Phys. Lett.*, vol. 89, no. 4, p. 044107, Jul. 2006, doi: 10.1063/1.2234747.

[112] T. Trupke, B. Mitchell, J. W. Weber, W. McMillan, R. A. Bardos, and R. Kroeze, “Photoluminescence Imaging for Photovoltaic Applications,” *Energy Procedia*, vol. 15, pp. 135–146, Jan. 2012, doi: 10.1016/j.egypro.2012.02.016.

[113] K. Bothe *et al.*, “Electroluminescence as an in-line characterisation tool for solar cell production,” in *21st European Photovoltaic Solar Energy Conference*, Dresden, Germany, Sep. 2006, pp. 597–600.

[114] R. Bock, P. P. Altermatt, and J. Schmidt, “Accurate extraction of doping profiles from electrochemical capacitance voltage measurements,” in *23rd European Photovoltaic Solar Energy Conference*, Valencia, Spain, 2008, pp. 1510–1513.

[115] P. Blood, “Capacitance-voltage profiling and the characterisation of III-V semiconductors using electrolyte barriers,” *Semicond. Sci. Technol.*, vol. 1, no. 1, pp. 7–27, Jul. 1986, doi: 10.1088/0268-1242/1/1/002.

[116] E. Peiner, A. Schlachetzki, and D. Krüger, “Doping Profile Analysis in Si by Electrochemical Capacitance-Voltage Measurements,” *J. Electrochem. Soc.*, vol. 142, no. 2, p. 576, Feb. 1995, doi: 10.1149/1.2044101.

[117] C. Yüce and N. Willenbacher, “Challenges in Rheological Characterization of Highly Concentrated Suspensions — A Case Study for Screen-printing Silver Pastes,” *JoVE J. Vis. Exp.*, no. 122, p. e55377, Apr. 2017, doi: 10.3791/55377.

[118] C. W. Macosko, *Rheology: Principles, Measurements, and Applications*. New York Weinheim: Wiley-VCH, Inc., 1994.

[119] A. I. Rusanov and V. A. Prokhorov, *Interfacial Tensiometry*, 1st edition., vol. Volume 3. Amsterdam, Netherland: Elsevier Science B.V., 1996. Accessed: Jul. 04, 2021. [Online]. Available: http://www.123library.org/book_details/?id=39042

[120] C. A. Schneider, W. S. Rasband, and K. W. Eliceiri, “NIH Image to ImageJ: 25 years of image analysis,” *Nat. Methods*, vol. 9, no. 7, Art. no. 7, Jul. 2012, doi: 10.1038/nmeth.2089.

[121] P. Gabbott, “A Practical Introduction to Differential Scanning Calorimetry,” in *Principles and applications of thermal analysis*, Oxford, UK: Blackwell Publishing Ltd, 2008.

[122] G. Höhne, W. F. Hemminger, and H.-J. Flammersheim, *Differential Scanning Calorimetry*, 2nd revised and Enlarged edition. Berlin-Heidelberg: Springer-Verlag, 2003.

[123] R. De Rose *et al.*, “A methodology to account for the finger interruptions in solar cell performance,” *Microelectron. Reliab.*, vol. 52, no. 9, pp. 2500–2503, Sep. 2012, doi: 10.1016/j.microrel.2012.07.014.

[124] J. Lossen, D. Rudolph, A. Adrian, and L. J. Koduvelikulathu, “How many finger-interruptions should we tolerate?,” presented at the 8th Workshop on Metallization & Interconnection for Crystalline Silicon Solar Cells, Konstanz, Germany, May 13, 2019.

[125] D. A. Willis, “Laser-Induced Forward Transfer of Metals,” in *Laser Printing of Functional Materials*, John Wiley & Sons, Ltd, 2018, pp. 149–174. doi: 10.1002/9783527805105.ch7.

[126] M. Galiazzo *et al.*, “Fine Line Double Printing and Advanced Process Control for Cell Manufacturing,” *Energy Procedia*, vol. 67, pp. 116–125, Apr. 2015, doi: 10.1016/j.egypro.2015.03.295.

[127] C. P. Hsu, R. H. Guo, C. C. Hua, C.-L. Shih, W.-T. Chen, and T.-I. Chang, “Effect of polymer binders in screen printing technique of silver pastes,” *J. Polym. Res.*, vol. 20, no. 10, p. 277, Oct. 2013, doi: 10.1007/s10965-013-0277-3.

[128] K. Patel, Y. Yoshioka, R. D. Baldyga, and W. Zhang, “Front side photovoltaics metallization pastes for high aspect ratio grid lines,” in *37th IEEE Photovoltaic Specialists Conference*, Seattle, WA, USA, Jun. 2011, pp. 001154–001156. doi: 10.1109/PVSC.2011.6186157.

[129] J. Wong, “Griddler: Intelligent computer aided design of complex solar cell metallization patterns,” in *IEEE 39th Photovoltaic Specialists Conference (PVSC)*, Jun. 2013, pp. 0933–0938. doi: 10.1109/PVSC.2013.6744296.

[130] A. Mette, “New concepts for front side metallization of industrial silicon solar cells,” Ph.D. Dissertation, Albert-Ludwigs-Universität Freiburg, Freiburg im Breisgau, Germany, 2007. [Online]. Available: https://freidok.uni-freiburg.de/data/3782

[131] S. Wiese, F. Kraemer, N. Betzl, and D. Wald, “Interconnection technologies for photovoltaic modules - analysis of technological and mechanical problems,” in *11th International Thermal, Mechanical Multi-Physics Simulation, and Experiments in Microelectronics and Microsystems (EuroSimE)*, Bordeaux, France, Apr. 2010, pp. 1–6. doi: 10.1109/ESIME.2010.5464518.

[132] J. Walter, L. C. Rendler, A. Halm, V. Mihailetchi, A. Kraft, and U. Eitner, “Ribbon interconnection of 6” BC-BJ solar cells,” *Energy Procedia*, vol. 124, pp. 504–514, Sep. 2017, doi: 10.1016/j.egypro.2017.09.287.

[133] J. Walter, M. Tranitz, M. Volk, C. Ebert, and U. Eitner, “Multi-wire Interconnection of Busbar-free Solar Cells,” *Energy Procedia*, vol. 55, pp. 380–388, Jan. 2014, doi: 10.1016/j.egypro.2014.08.109.

[134] S. Schindler, J. Schneider, C. Pönisch, R. Nissler, and D. Habermann, “Soldering Process and Material Characterization of Miniaturized Contact Structures of a Newly Developed Multi Busbar Cell Metallization Concept,” in *Proceedings of 28th European Photovoltaic Solar Energy Conference and Exhibition*, Paris, France, Oct. 2013, pp. 480–483. doi: 10.4229/28THEUPVSEC2013-1CV.2.13.

[135] T. Söderström, P. Papet, and J. Ufheil, “Smart Wire Connection Technology,” in *Proceedings of 28th European Photovoltaic Solar Energy Conference and Exhibition*, Paris, France, Oct. 2013, pp. 495–499. doi: 10.4229/28THEUPVSEC2013-1CV.2.17.

[136] P. Papet *et al.*, “New Cell Metallization Patterns for Heterojunction Solar Cells Interconnected by the Smart Wire Connection Technology,” *Energy Procedia*, vol. 67, pp. 203–209, Apr. 2015, doi: 10.1016/j.egypro.2015.03.039.

[137] T. Fellmeth, F. Clement, and D. Biro, “Analytical Modeling of Industrial-Related Silicon Solar Cells,” *IEEE J. Photovolt.*, vol. 4, no. 1, pp. 504–513, Jan. 2014, doi: 10.1109/JPHOTOV.2013.2281105.

[138] Y. Zhang *et al.*, “Knotless Screen Printing for Crystalline Silicon Solar Cells,” presented at the 7th Workshop ion Metallization and Interconnection for Crystalline Silicon Solar Cells, Konstanz, Germany, Oct. 23, 2017. Accessed: Apr. 25, 2021. [Online]. Available: https://www.researchgate.net/publication/324543932_Knotless_Screen_Printing_for_Crystalline_Silicon_Solar_Cells/link/5ad4c1600f7e9b285936a066/download

[139] L. Ney *et al.*, “Optimization of fine line screen printing using in-depth screen mesh analysis,” in *Proceedings of the 8th Workshop on Metallization and Interconnection for Crystalline Silicon Solar Cells*, Perak, Malaysia, Sep. 2019, p. 020006. doi: 10.1063/1.5125871.

[140] H. Hannebauer, T. Dullweber, T. Falcon, and R. Brendel, “Fineline Printing Options for High Efficiencies and Low Ag Paste Consumption,” *Energy Procedia*, vol. 38, pp. 725–731, Jan. 2013, doi: 10.1016/j.egypro.2013.07.339.

[141] H. Hannebauer, T. Dullweber, T. Falcon, X. Chen, and R. Brendel, “Record Low Ag Paste Consumption of 67.7 mg with Dual Print,” *Energy Procedia*, vol. 43, pp. 66–71, Jan. 2013, doi: 10.1016/j.egypro.2013.11.089.

[142] M. Galiazzo, O. Borsato, and E. Bortoletto, “Fine Line Double Printing + for Today and Tomorrow Cell Metallization and Interconnection,” in *Proceedigs of 32nd European Photovoltaic Solar Energy Conference and Exhibition*, Jun. 2016, pp. 958–960. doi: 10.4229/EUPVSEC20162016-2BV.7.46.

[143] T. Falcon, “High Accuracy, High Aspect Ratio Metallization on Silicon Solar Cells Using a Print on Print Process,” in *Proceedings of the 25th European Photovoltaic Solar Energy Conference and Exhibition*, Sep. 2010, pp. 1651–1655. doi: 10.4229/25THEUPVSEC2010-2CV.1.66.

[144] Y.-H. Chang, W.-M. Su, P.-S. Huang, and L.-W. Cheng, “Improvement of the solar cell efficiency by fine line print on print technology,” in *39th Photovoltaic Specialists Conference (PVSC)*, Tampa, FL, USA, Jun. 2013, pp. 2176–2178. doi: 10.1109/PVSC.2013.6744906.

[145] C. Bottosso, W. Tao, X. Wang, L. Ma, and M. Galiazzo, “Reliable Metallization Process for Ultra Fine Line Printing,” *Energy Procedia*, vol. 43, pp. 80–85, Jan. 2013, doi: 10.1016/j.egypro.2013.11.091.

[146] A. Voltan, E. Bortoletto, O. Borsato, and M. Galiazzo, “Toward 30µm Printed Ag Finger Width by Ultra Fine Line Double Printing,” in *Proceedings of 31st European Photovoltaic Solar Energy Conference and Exhibition*, Hamburg, Germany, Sep. 2015, pp. 704–708. doi: 10.4229/EUPVSEC20152015-2AV.2.33.

[147] Applied Materials, Inc., “Applied Tempo™ Metallization System | Applied Materials.” https://www.appliedmaterials.com/products/tempo (accessed Apr. 23, 2021).

[148] ASYS Automatisierung GmbH, “AIRON: The fastest way to print,” Aug. 06, 2020. https://www.asys-group.com/en/products/energy/solar/ (accessed Apr. 23, 2021).

[149] F. Clement *et al.*, “‘Project FINALE’ - Screen and Screen Printing Process Development for Ultra-Fine-Line Contacts below 20µm Finger Width,” in *Proceedings of 36th European Photovoltaic Solar Energy Conference and Exhibition*, Marseille, France, Sep. 2019, pp. 255–258. doi: 10.4229/EUPVSEC20192019-2DO.5.1.

[150] A. Lorenz *et al.*, “Screen Printed Thick Film Metallization of Silicon Solar Cells - Recent Developments and Future Perspectives,” in *Proceedings of 35th European Photovoltaic Solar Energy Conference and Exhibition*, Brussels, Belgium, Sep. 2018, pp. 819–824. doi: 10.4229/35THEUPVSEC20182018-2DV.3.65.

[151] K. A. Münzer *et al.*, “Development and Implementation of 19 % Rear Passivation and Local Contact Centaurus Technology,” in *26th European Photovoltaic Solar Energy Conference and Exhibition*, Hamburg, Germany, 2011, pp. 2292–2297. doi: 10.4229/26THEUPVSEC2011-2CV.4.53.

[152] A. Blakers, “Development of the PERC Solar Cell,” *IEEE J. Photovolt.*, vol. 9, no. 3, pp. 629–635, May 2019, doi: 10.1109/JPHOTOV.2019.2899460.

[153] M. S. Jeong *et al.*, “Dependence of the Optimization of the Front Grid Design in Passivated Emitter and Rear Contact c-Si Solar Cells on the Finger Width and the Aspect Ratio,” *J. Korean Phys. Soc.*, vol. 76, no. 8, pp. 774–780, Apr. 2020, doi: 10.3938/jkps.76.774.

[154] M. M. Hilali, S. Sridharan, C. Khadilkar, A. Shaikh, A. Rohatgi, and S. Kim, “Effect of glass frit chemistry on the physical and electrical properties of thick-film Ag contacts for silicon solar cells,” *J. Electron. Mater.*, vol. 35, no. 11, pp. 2041–2047, Nov. 2006, doi: 10.1007/s11664-006-0311-x.

[155] B. Hallam *et al.*, “Efficiency enhancement of i-PERC solar cells by implementation of a laser doped selective emitter,” *Sol. Energy Mater. Sol. Cells*, vol. 134, pp. 89–98, Mar. 2015, doi: 10.1016/j.solmat.2014.11.028.

[156] W. Wu, Z. Zhang, F. Zheng, W. Lin, Z. Liang, and H. Shen, “Efficiency enhancement of bifacial PERC solar cells with laser-doped selective emitter and double-screen-printed Al grid,” *Prog. Photovolt. Res. Appl.*, vol. 26, no. 9, pp. 752–760, 2018, doi: https://doi.org/10.1002/pip.3013.

[157] C. Zhang, H. Shen, L. Sun, J. Yang, S. Wu, and Z. Lu, “Bifacial p-Type PERC Solar Cell with Efficiency over 22% Using Laser Doped Selective Emitter,” *Energies*, vol. 13, no. 6, Art. no. 6, Jan. 2020, doi: 10.3390/en13061388.

[158] A. Wolf *et al.*, “Status and Perspective of Emitter Formation by POCl3-Diffusion,” in *31st European Photovoltaic Solar Energy Conference and Exhibition*, Hamburg, Germany, Sep. 2015, pp. 414–419. doi: 10.4229/EUPVSEC20152015-2CO.4.1.

[159] W. Deng *et al.*, “Development of High-efficiency Industrial p-type Multi-crystalline PERC Solar Cells with Efficiency Greater Than 21%,” *Energy Procedia*, vol. 92, pp. 721–729, Aug. 2016, doi: 10.1016/j.egypro.2016.07.050.

[160] D. Rudolph *et al.*, “Influence of the paste volume on the contact formation in fine line metallization,” in *IEEE 7th World Conference on Photovoltaic Energy Conversion (WCPEC) (A Joint Conference of 45th IEEE PVSC, 28th PVSEC & 34th EU PVSEC)*, Waikoloa, HI, USA, Jun. 2018, pp. 2678–2682. doi: 10.1109/PVSC.2018.8547938.

[161] S. Yuan *et al.*, “Novel Ag-doped glass frits for high-efficiency crystalline silicon solar cells,” *Chem. Commun.*, vol. 53, no. 46, pp. 6239–6242, Jun. 2017, doi: 10.1039/C7CC02838E.

[162] H.-S. Kim *et al.*, “Electrochemical nature of contact firing reactions for screen-printed silicon solar cells: origin of ‘gray finger’ phenomenon,” *Prog. Photovolt. Res. Appl.*, vol. 24, no. 9, pp. 1237–1250, 2016, doi: https://doi.org/10.1002/pip.2783.

[163] H. Chu *et al.*, “Impact of the Presence of Busbars During the Fast Firing Process on Contact Resistances,” *IEEE J. Photovolt.*, vol. 8, no. 4, pp. 923–929, Jul. 2018, doi: 10.1109/JPHOTOV.2018.2828824.

[164] R. Mayberry and V. Chandrasekaran, “Metallization contributions, requirements, and effects related to pattern transfer printing (PTP^{TM}) on crystalline silicon solar cells,” Perak, Malaysia, 2019, p. 020008. doi: 10.1063/1.5125873.

[165] J. Schmidt, A. G. Aberle, and R. Hezel, “Investigation of carrier lifetime instabilities in Cz-grown silicon,” in *Conference Record of the Twenty Sixth IEEE Photovoltaic Specialists Conference*, Sep. 1997, pp. 13–18. doi: 10.1109/PVSC.1997.653914.

[166] T. Niewelt, J. Schön, W. Warta, S. W. Glunz, and M. C. Schubert, “Degradation of Crystalline Silicon Due to Boron–Oxygen Defects,” *IEEE J. Photovolt.*, vol. 7, no. 1, pp. 383–398, Jan. 2017, doi: 10.1109/JPHOTOV.2016.2614119.

[167] P. Hamer, B. Hallam, M. Abbott, C. Chan, N. Nampalli, and S. Wenham, “Investigations on accelerated processes for the boron–oxygen defect in p-type Czochralski silicon,” *Sol. Energy Mater. Sol. Cells*, vol. 145, pp. 440–446, Feb. 2016, doi: 10.1016/j.solmat.2015.11.013.

[168] A. Herguth, “How to Properly Assess Boron-Oxygen Related Degradation in Crystalline Silicon,” in *33rd European Photovoltaic Solar Energy Conference and Exhibition*, Amsterdam, Netherland, Sep. 2017, pp. 576–579. doi: 10.4229/EUPVSEC20172017-2AV.1.43.

[169] M. Padmanabhan *et al.*, “Light-induced degradation and regeneration of multicrystalline silicon Al-BSF and PERC solar cells,” *Phys. Status Solidi RRL – Rapid Res. Lett.*, vol. 10, no. 12, pp. 874–881, 2016, doi: https://doi.org/10.1002/pssr.201600173.

[170] A. A. Brand *et al.*, “Ultrafast In-Line Capable Regeneration Process for Preventing Light Induced Degradation of Boron-Doped p-Type Cz-Silicon Perc Solar Cells,” in *33rd European Photovoltaic Solar Energy Conference and Exhibition*, Amsterdam, Netherland, Sep. 2017, pp. 382–387. doi: 10.4229/EUPVSEC20172017-2CO.9.5.

[171] pv-tools GmbH, “IQE-SCAN: Spectral quantum efficiency & reflectance.” http://www.pv-tools.de/products/iqe-scan.html (accessed May 27, 2021).

[172] greateyes GmbH, “LumiSolarCell System - Photoluminescence (PL), Electroluminescence (EL), and Thermogrpahy (IR) Inspection of Photovoltaic Cells and Wafers.” Accessed: Jun. 27, 2021. [Online]. Available: https://www.greateyes.de/projects/greateyes/static/custom/file/LumiSolarCell_Brochure.pdf

[173] Netzsch-Gerätebau GmbH, “DSC 214 Polyma - Die Systemlösung zur effizienten Charakterisierung polymerer Werkstoffe.” Accessed: Apr. 07, 2021. [Online]. Available: https://www.netzsch-thermal-analysis.com/de/produkte-loesungen/dynamische-differenzkalorimetrie-differenz-thermoanalyse/dsc-214-polyma/

Appendix

Specifications of measurement devices

Table A1: Specifications of cetisPV sun simulator from h.a.l.m electronik GmbH.

Parameter	Value
Spectral mismatch	Class A according IEC 60904-9
Spatial non-uniformity	Class A according IEC 60904-9
Temporal stability	Class A according IEC 60904-9
Flash duration	up to 60 ms
Irradiance	200 to 1000 $W \cdot m^{-2}$

Table A2: Specifications of IQE-Scan from pv-tools GmbH [171].

Parameter	Value
Monochromatic light	280 – 1600 nm
Full width Half Maximum (FWHM) bandwidth	8 nm
Wavelength accuracy	1 nm
White bias light	up to 1.2 suns
Trans impedance amplifier	max 200 mA

Table A3: Specifications of LumiSolarCell from greateyes GmbH [172].

Parameter	Value
Programmable power supply	0 – 100 V and 0 – 7.5 A
Substrate size	max. 200 mm × 200 mm
Image size	1024 ×1024 pixel, 16 bit
Image resolution	150 µm per pixel
Typical exposure times	0.1 – 10 s

Table A4: Specifications of DSC 214 Polyma from Netzsch-Gerätebau GmbH [173].

Parameter	Value
Temperature range	–170 °C to 600 °C
Heating or cooling rate	0.001 $K \cdot min^{-1}$ to 500 $K \cdot min^{-1}$
Technical resolution	0.1 µW
Enthalpy precision	±0.5% to ±2%
Sample mass	minimum 10 mg

List of publications

Peer-Reviewed Journal contributions

First author

1. A. Adrian, D. Rudolph, J. Lossen, and N. Willenbacher, “Investigation of Thick-Film-Paste Rheology and Film Material for Pattern Transfer Printing (PTP) Technology,” *Coatings*, vol. 11, no. 1, p. 108, 2021. DOI: 10.3390/coatings11010108.
2. A. Adrian, D. Rudolph, N. Willenbacher and J. Lossen, "Finger Metallization Using Pattern Transfer Printing Technology for c-Si Solar Cell," *IEEE Journal of Photovoltaics*, vol. 10, no. 5, pp. 1290-1298, 2020. DOI: 10.1109/JPHOTOV.2020.3007001.

Co-authors

1. K. Tsuji, S. Suzuki, N. Morishita, T. Kuroki, M. Nakahara, M. Dhamrin, A. Adrian, Z. W. Peng, T. Buck, and N. Usami, “Contact control of Al/Si interface of Si solar cells by local contact opening method,” *Materials Chemistry and Physics*, 2021. DOI: 10.1016/j.matchemphys.2021.124833.
2. P. Ferrada, D. Rudolph, C. Portillo, A. Adrian, J. Correa-Puerta, R. Sierpe, V. Campo, M. Flores, T. P. Corrales, R. Henríquez, M. J. Kogan, and J. Lossen., “Interface analysis of Ag/n-type Si contacts in n-type PERT solar cells,” *Progress in Photovoltaics: Research and Applications*, 28: 358-371, 2020. DOI: 10.1002/pip.3242.
3. C. Yüce, K. Okamoto, L. Karpowich, A. Adrian, and N. Willenbacher, “Non-volatile free silver paste formulation for front-side metallization of silicon solar cells,” *Solar Energy Materials and Solar Cells*, 2019. DOI: 10.1016/j.solmat.2019.110040.

Conference contributions

Oral presentations

1. A. Adrian, D. Rudolph, and J. Lossen, “Ultra-fine contact fingers achieved by laser printing,” in SiliconFOREST, Falkau, Germany, 2019.
2. A. Adrian, D. Rudolph, J. Lossen, M. Matusovsky, and V. Chandrasekaran, “Benefits of Pattern Transfer Printing Method for Finger Metallization on Silicon Solar Cells,” in *35th European Photovoltaic Solar Energy Conference and Exhibition*, Brussels, Belgium, 2018. DOI: 10.4229/35THEUPVSEC20182018-2CO.12.2.

Visuals

1. A. Adrian, D. Rudolph, J. Lossen, M. Matusovsky, and A. Noy, “Ultra-Fine Contact Finger Achieved by Pattern Transfer Printing (PTP) Technology for Silicon Solar Cells – Recent Development,” in *36th European Photovoltaic Solar Energy Conference and Exhibition*, Marseille, France, 2019.

Co-Authors

1. Z. W. Peng, T. Buck, A. Adrian, S. Suzuki, V. D. Mihailetchi, A. Mazurov, S. Seren, C. Buchner, M. Darmin, and R. Kopecek, “Performance Upgrade Solutions for Low Cost n-PERT-RJ Solar Cells by Adopting APCVD System,” in *30th International Photovoltaic Science and Engineering Conference (PVSEC-30) & Global Photovoltaic Conference 2020 (GPVC 2020)*, Jeju, Republic of Korea, 2020.
2. J. Correa-Puerta, P. Ferrada, C. Portillo, D. Rudolph, A. Adrian, J. Lossen, M. Flores, R. Henríquez, T. P. Corrales, R. Sierpe, M. J. Kogan, and V. Campo, “Electrical conduction in the Ag/Si interface of silicon solar cells,“ in *9th International Conference on Low Dimensional Structures and Devices*, Puerto Varas, Chile, 2019.
3. J. Lossen, D. Rudolph, A. Adrian, and L. J. Koduvelikulathu, “How many finger-interruptions should we tolerate?” in *8th Workshop on Metallization & Interconnection for Crystalline Silicon Solar Cells*, Konstanz, Germany, 2019.
4. C. Camus, A. Adrian, J. Bogenrieder, J. Hauch, and C. J. Brabec, “Assessment of Technology- and Weather-Specific Temperature Losses of Various Photovoltaic Technologies, ” in *35th European Photovoltaic Solar Energy Conference and Exhibition*, Brussels, Belgium, 2018, pp. 1177-1181. DOI: 10.4229/35thEUPVSEC20182018-5CV.1.13.
5. C. Camus, A. Adrian, J. Bogenrieder, J. Hauch, and C. J. Brabec, “Assessment of Technology- and Site-Specific Weak Light Losses of Various Photovoltaic Technologies,” in *Integrated Photovoltaic Technical Conference*, Cassis, France, 2018. DOI: 10.13140/RG.2.2.24789.88802.
6. D. Rudolph, A. Adrian, J. Lossen, P. Ferrada, C. Portillo, V. Del Campo, J. Correa, R. Sierpe, and M. J. Kogan, “Influence of the paste volume on the contact formation in fine line metallization,” in *IEEE 7th World Conference on Photovoltaic Energy Conversion*, Waikoloa, USA, 2018. DOI: 10.1109/PVSC.2018.8547938.

Chapter in an edited book contributions

1. M. Pospischil, A. Lorenz S. Kühnhold-Pospischil, A. Adrian, “Alternative printing technologies,” in Silicon Solar Cell Metallization and Module Technology. T. Dullweber and L. Tous, Eds. IET Energy Engineering Series 174, London: The Institution of Engineering and Technology, 2021, ch. 7, pp. 255-307. DOI: 10.1049/PBPO174E_ch7.